creative commons
COMMONS DEED

저작자표시-비영리-변경금지 2.0 대한민국

이용자는 아래의 조건을 따르는 경우에 한하여 자유롭게

- 이 저작물을 복제, 배포, 전송, 전시, 공연 및 방송할 수 있습니다.

다음과 같은 조건을 따라야 합니다:

저작자표시. 귀하는 원저작자를 표시하여야 합니다.

비영리. 귀하는 이 저작물을 영리 목적으로 이용할 수 없습니다.

변경금지. 귀하는 이 저작물을 개작, 변형 또는 가공할 수 없습니다.

- 귀하는, 이 저작물의 재이용이나 배포의 경우, 이 저작물에 적용된 이용허락조건을 명확하게 나타내어야 합니다.
- 저작권자로부터 별도의 허가를 받으면 이러한 조건들은 적용되지 않습니다.

저작권법에 따른 이용자의 권리는 위의 내용에 의하여 영향을 받지 않습니다.

이것은 이용허락규약(Legal Code)을 이해하기 쉽게 요약한 것입니다.

Disclaimer

dCollection

공학박사학위논문

α-Synuclein-Mediated Two-Dimensional Assembly of Gold Nanoparticles and Its Applications

알파-시뉴클레인을 활용한 금나노입자의 2차원 조립 및 그 응용

2017년 2월

서울대학교 대학원

화학생물공학부

이 정 희

Abstract

α-Synuclein-Mediated Two-Dimensional Assembly of Gold Nanoparticles and Its Applications

Junghee Lee

School of Chemical and Biological Engineering

The Graduate School

Seoul National University

Nanoparticles exhibit exceptional chemical, optical, and electrical properties. To maximize those advantages in realistic devices, hierarchical assembly of nanoparticles into supra-structures is essential. Among various supra-structures, two-dimensional organization of nanoparticles is of great interest to utilize nanoparticles in diverse electrical and optoelectrical devices. To organize nanoparticles into two-dimensional structures, diverse macromolecules such as DNA or polymers have been employed.

α-Synuclein (αS) is an amyloidogenic protein which produces amyloid fibrils via self-assembly and constitutes a major component of

Lewy bodies observed in Parkinson's disease patients. The protein is a member of intrinsically disordered proteins (IDPs) characterized by multiple partner molecules due to their structural plasticity. Interestingly, we have found out that αS encapsulates gold nanoparticles (AuNPs). αS consists of 140 amino acids and can be fdivided as three regions of the basic N-terimus, the hydrophobic middle segement of non-amyloid-β component (NAC), and the acidic C-terminus. Due to the positive charge of N-termial region, the region was demonstrated to be main part of the interaction between αS and negatively charged citrate-capped AuNPs. Therefore, the hydrophobic NAC and the negatively charged C-terminal region of αS would be exposed.

In this study, the adhesive property of αS-AuNP has been investigated in acidic solution. αS-AuNP showed omni-adhesive property at pH 4.5. Impressively, the αS-AuNP complex adsorbed onto all the surfaces that we have tested, including oxides, amorphous ceramic material, semiconductors, metal, polymers, polymeric organosilicon, carbon materials, and natural minerals. The most intriguing part was that αS-AuNP adsorbed as tightly packed single layer regardless of chemical and physical nature of the substrate. The adsorption was explained by two different interactions: (i) interactions between αS and substrate and (ii) repulsive interaction between C-terminus of αS molecules. Interaction between αS and diverse substrates was enabled by structural plasticity of αS and induced adsorption of αS-AuNP. Repulsive interaction between the C-terminus of αS molecules precluded additional adsorption.

The omni-adhesive property of αS-AuNPs was found to have great feasibility in various systems. E-beam lithography enabled the patterning of αS-AuNP in 100-nm-resolution. The solution-based adsorption strategy also allowed conformal organization of AuNPs onto diverse 3-D objects from macro-glass crystals to nano-materials. We applied the αS-AuNP adsorption to memory development, fuel-cell, solar-cell, cell-culture platform, and photothermal cancer therapy. The outlying αS played versatile roles such as dielectric layer for charge retention, sacrificial layer to expose AuNPs for chemical catalysis, reaction center for silicification, and bio-interface for cell attachment, respectively. Here, we also introduce free-standing αS-AuNP film. There were a lot of struggles in making ultrathin films with high nanoparticle density over micro scale. We have employed omni-adhesive property of αS-AuNP film in the fabrication of free-standing film. First, we have made αS-AuNP complex and adsorbed αS-AuNP single layer onto polycarbonate (PC) substrate. After the adsorption, PC substrate was dissolved using chloroform. The organic solvent treatment induced direct self-assembly of αS which led to β-sheet bridges between nanoparticles.

Keywords

α-Synuclein; Gold nanoparticle; Nano devices; Omni-adhesive property; Single layer

Student number: 2012-20967

Contents

Abstract·····i

Contents·····iv

List of Tables·····viii

List of Figures····· ix

Part I. Omni-adhesive property of α-synculein-gold nanoparticle complex

I-1.

Introduction····· 1

(1) Two-dimensional organization of nanoparticles ····· 1

(2) Generalizable surface functionalization ····· 1

(3) α-synculein, an intrinsically disordered protein ····· 2

(4) Interaction between αS and gold nanoparticle ····· 3

I-2. Experimental Section····· 5

(1) Purification of αS ····· 5

(2) Substrate preparation ····· 5

(3) X-ray photoelectron spectroscopy (XPS) characterization ····· 6

(4) Atomic force microscope (AFM) analysis ····· 6

(5) Contact angle measurements ····· 7

(6) Large-area monolayer formation of αS-AuNP adsorbed on SiO_2

wafer ····· 7
(7) Field-emission scanning electron microscope (FE-SEM) analysis ····· 8
(8) Transmission electron microscope (TEM) analysis ····· 8
(9) Computational calculation for isoelectric point (pI) of αS ····· 8
(10) High-density single-layer coating of αS-AuNPs onto various materials ····· 9
(11) Electron-beam (e-beam) lithography for 2-Dimensional patterning of αS-AuNPs in single-layer ····· 10
(12) Fabrication of micro-fluidic device and 3-D microwell array ····· 11
I-3. Results and Discussion····· 12
(1) Single-layer Adsorption of αS-AuNPs ····· 12
(2) pH-dependence of Single-layer Adsorption of αS-AuNPs ····· 16
(3) Omni-adhesiveness of αS-AuNPs Producing the Close-packed Single-layer AuNP Coat over Multiple Substrates ····· 24
(4) High-density Single-layer Coating of AuNPs over Multiple Geometric Shapes in 2-D and 3-D ····· 34
I-4. Conclusions····· 39
Part II. Multiple Uses of Hybrid Gold Nanoparticles with α-Synuclein Protein
II-1. Introduction····· 40

(1) Applications of NP-based high-performance devices ……40
(2) Role of the αS layer ……40
(3) Nanoparticle based organic field-effect transistors ……41
(4) Nanoparticle based fuel-cell performance enhancement ……42
(5) Particle-on-a-particle system and dye-sensitized solar cell ……43
(6) Cell attachment and photothermal cancer therapy ……45
II-2. Experimental Section……46
(1) Fabrication and characterization of memory devices …… 46
(2) Oxygen reduction reaction (ORR) performance test …… 48
(3) Plasmon-enhanced dye-sensitized solar cell …… 49
(4) Cell culture …… 51
(5) Immunostaining and confocal laser scanning microscope (CLSM) examination …… 51
(6) HeLa cell detachment by the photodynamic effect of αS-AuNP single-layer coat …… 52
(7) Synthesis of AuNPs and GO …… 53
(8) Preparation and Characterization of AuNP/GO hybrid sheets …… 54
II-3. Results and Discussion…… 55
(1) Efficient Charge Trapping of the αS-AuNP Single-Layer in Memory Transistors …… 55
(1)-1. Non-flexible substrate based memory development …… 55
(1)-2. Flexible substrate based memory development …… 69

(2) Single-layered High Density Coating of αS-AuNPs on CNT for the Oxygen Reduction Reaction in Fuel Cells ····· 74
(3) Facile Fabrication of αS-AuNP Satellites on TiO_2 Microsphere and Their Use in the Dye-sensitized Solar Cells ····· 79
(4) Cell Immobilization on the Diverse Surfaces of 2-D and 3-D Objects Pre-coated with the Biocompatible αS-AuNPs ····· 85
(5) αS-AuNP/Graphene Oxide sheets for Hybrid sheets for photothermal cancer therapy ····· 91
II-4. Conclusions····· 103

Part III. Free-standing Gold-nanoparticle Monolayer Film Fabricated via Protein Self-assembly of α-Synuclein

III-1. Introduction····· 104
III-2. Experimental Section····· 105
(1) Fabrication of free-standing αS-AuNP Film ····· 105
(2) Cutting PC substrate into 2-D shape ····· 106
(3) Preparation of microfluidic devices for micro-patterning of αS-AuNP film ····· 107
(4) Micro-patterning of αS-AuNP monolayer film ····· 107
(5) Testing of AuNP film formation with bovine serum albumin (BSA), amyloid-β (Aβ), κ-casein (κCN), and β-2 microglobulin (β_2M)····· 108
(6) Flexibility of the αS-AuNP monolayer film ····· 109

(7) Conformal contact of the αS-AuNP film ····· 109
(8) Stability of the αS-AuNP film ····· 109
(9) Formation of wafer-scale αS-AuNP films ····· 110
(10) Fabrication of double-component AuNP films ····· 110
III-3. Results and Discussion ····· 111
(1) Free-standing film of αS-AuNPs ····· 111
(2) The role of αS for the fabrication of free-standing film ····· 116
(2)-1. Interaction between αS-AuNP ····· 116
(2)-2. Interaction between αS-AuNP and PC substrate ····· 118
(2)-3. Interaction between αS-AuNP and αS-AuNP ····· 122
(3) Optical property of αS-AuNP free-standing film ····· 124
(4) Flexibility of αS-AuNP free-standing film ····· 126
(5) Stability of αS-AuNP free-standing film ····· 128
(6) Patterning of αS-AuNP free-standing film ····· 130
(7) Fabrication of double-component AuNP film ····· 132
III-4. Conclusions ····· 134

References ····· 135

List of Tables

Table 1. Particle density of αS-AuNPs adsorbed on various

substrates ····· 27

Table 2. Evaluation of water contact angles of various substrates coated with αS-AuNP single-layer ····· 32

List of Figures

Figure 1. Interaction between αS and AuNP ····· 4

Figure 2. αS-AuNP single-layer on SiO_2 substrates ····· 15

Figure 3. pH effect on the close-packed single-layer coating of αS-AuNPs ····· 17

Figure 4. SEM images of αS-AuNPs adsorbed onto Si/SiO2 wafer at various pHs ····· 18

Figure 5. SEM images of αS-AuNPs adsorbed onto PMMA substrate at various pHs ····· 19

Figure 6. SEM images of αS-AuNPs adsorbed onto GaAs wafer at various pHs ····· 20

Figure 7. pH effect on the hydrodynamic diameter of αS-AuNP (10-nm AuNP) ····· 22

Figure 8. The pH dependence of particle density ····· 23

Figure 9. AFM analysis result of αS-AuNP single layer on multiple substrates ····· 26

Figure 10. XPS analysis result of various substrates coated with αS-AuNP single layer ····· 30

Figure 11. Contact angle measurement ····· 31

Figure 12. Patterning AuNP single layer with e-beam lithography ··· 35

Figure 13. AuNP single-layer coats over diverse 3D substrates ····· 37

Figure 14. Adsorbed αS-AuNPs single layer on SiO_2 gate ·····59

Figure 15. Transfer characteristics of αS-AuNPs based OFETs ·····61

Figure 16. Summarized results of transfer characteristics of OFETs ·····64

Figure 17. Programming and erasing tests of OFETs ·····65

Figure 18. Retention characteristics of αS-AuNP based OFETs ····· 68

Figure 19. Flexible Flash memory development ····· 71

Figure 20. Programming and retention time test of αS-AuNP-based flexible OFET memory ····· 73

Figure 21. Adsorption of αS-AuNP single layer on CNT and O_2 plasma treatment ····· 77

Figure 22. Electrocatalysis of O_2-plasma treated AuNP-CNT ·····78

Figure 23. αS-AuNP single layer on TiO2 microsphere and biosilicification ····· 82

Figure 24. αS-AuNP satellites on TiO_2 microsphere and dye-sensitized solar cells ····· 84

Figure 25. Cell immobilization on the substrates pre-coated with biocompatible αS-AuNPs ····· 87

Figure 26. 3-D cell culture in αS-AuNPs single layer coated PDMS micro-channels ····· 90

Figure 27. Characterization of αS-AuNPs and AuNP/GO hybrid sheets …… 94

Figure 28. Plasmon coupling and optical property of AuNP/GO hybrid sheets……... 96

Figure 29. Adhesion of AuNP/GO sheets on MSC surface …….. 99

Figure 30. In vivo photothermal therapy result of MSC-AuNP/GO sheet ……... 102

Figure 31. Flexible free-standing αS-AuNP monolayer films ……… 115

Figure 32. Coating AuNPs with αS …… 117

Figure 33. Tests of protein-AuNP monolayer adsorption …… 120

Figure 34. Optimization of film formation …… 121

Figure 35. Interaction between αS-AuNPs …… 123

Figure 36. NP size dependency of optical properties of αS-AuNP monolayer films …… 125

Figure 37. Conformal contact of αS-AuNP free-standing film …… 127

Figure 38. Stability of αS-AuNP free-standing film …….. 129

Figure 39. Patterning of αS-AuNP film …….. 131

Figure 40. Fabrication of double-component films …….. 133

Scheme 1. Single-layer Adsorption of αS-AuNPs …… 14

Scheme 2. Schematic representation of omni-adhesive property of αS-AuNPs …… 26

Scheme 3. Schematic representation of fabrication of memory

transistor ····· 57

Scheme 4. Schematic illustration of AuNP/GO sheets attached on tumor-tropic MSCs ····· 92

Scheme 5. Schematic diagram showing the fabrication strategy of free-floating αS-AuNP monolayer film·····113

Part I. Omni-adhesive property of α-synculein-gold nanoparticle complex

I-1. Introduction

(1) Two-dimensional organization of nanoparticles

Organization of nanoparticles (NPs) onto material surface is an essential process to utilize chemical and electrical properties of NPs in high-performance devices. For that purpose, many strategies have been suggested including charge interaction [1], Langmuir-Schaefer transfer [2], Langmuir-Blodgett technique [3], and thermal annealing [4], and applied for developing nano-devices such as optoelectronic sensors and low-power consumption memories. However, for widespread practical applications, it is needed to develop a generalizable method for NP organization onto various substrates, satisfying several requirements: (i) universal feasibility regardless of substrate nature, (ii) versatile applicability to multi-dimensional/-scale substrates, and (iii) mild reaction condition to minimize damage on target substrates. To meet these demands, universal adhesive molecules can be suggested as an effective tool for NP organization onto surfaces.

(2) Generalizable surface functionalization

As a means of generalizable surface functionalization, synthetic [5] or bio-inspired polymers [6] has been studied as universal adhesive molecules. In particular, utilization of mussel-inspired polymer, polydopamine, was found to be an efficient method for surface functionalization in various applications such as high power Li ion battery fabrication, bio-functionalization, and micro-fluidic device fabrication [7-9]. Recently, utilization of polydopamine showed possibility to organize NPs onto various 3-dimensional (3-D) substrates, but the approach resulted in uncontrolled NP immobilization in multi-layer [10].

(3) α-synuclein, an intrinsically disordered protein

α-synculein (αS) is well known as the major constituent of Lewy bodies, which is the pathological hallmark of Parkinson's disease. In Lewy bodies, αS is obsereved as amyloid fibrils produced via protein-self assembly of αS molecules. The protein is also a member of intrinsically disordered proteins (IDPs) which have been characterized by multiple partner interactions enabled by their structural plasticity [11-13]. This multiple interacting property is critical for IDPs to involve in diverse biological activities from transcription to multi-protein assembly [13]. Although physiological role of αS has not defined yet, αS has shown its multiple partner interactions from synthetic to natural molecules including eosin [14], coomassie brilliant blue [15], dequalinium [16], phthalocyanine tetrasulfonate (PcTS) [17], tau [18],

amyloid-β (Aβ) [19], synaptobrevin-2 [20], firefly luciferase [21], glutathione peroxidase [22], lipids [12], etc.

(4) Interaction between αS and gold nanoparticle

αS, which consists of 140 amino acids, can be divide into three domains of the basic N-terminus, the hydrophobic middle segment of non-amyloid-β component (NAC), and the acidic C-terminus [23]. Due to the negative charged surface of citrate-capped gold nanoparticles (AuNPs), the positively charged N-terminus was demonstrated to be the main region for the interaction with AuNPs [24,25] (Figure 1). It was suggested that the interaction between αS and AuNPs has enabled fabrication of αS-encapsulated AuNP (αS-AuNP) conjugates [24,25]. In other previous studies, αS mutant with cystein in C-teriminas was used to fabricate αS-AuNP, which was enabled by covalent-bonding between Au and cysteine residue. The cystein based αS-AuNP s were employed to align AuNPs into the pea-pod type 1-D nanochains [26] and the closely packed 2-D monolayer sheet on a glass capable of detecting metal ions in the presence of the metal chelator of PcTS [27].

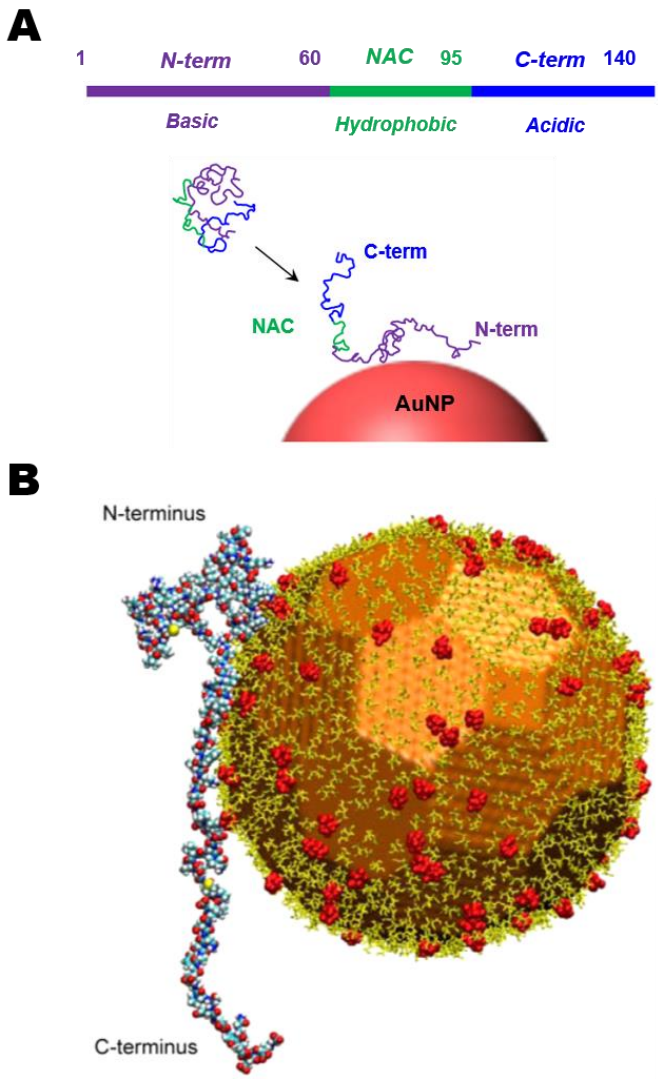

Figure 1. Interaction between αS and AuNP. (a) Scheme of αS orientation upon its binding onto AuNP. Three distinctive domains in αS's primary structure are represented as the basic N-terminus (violet), the hydrophobic non-amyloid-β component (NAC) (green), and the acidic C-terminus (blue). (b) VMD rendering of α-syn's simulated interaction with individual citrate capped AuNPs. [Lin et al. J. Phys. Chem. **119** (2015) 21035-21043]

I-2. Experimental Section

(1) Purification of αS

Wild-type human αS protein was prepared as the procedure reported in the previous paper [28]. Briefly, αS gene cloned in pRK172 vector was transformed into *Escherichia coli* BL21 (DE3) for αS over-expression. The heat-treated cell lysate was subjected to successive purifications using DEAE-Sephacel anion-exchange, Sephacryl S-200 size-exclusion, and S-Sepharose cation-exchange chromatography. The purified αS was dialyzed against total 12 L of fresh 20 mM MES at pH 6.5 with three changes, and stored in aliquots at a concentration of 1 mg/ml at -80ºC.

(2) Substrate preparation

n-Si (Siltron Inc., Korea), GaAs (University Wafer, Boston, MA), fluorine-doped tin oxide (FTO, Pilkington, Toledo), SiO_2 (Global Wafers Co., Ltd., China), mica, graphite (NGS Naturgraphit GmbH, Germany), glass (Corning, Corning, NY), quartz (Perkin Elmer, Waltham, MA), Au (Phasis, Switzerland), polyethylene terephthalate (PET) were cleaned ultrasonically in deionized water (DW) or isopropanol (IPA), and purged with nitrogen gas. Polystyrene (Sigma-Aldrich, M.W. = 38k, 4 wt % in xylene), polycarbonate (Sigma-Aldrich, M.W. = 64k, 5 wt % in chloroform), poly(methyl methacrylate) (Microchem, M.W. = 950k, 5 wt % in anisole) were spin-coated

on cleaned Si/SiO_2 wafer at 4,000 rpm for 30 s. Each polymer was annealed over its glass temperature (T_g) for 30 s. Polydimethylsiloxane (PDMS, Sylgard 184, Dow Corning, Midland, MI) was prepared by mixing pre-polymer and curing agent at 10:1 and subsequent incubation of the mixture at 80^{o}C for 30 min. The cured PDMS was cleaned in DW with ultra-sonication. Al_2O_3 and TiO_2 were prepared by atomic layer deposition (ALD) on O_2-plasma cleaned SiO_2 wafer and washed ultrasonically in IPA. Fluorinated wafer was prepared by the reaction between 1H,1H,2H,2H–perfluorooctyltriethoxysilane (98%, Sigma-Aldrich) and O_2-plasma (60 W, 45 sccm, 10 min) cleaned SiO_2 wafer at 80^{o}C for 12 hr. The jewelry crystals (2854 butterfly flat back, crystal F 001, Swarovski element) were cleaned ultrasonically in IPA for several minutes and purged with nitrogen gas.

(3) X-ray photoelectron spectroscopy (XPS) characterization

XPS spectra were obtained using AXIS Ultra DLD (Kratos, UK) with a monochromatic Mg Ka (1253 eV) X-ray source of 40 eV pass energy under ultra-high vacuum (~10^{-9} torr). High-resolution scans were acquired from 390 to 410 eV and 80 to 90 eV for analysis of N 1s peak (~399.5 eV) and Au $4f_{7/2,5/2}$ (~84.1/84.9 eV). Ratio between Au and N was calculated with the peak areas and the atomic sensitivity factor.

(4) Atomic force microscope (AFM) analysis

Substrates were cut with 1 x 1 cm^2 in size and prepared following the cleaning procedures. Then, α-synuclein-coated gold nanoparticles (αS-AuNP) in 200 μl of 50 mM citrate (pH 4.5) were placed on each substrate. The prepared samples were subjected to AFM (Multimode 8, Bruker, Billerica, MA) analysis using tapping mode Nanoscope V system (Bruker). For height measurement, each sample was smoothly scratched with a PET plate prior to the AFM measurement.

(5) Contact angle measurements

Samples were prepared according to the same procedures as the AFM experiment. All the contact angles and the images of water droplets were monitored by using a drop shape analyzer (DSA100, Kruss, Germany). The static contact angle was examined after storing the samples at a humid chamber for 30 min to prevent evaporation.

(6) Large-area monolayer formation of αS-AuNP adsorbed on SiO_2 wafer

$αS\text{-}AuNP_{10nm}$ was prepared by incubating of 1 ml of αS at 1 mg/ml and 8 ml of the AuNP colloidal solution. After the centrifugation, the αS-AuNP pellet was resuspended with 2 ml of 50 mM citrate (pH 4.5), which was placed onto the SiO_2 wafer pre-cleaned via sonication in IPA and O_2-plasma treatment to remove organic contaminants. After incubation at 40°C for 3 hr in a humid

chamber, the sample was thoroughly washed with 20% methanol at 4ºC and dried with nitrogen gas.

(7) Field-emission scanning electron microscope (FE-SEM) analysis

All the samples were completely dried in a desiccator and coated with a 2-nm-thick layer of platinum by a sputter coater (BAL-TEC/SCD 005 sputter coater, Switzerland). The samples were then analyzed with FE-SEM (SUPRA 55VP, Carl Zeiss, Germany) at 2.0 kV.

(8) Transmission electron microscope (TEM) analysis

An aliquot of samples (10 μl) was placed onto carbon-coated 200-mesh copper grids (Ted Pella Inc. CA). After washing the grid with DW, the air-dried grid was examined with TEM (JEM 1010, JEOL, Japan).

(9) Computational calculation for isoelectric point (pI) of αS

Isoelectric point (pI) of αS was obtained as an average value calculated with 15 different programs such as Isoelectric Point Calculator (IPC) protein, IPC peptide, Toseland, Thurlkill, Nozaki Tan, DTASelect, EMBOSS, Grimsley, Patrickios, Rodwell, Sillero, Solomon, Lehninger, Wikipedia, and ProMoST (http://isoelectric.ovh.org/).

(10) High-density single-layer coating of αS-AuNPs onto various materials

The high-density single-layered coat of αS-AuNPs was formed onto bare AuNPs (BBI solutions, UK), carbon nanotubes (CNTs; Sigm-Aldrich), carbon nanofibers (CNFs; Sigm-Aldrich), or 500-nm titanium dioxide (TiO_2; EPR-Ti-0.5, EPRUI Nanoparticles & Microspheres Co. Ltd, China). Following an incubation at 40°C for 2 hr with agitation at 200 rpm, the αS-mediated three types of AuNP-AuNP core-satellites were generated in 800 μl of 10 mM MES at pH 5.5 by incubating the following mixtures: αS-$AuNP_{30nm}$ in a pellet and 400 μl of bare $AuNPs_{5nm}$ colloidal solution (type 1), αS-$AuNP_{30nm}$ in a pellet and 400 μl of bare $AuNPs_{10nm}$ colloidal solution (type 2), and αS-$AuNP_{100nm}$ in a pellet and 400 μl of bare $AuNPs_{100nm}$ colloidal solution (type 3). After the incubation, the samples were centrifuged at 16,100 x g for 1 min with fresh 20 mM MES at pH 6.5 three times to remove free AuNPs. Each αS-AuNP pellet was prepared with 200 μl of AuNP colloid solution and 25 μl of αS (1 mg/ml). For the αS-AuNP coating on CNT, 0.226 mg of multi-walled CNTs were incubated with a pellet of αS-$AuNP_{10nm}$ (400-μl AuNP and 50-μl αS) in 200 μl of 50 mM citrate (pH 4.5) at 40°C for 2.5 hr with agitation at 200 rpm after sonication for 1 min. The samples were then centrifuged at 16,100 x g for 15 min with fresh DW three times. For the αS-AuNP coating on CNF, the mixture of 15 μg of CNF (Sigma-Aldrich) and a pellet of αS-$AuNP_{5nm}$ (three sets of 400-μl AuNP and 50-μl αS) was

incubated in 200 μl of 50 mM citrate at 40ºC for 3 hr. The products were washed via centrifugation with fresh DW at 16,100 x g for 15 min three times. The CNFs were solubilized by the pre-treatment, in which 3 mg of CNFs (sigma Aldrich) were refluxed for 24 hr under sonication (bath-type) in a solution composed of 2.5 ml of sulfuric acid, 5 ml of nitric acid, and 2.5 ml DW. For the αS-AuNP coating on TiO_2 microsphere (EPRUI Nanoparticles & Microspheres Co. Ltd), the TiO_2 spheres (10 μl) were incubated with a pellet of αS-$AuNP_{10nm}$ (three sets of 400-μl AuNP and 50-μl αS) in 200 μl of 50 mM citrate (pH 4.5) at 40ºC for 2.5 hr. Micro-channels and microwells were filled with αS-AuNP solution in 50 mM citrate at pH 4.5. After incubation in a humid chamber at 40ºC for 3 hr, the micro-channels and microwells were completely washed with 20% methanol at 4ºC to remove free αS-AuNPs, and then stored in a desiccator.

(11) Electron-beam (e-beam) lithography for 2-Dimensional patterning of αS-AuNPs in single-layer

PMMA (Microchem, M.W. = 950k, 5 wt % in anisole) was spin-coated on a cleaned Si/SiO_2 wafer at 4,000 rpm for 40 s. On the PMMA-coated wafer, e-beam was irradiated to the designed patterns drawn with computer-aided design (CAD) software (NPGS, DesignCAD Express 16.2). After the e-beam exposure, the PMMA-coated wafer was dipped into methyl isobutyl ketone/IPA solution for 45 s to remove the e-beam exposed region. Following the development process, the sample was thoroughly washed with IPA and

dried with nitrogen gas. The patterns were treated with O_2 plasma (60 W, 45 sccm, 1 min) to remove organic residues on the SiO_2 surface, which results in the developed patterns hydrophilic to exhibit conformal contact toward the particle-containing aqueous solution. Then, αS-AuNP$_{10nm}$ in 50 mM citrate at pH 4.5 was placed onto the patterned substrate, and the sample was incubated in a humid chamber at 40^{o}C for 3 hr. After the particle adsorption, the remnants were washed off with 20% methanol at 4^{o}C and the substrate was dried with nitrogen gas. Before the lift-off process, the substrate was entirely exposed to O_2 plasma (60 W, 45 sccm, 11 min) to prevent cross-linking between the protein molecules. Finally, the whole substrate was dipped into acetone with gentle agitation to remove the PMMA layer and dried with nitrogen gas purging.

(12) Fabrication of micro-fluidic device and 3-D microwell array

A PDMS master mold for micro-channels was prepared using soft lithography and the previously reported techniques [29]. In brief, O_2 plasma-treated (50 W, 45 sccm, 5 min) Si wafer was spin-coated with negative photoresist (SU-8 5, Microchem, Boston, MA), and the wafer was pre-baked at 95^{o}C for 10 min. Following an exposure with 405 nm ultraviolet (UV) light (Shinu MST, Korea) at 500 mJ, the wafer was baked at 95^{o}C for 10 min. The unexposed region of the photoresist was removed with SU-8 developer (Microchem). Then, the resulting wafer was used as a master mold for PDMS precursor Sylgard 184 (Dow Corning, Midland, MI). The precursor solution with curing

agents was poured on the wafer, baked at 90°C for 40 min, and replicated. In the case of micro-fluidic device, the PDMS mold was punched for inlets and reservoirs, and attached on glass slide after O_2 plasma treatment (50 w, 45 sccm, 1 min).

I-3. Results and Discussion

(1) Single-layer Adsorption of αS-AuNPs

The αS-AuNP conjugates were prepared by incubating the mixture of soluble αS and colloidal AuNPs in 20 mM Mes (pH 6.5) for 12 hr at 4°C [30] (Scheme 1). The high-density single-layer coating of αS-AuNPs was achieved via the adsorption of the conjugates at an acidic pH of 4.5 and subsequent thorough washing with either water or 20% methanol. The close-packed αS-AuNP monolayer on the surface of Si/SiO_2 wafer was examined with atomic force microscope (AFM) (Figure 2a) and scanning electron microscope (SEM) (Figure 2b). This solution-based procedure permitted the conjugates to cover the entire surface of 4-inch wafer to a single layer (Figure 2b, inset). This single-layer formation could be attributed to the peculiar amino acid sequence of αS exposed from the conjugates and its preferential interation with the surface to the other conjugates (Scheme 1). In the primary structure of αS as divided into three regions such as the basic N-terminus, the hydrophobic middle segment of non-amyloid-β component (NAC), and the acidic C-

terminus, the positively charged N-terminal region was previously demonstrated to be responsible for the αS binding to citrate-capped negatively charged AuNPs [24]. Consequently, a long stretch of the hydrophobic NAC and the negatively charged C-terminal region would be exposed by possibly forming a hydrophobic shell comprised of NACs with the extended acidic segments, which could play a critical role for exhibiting the adsorption characteristics.

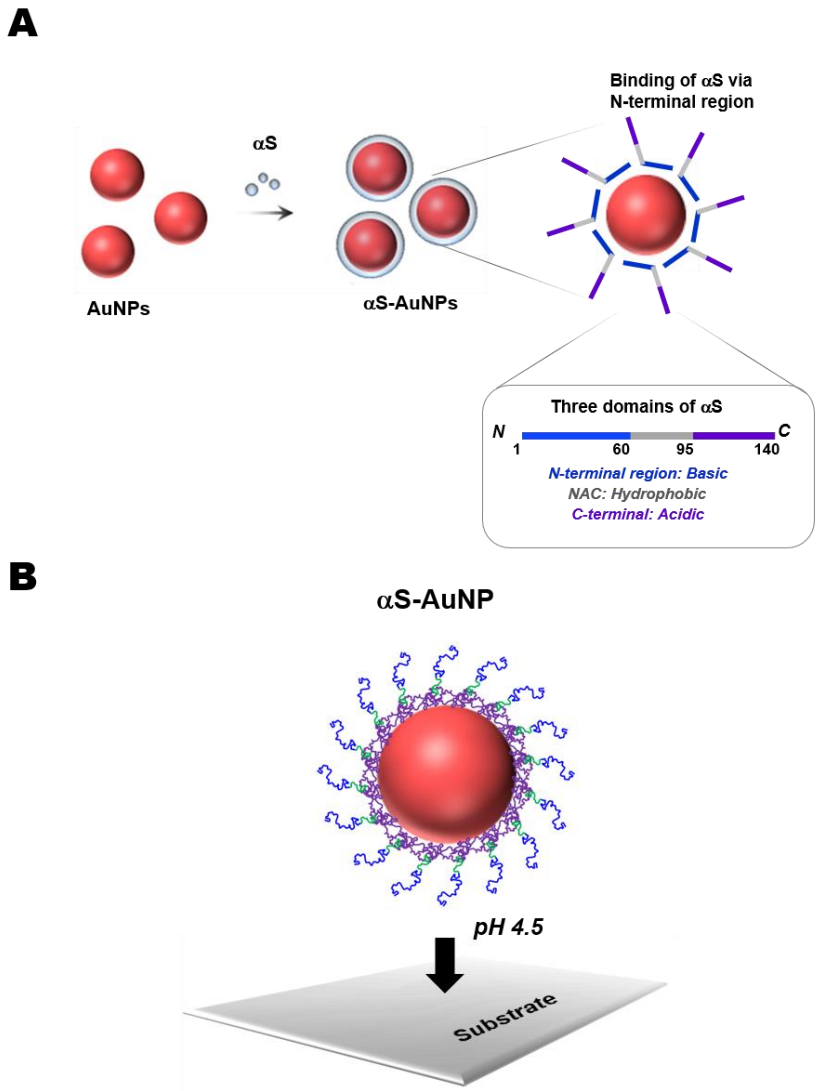

Scheme 1. Single-layer Adsorption of αS-AuNPs. (a) Schematic representation of encapsulation of AuNPs with αS. **(**b) Drawing of αS-AuNP adsorption onto substrate via conformational plasticity of αS at the pH of 4.5.

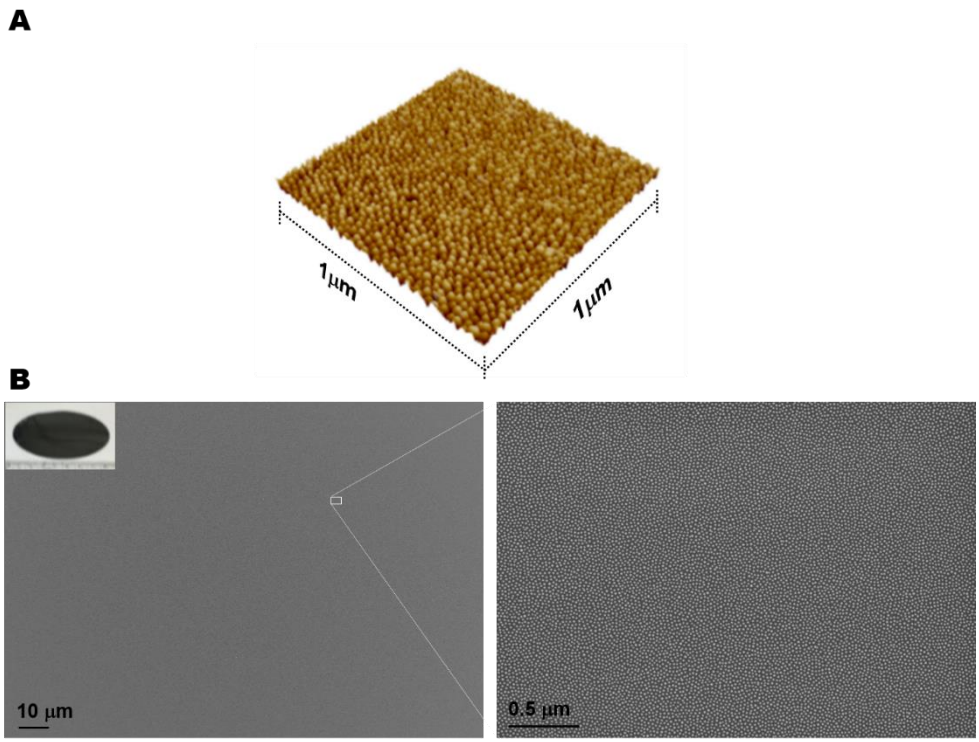

Figure 2. αS-AuNP single-layer on SiO_2 substrate. (a) 3-D AFM image showing the tightly packed monolayer of αS-AuNPs adsorbed onto Si/SiO_2 wafer. (b) FE-SEM image of the αS-AuNP single-layer on SiO2 wafer. A 4-inch wafer coated with αS-AuNPs is presented in inset. Low- (left) and high- (right) magnification images are presented.

(2) pH-dependence of Single-layer Adsorption of αS-AuNPs

The adsoption of αS-AuNPs was shown to be highly dependent upon pH. Upon pH variation from 5.0 to 3.0, theoretical evaluation of the regional charge distribution of αS has indicated that the C-terminal region (5 aspartic acid and 10 glutamic acid residues) particularly exhibits a drastic change in charge from negative to positive state. On the other hand, the positive charges of the N-terminus (11 lysine residues) are mostly maintained with a noticealbe disappearance of negative charges (Figure 3a). Based on the computational calculations, pI values of the N-terminal and the NAC/C-terminal region were estimated to be 9.96 and 3.64, respectively. Concerning the exposed NAC/C-terminal stretch and the hydrophobic shell of NAC which might shield any ionic influence from the core construct between AuNP and the basic N-terminus, the adsoption behavior of the αS-AuNP conjugates was expected to be dramatically affected around pH 3.64. As a matter of fact, the conjugates actually agglomerated extensively at pH 3.5 and 4.0 by producing multilayered amorphous aggregates on the surface of three differenent substrates such as SiO_2 (Figure 3b and 4), poly(methyl methacrylate) (PMMA) (Figure 3b and 5), and GaAs (Figure 3b and 6). This result suggests that the agglomeration is independent of the chemical nature of the substrates but due to the self-associative property of αS-AuNPs present at a neutrally charged state.

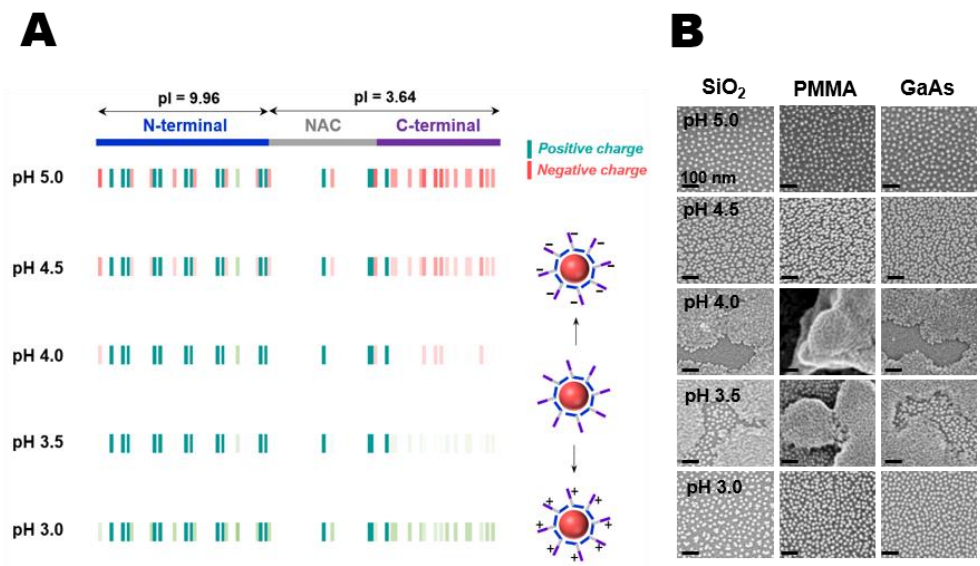

Figure 3. pH effect on the close-packed single-layer coating of αS-AuNPs. (a) Diagrams showing the charge distribution of amino acid residues of αS at various pHs. The αS sequence is divided into three domains such as N-terminal (blue), middle NAC (gray), and C-terminal (violet) region. Positively (green) and negatively (red) charged R groups are presented at various pHs ranging from 3.0 to 5.0 at intervals of 0.5. Schematic representation of the αS's charge distribution on the surface of AuNP at specific pHs indicated. (b) FE-SEM images of the adsorbed αS-AuNPs onto three different substrates such as Si/SiO_2 (left column), PMMA (middle column), and GaAs (right column) at various pHs ranging from 3.0 to 5.0.

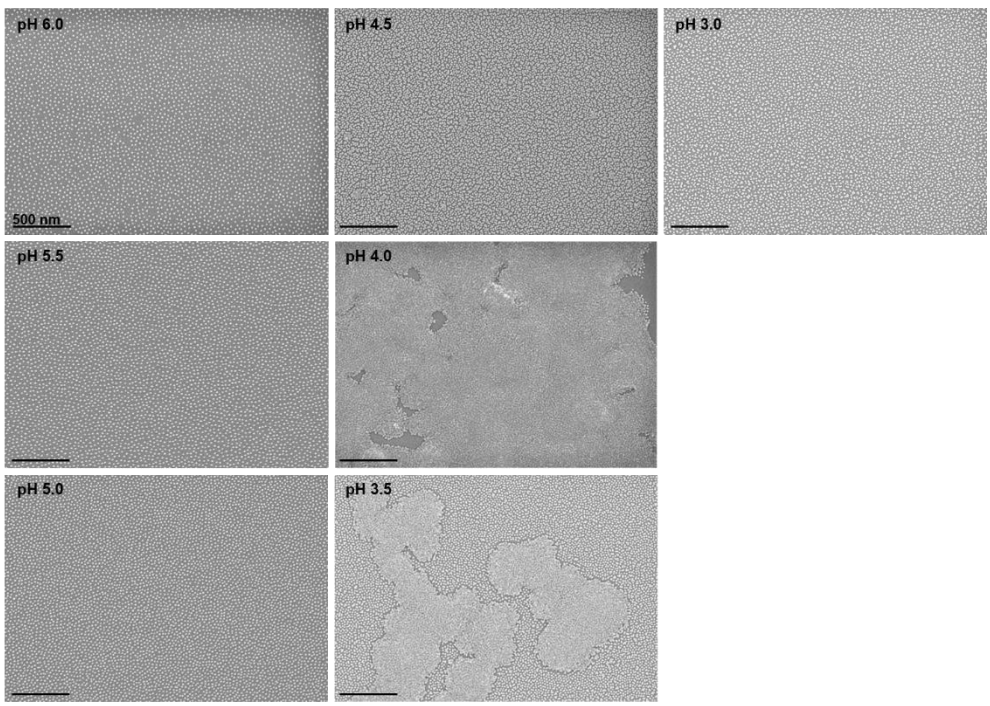

Figure 4. SEM images of αS-AuNPs adsorbed onto Si/SiO2 wafer at various pHs. A double-component buffer solution comprising citric acid and sodium phosphate dibasic was employed to adjust the pH indicated between 3.0 and 6.0.

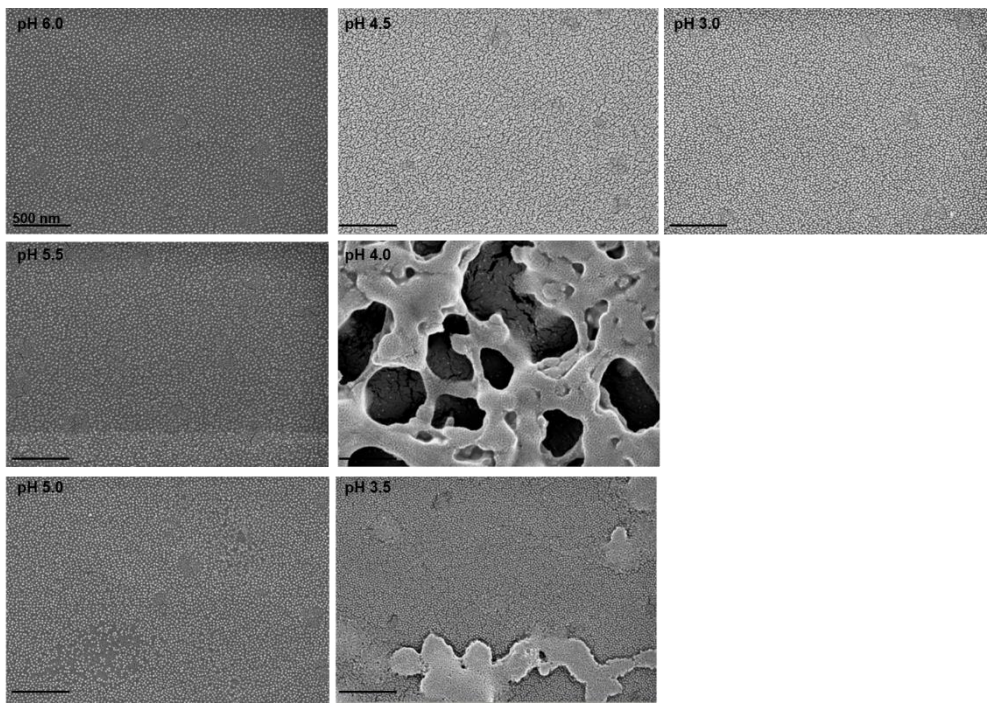

Figure 5. SEM images of αS-AuNPs adsorbed onto PMMA substrate at various pHs. The pHs were maintained in the double-component buffer solution (citric acid/sodium phosphate dibasic).

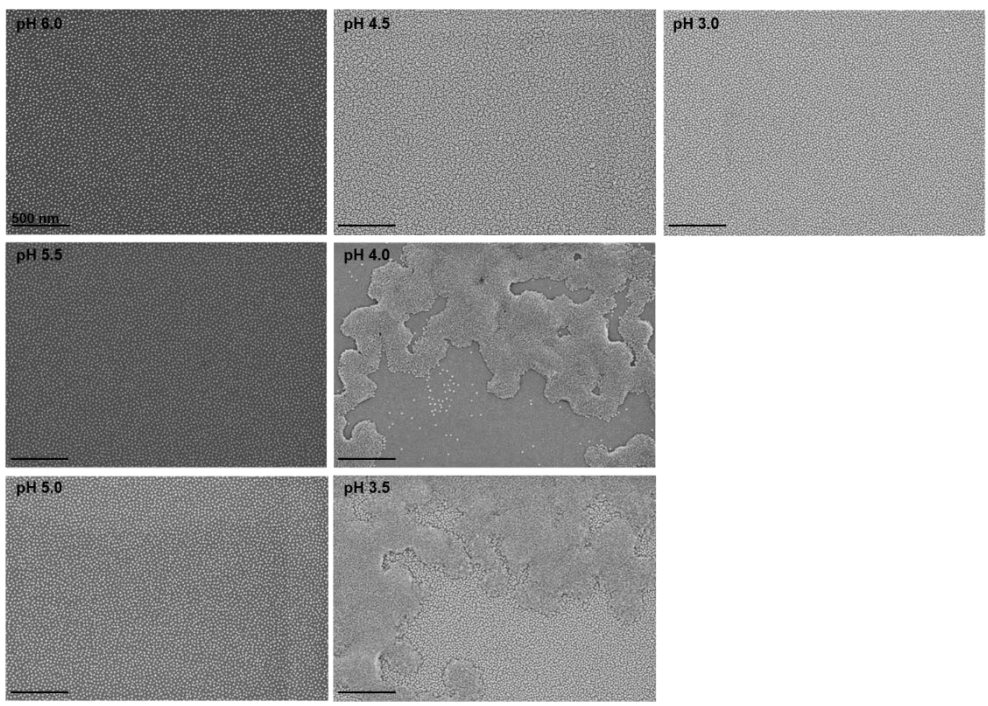

Figure 6. SEM images of αS-AuNPs adsorbed onto GaAs wafer at various pHs. The pHs were maintained in the double-component buffer solution (citric acid/sodium phosphate dibasic).

Intriguingly, at the pHs other than 3.5 and 4.0, the αS-AuNP conjugates formed the single-layered coat over all the three substrates. The tight packing, however, was obtained at pH 4.5 where the conjugates would allow mutual proximity on the surface but prevent their agglomeration. As pH increased above 4.5 up to 6.0, the particle packing became sparse as the conjugates have increased their hydrodynamic diameter (Figure 7) with the emergence of negative charges which could make the conjugates repulsive. Based on the same reason, at the acidic pH of 3.0, the particles also produced the monolayer coat over the substrates, where the αS-AuNPs would also become repulsive but with the positive charges in this case. This bimodal response of the pH-dependent adsorption behavior of αS-AuNPs, therefore, appears to be intrinsic toward the unfolded protein of αS which cannot be replaced by other proteins such as bovine serum albumin and amyloidogenic proteins including amyloid-β, β2-microglobulin, and κ-casein [30]. For the quantitative assessment, the particle adsorption at various pHs were analyzed with the SEM images. As pH decreased from 6.0 to 4.5, the particle density of αS-AuNPs adsorbed on SiO_2 increased: 649.0 ± 9.0 μm^{-2} (pH 6.0), 765.5 ± 7.9 μm^{-2} (pH 5.5), 1016.2 ± 55.3 μm^{-2} (pH 5.0), and 1381.8 ± 47.3 μm^{-2} (pH 4.5) (Figure 8a). Besides the particle agglomeration at pH 4.0 and 3.5, the sigle-layer adsorption returned at pH 3.0 with the density of 1052.7 ± 37.2 μm^{-2}. The same bimodal pH-dependent adsorption profiles were observed with the other substrates of PMMA (Figure 8b) and GaAs (Figure 8c).

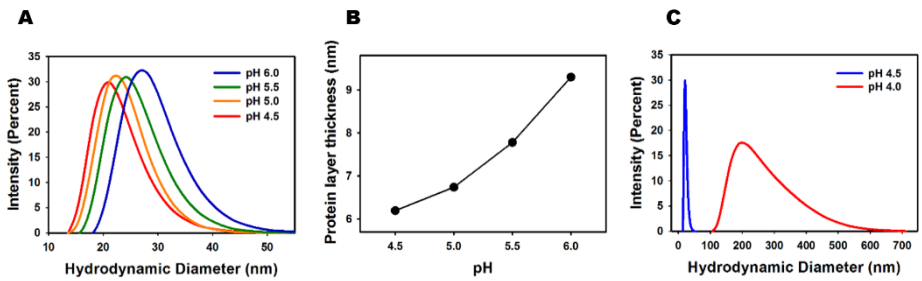

Figure 7. pH effect on the hydrodynamic diameter of αS-AuNP (10-nm AuNP). (a) Statistical distribution of the hydrodynamic diameters of αS-AuNPs measured with DLS at various pHs indicated. (b) Thickness of αS layer on the αS-AuNP conjugates obtained via the DLS measurements. (c) DLS spectra of the αS-AuNPs at either pH 4.5 or 4.0. Large agglomeration of the conjugates was shown to occur at pH 4.0.

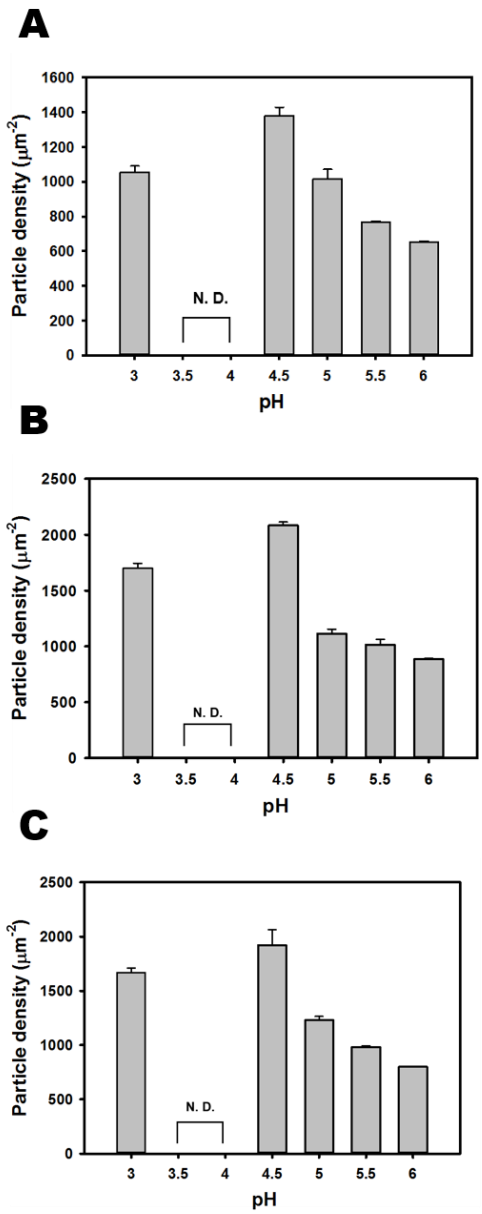

Figure 8. The pH dependence of particle density. Particle density of αS-AuNPs adsorbed on (a) SiO_2, (b) PMMA, (c) GaAs substrate at various pHs. At pH 3.5 and 4.0, the particle density was not determined due to the agglomeration of αS-AuNPs.

(3) Omni-adhesiveness of αS-AuNPs Producing the Close-packed Single-layer AuNP Coat over Multiple Substrates

Considering an amphipathic nature of the exposed NAC/C-terminal segment as well as the multiple ligand interaction property of αS due to its structural plasticity as an inherent characteristic of IDPs, the multiple adhesive ability of αS-AuNPs was examined with a diverse set of substrates. Impressively, the αS-AuNP conjugates adhered to virtually all the surfaces tested from organic to inorganic materials by producing the tightly packed single-layered coat regardless of the substrates' chemical identity. (Scheme 2) Those substrates include oxides (SiO_2, Al_2O_3, TiO_2, fluorine-doped tin oxide (FTO)), amorphous ceramic material (glass), semiconductors (Si, GaAs), metal (Au), polymers (polystyrene, PS; polyethylene terephthalate, PET; polycarbonate, PC; PMMA), polymeric organosilicon (polydimethylsiloxane, PDMS), carbon material (graphite), and natural minerals (quartz, mica). Based on the AFM images of the particle-coated surfaces as shown with SiO_2, Al_2O_3, TiO_2, glass, n-Si, GaAs, Au, PC, and PMMA, mica, PS, and p-Si data (Figure 9), all the substrates were conformally coated by the particles at pH 4.5 to a state of close-packed single-layer at an average density of 1402.44 ± 16.67 μm^{-2} (Table 1). Their height profiles, however, varied among the surfaces. Some of the maximum heights were measured even less than the size of 10-nm AuNPs adsorbed (Figure 9). This might be attributed to uneven and disparate trough levels of the uncoated surfaces due to the protein left on the surface after scraping off the coats with a PET stick.

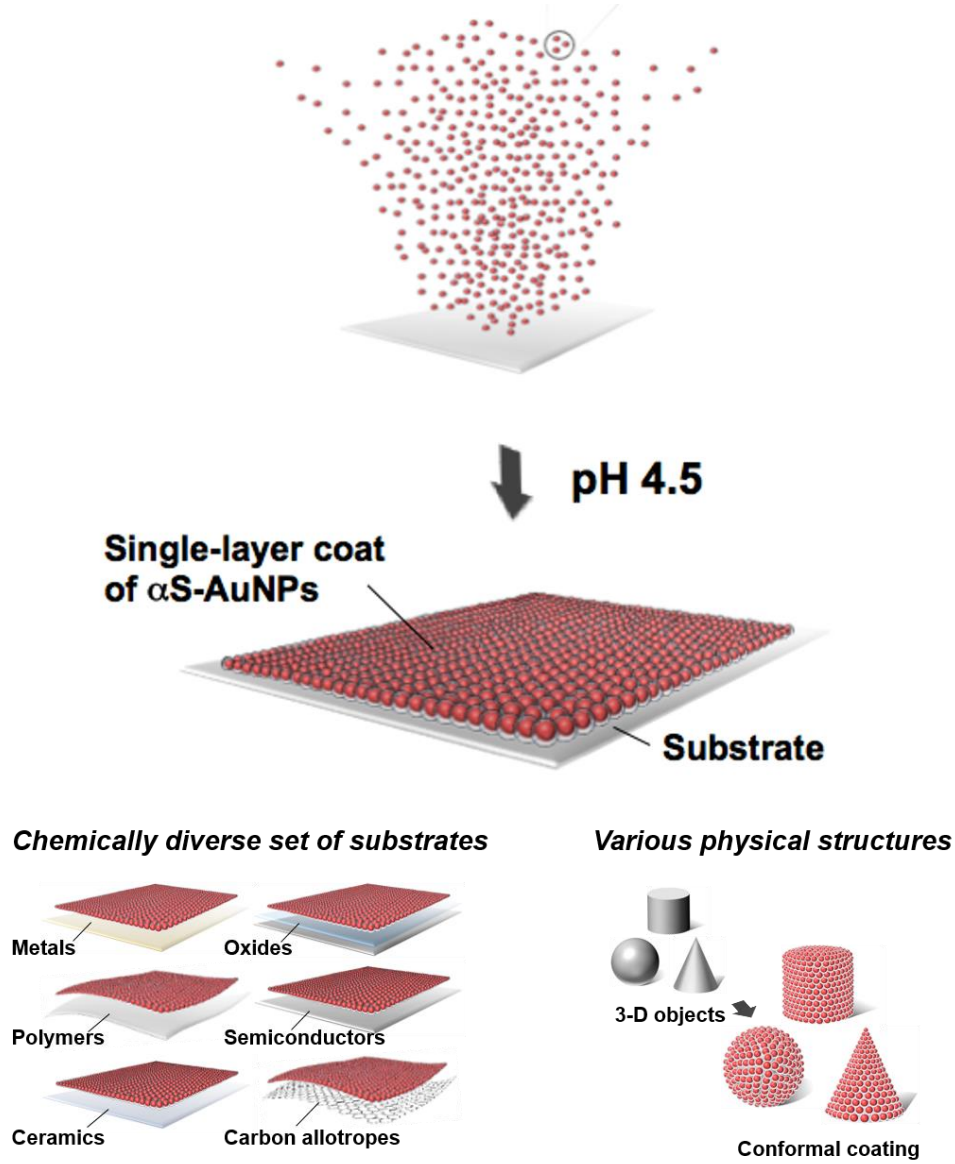

Scheme 2. Schematic representation of omni-adhesive property of αS-AuNPs.

The αS-AuNP adsorption leads to the conformal coating of the particles onto a chemically diverse set of substrates in various physical structures.

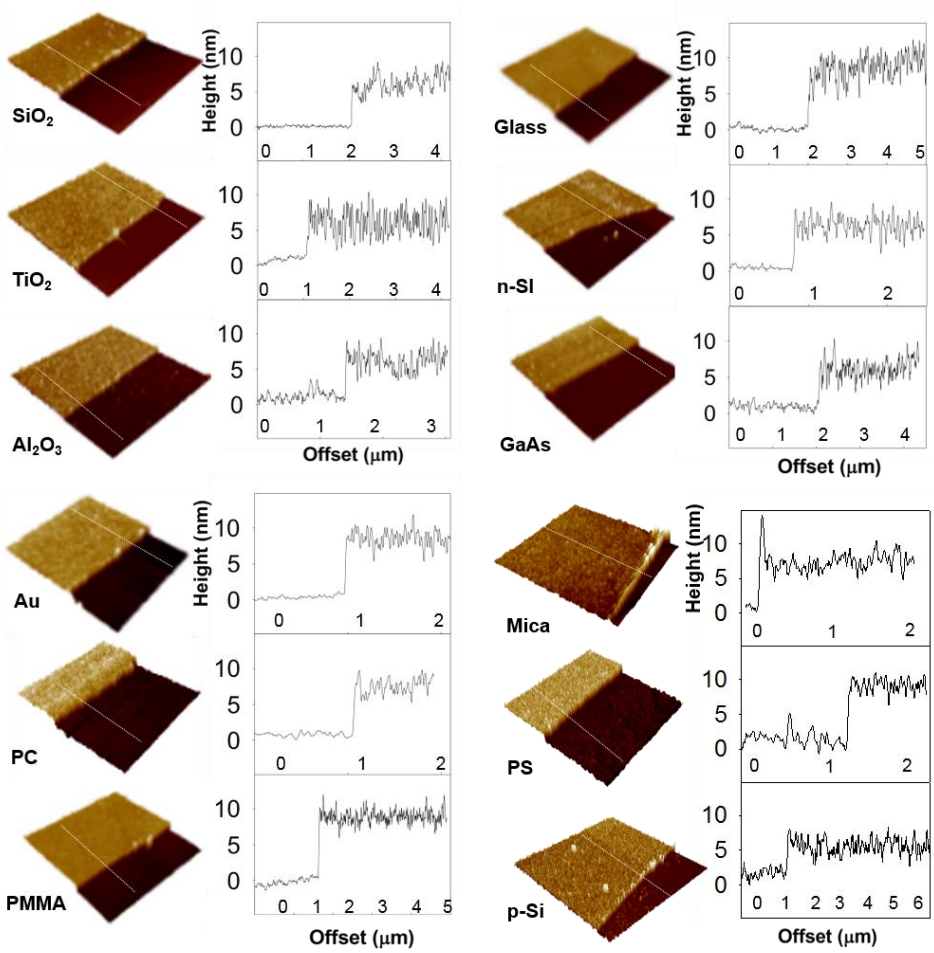

Figure 9. AFM analysis result of αS-AuNP single layer on multiple substrates.

(left) 3-D AFM image and (right) AFM height profile for each substrate.

Table 1. Particle density of αS-AuNPs adsorbed on various substrates (mean ± SD, n = 3).

Substrate	Particle density (μm^{-2})
SiO_2	1421.33 ± 12.22
TiO_2	1382.67 ± 32.58
Al_2O_3	1389.33 ± 32.33
Glass	1406.67 ± 26.03
n-Si	1402.67 ± 29.48
p-Si	1378.67 ± 22.03
GaAs	1416.00 ± 21.17
Au	1410.67 ± 12.22
Mica	1377.33 ± 32.58
PC	1426.67 ± 12.22
PMMA	1410.67 ± 16.65
PS	1406.67 ± 14.05
Average	1402.44 ± 16.67

The average particle density of αS-AuNPs are shown in the last low.

Analysis of chemical composition of the coated surfaces with X-ray photoelectron spectroscopy (XPS) revealed that αS-AuNP complexes were adsorbed intact onto the surfaces - SiO_2, Al_2O_3, TiO_2, glass, n-Si, GaAs, Au, PC, PMMA, FTO, PDMS, PS, PET, graphite, quartz, and mica - without any decomposition (Figure 10). From the spectra, those discrete signals of Au 4f doublets ($4f_{7/2}$ and $4f_{5/2}$) and N 1s singlet peaks yielded the Au-to-N (Au/N) ratios centered at 4.0 for all the substrates, indicating that those single-layered coats contained both AuNPs and αS at approximately the same proportion. Nonetheless, the binding energies of N 1s peaks still varied, suggesting that the coat proteins could experience different modes of structural adjustment upon the conjugate binding to the surfaces. The next water-based contact angle observation clearly demonstrated that not only the interfacial properties of the hydrophilic (SiO_2, mica, and FTO) and the hydrophobic (Fluorine-coat (F-coat), PC, and PS) surfaces were changed upon the αS-AuNP coating (Figure 11), but even the coated surfaces exhibited different contact angles (Table 2). This fact indicates that the αS molecules exposed on the coated surfaces might exist in different states in terms of their structural orientations. Since the protein has been bound to the particles noncovalently in the αS-AuNP conjugates, the conformational signals initiated from the proteins located at the interface between the surface and the adsorbing particle during a transient reversible binding period of the coating process could propagate laterally through the proteins surrounding the particle to the ones on the top and thus exposed from the coated surfaces. Therefore, the distinctive contact angles would reflect different types of multidentate interactions of αS to the

chemically diverse substrates and subsequent transfer of the conformational signals through the surface-restricted flexible proteins to the unique structural orientations of αS located atop the surface-bound conjugates. Taken together, these observations encourage us to suggest that the coating strategy with αS-AuNPs could be valued for its practical use to make functional graffiti of various nanoparticles onto diverse materials for multiple purposes.

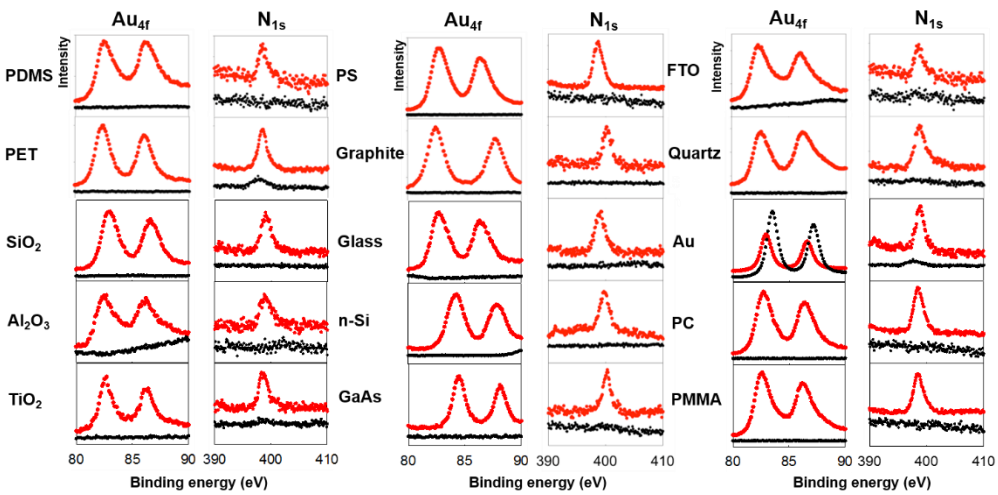

Figure 10. XPS analysis result of various substrates coated with αS-AuNP single layer. (left) Au 4f region and (right) N 1s region for each substrate.

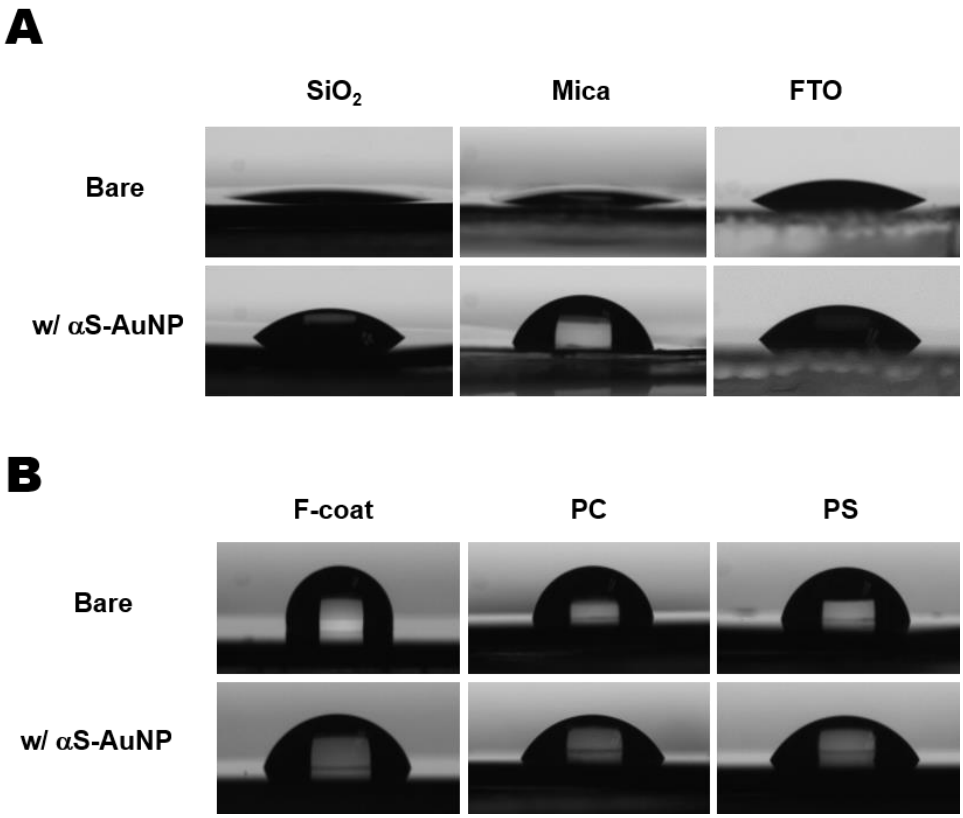

Figure 11. Contact angle measurement. (a) Optical image of the water droplets formed on the surfaces of hydrophilic substrates without (top) and with thee αS-AuNP single-layer coat (bottom). (b) Optical image of the water droplets formed on the surfaces of hydrophobic substrates without (top) and with thee αS-AuNP single-layer coat (bottom).

Table 2. Evaluation of water contact angles of various substrates coated with αS-AuNP single-layer.

	Bare surface θ_{adv} (θ_{stat})	αS-AuNP coated surface θ_{adv} (θ_{stat})
PMMA	71.6 (66.5)	63.7 (54.9)
PC	80.9 (75.5)	62.3 (58.3)
PS	88.0 (78.2)	65.5 (60.6)
PDMS	112.3 (102.9)	93.5 (88.8)
Fluorinated wafer	106.6 (95.2)	78.2 (71.7)
PET	73.7 (66.2)	66.3 (55.6)
SiO_2	<10	39.7 (24.5)
FTO	29.7 (27)	53.3 (48.6)
Mica	<10	67.9 (56.4)
Au	52.1 (40.1)	59.3 (46.5)

θ_{adv} and θ_{stat} are advancing and static contact angles, respectively.

(4) High-density Single-layer Coating of AuNPs over Multiple Geometric Shapes in 2-D and 3-D

High resolution patterning of NPs in 2-D is critical to utilize the diverse properties of NPs in the form of high-efficiency nanomaterials-based devices for the development of nano-electronics, sensor technology, and even cell-based biotechnology [31]. To pattern the AuNPs into various geometric shapes in 2-D, electron beam (e-beam) lithography technique was employed (Figure 12a). After PMMA-spin-coated Si/SiO_2 wafer was illuminated with e-beam in pre-defined patterns, the areas of PMMA exposed to e-beam were washed off with a developing solvent of methyl isobutyl ketone to reveal the underlying Si/SiO_2 surface in the patterns. The αS-AuNPs were then adsorbed onto an entire surface of the substrate. The final patterns imprinted with the conjugates were produced via the organic solvent treatment to lift off the remaining PMMA layer along with the particle conjugates. For the high-resolution pattering, O_2 plasma treatment was performed to remove the αS protein shell prior to the solvent treatment which would cause cross-linking between αS molecules. In Figure 12b, SEM image shows various geometric shapes patterned with AuNPs in the forms of lines (1-to-4 μm in width), rectangles (200 μm x 10-to-80 μm), and squares (0.5-to-80 μm x 0.5-to-80 μm). The particles were successfully patterned to give rise to a line with 100-nm width (Figure 3a, inset). Other shapes were also readily imprinted on the substrate in the forms of circles with 50-500 μm in diameter and equilateral triangles with side length of 1-50 μm. Although the patterning shown here

was conducted with a single type of substrate, the versatile adhesion property of αS-AuNP would permit the NP patterning to be imprinted on diverse material surfaces.

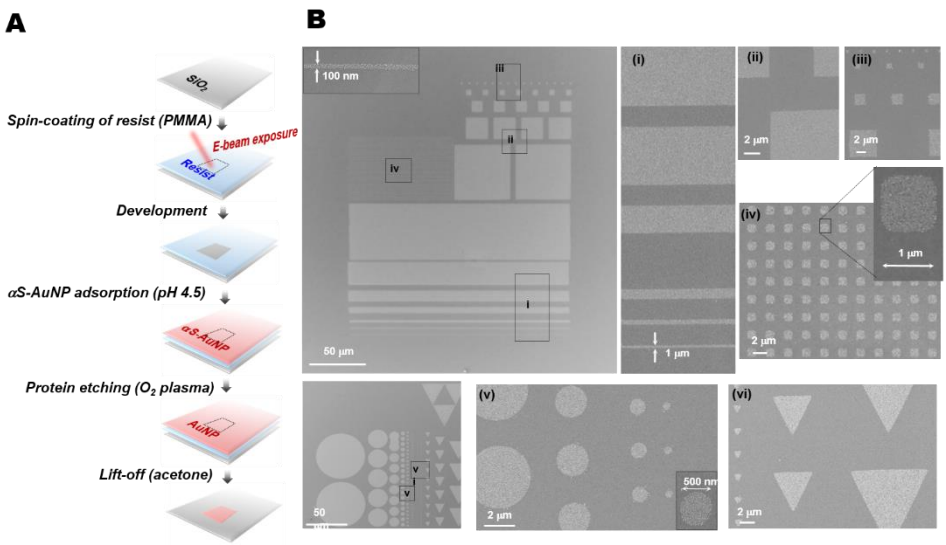

Figure 12. Patterning AuNP single layer with e-beam lithography. (a) Schematic representation of a procedure for the AuNP two-dimensional (2-D) patterning. The protocol consists of SiO_2 substrate preparation, spin-coating of resist, e-beam exposure, development, αS-AuNP adsorption, O_2 plasma treatment, and lift-off step. (b) SEM images of the αS-AuNP single-layer coats patterned in lines (1-to-4 μm in width), rectangles (200 μm x 10-to-80 μm), and squares (0.5-to-80 μm x 0.5-to-80 μm). A line pattern with the minimum width of 100 nm is shown in the inset.

In addition to 2-D patterning, our solution-based AuNP adsorption strategy also allows conformal immobilization of AuNPs onto spatially curved and/or physically inaccessible surfaces of 3-D objects in nano- to micro-scale. The αS-AuNPs containing either 5 or 10 nm particle were adsorbed to a single layer onto chemically diverse surfaces such as citrate-capped surface of larger AuNPs with a diameter of either 30 or 100 nm (Figure 13a), tubular surfaces of 10 nm carbon nanotubes (CNTs) or 200 nm carbon nanofibers (CNFs) (Figure 13b), and titanium dioxide (TiO_2) spheres with a diameter of 500 nm (Figure 13c). These nanocomposites could be used in the areas of surface-enhanced Raman scattering (SERS), electrochemical catalysis, and photovoltaic application, respectively. Moreover, the conjugates also formed the AuNP monolayer onto the surfaces of 3-D microstructures such as microchannels and microwells (Figure 13d) and 3-D macro glass crystals (Figure 13e) which became optically transparent in different colors of light pink, red, and blue as the crystals were coated with AuNPs in different diameters of 10, 20, and 30 nm, respectively. In addition, coated αS-AuNP single layer was stable in various conditions usally employed during device prepartion for real applications, including heat treatment or organic solvent treatment. (Figure 14) These results suggest that the omni-adsorption property of αS-AuNPs brings technological advantage on preparing functional graffiti of NPs on any surfaces of 2-D and 3-D objects.

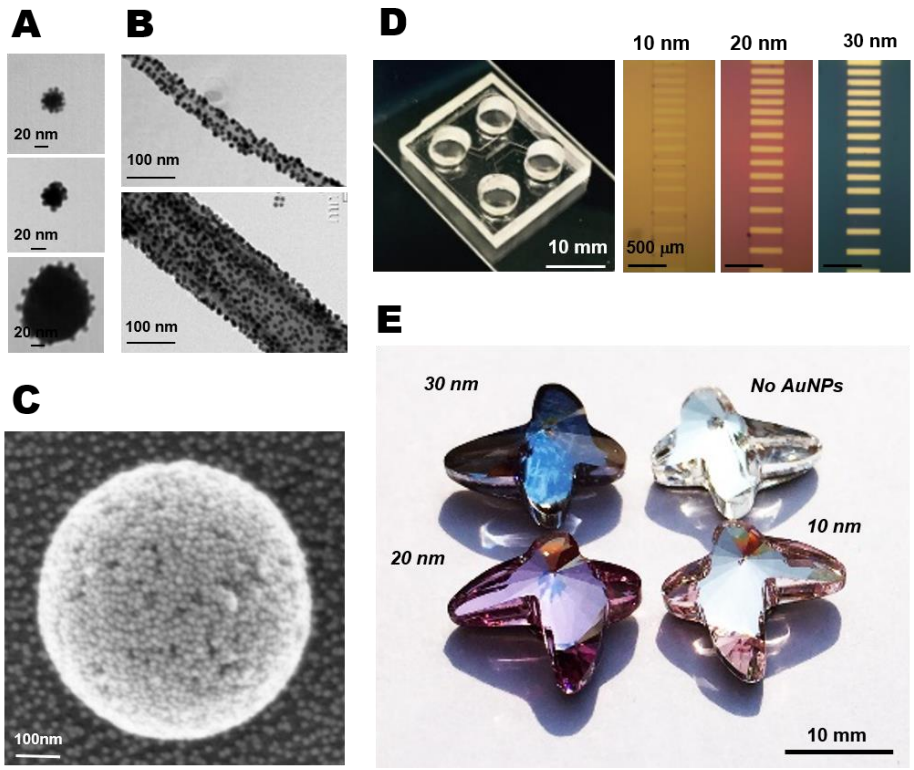

Figure 13. AuNP single-layer coats over diverse 3D substrates. (a) TEM images showing the AuNP-AuNP core-satellite structures with diameters of 30 nm-5 nm (top), 30 nm-10 nm (middle), and 100 nm-10 nm (bottom). (b) TEM images of the CNT (top) and CNF (bottom) coated with αS-AuNPs in a single-layer at high density. (c) SEM image showing the close-packed αS-AuNP single-layer coat on TiO_2 sphere. (d) Macroscopic image of PDMS micro-fluidic device (top) and optical microscope images of the micro-channels coated with αS-AuNPs in different size AuNPs of 10 nm (bottom left), 20 nm (bottom middle), or 30 nm (bottom right) showing light pink, red, and blue color, respectively. (e) Optical images of the glass crystals coated with αS-AuNPs in different sizes of 10, 20, and 30 nm, which reveal different colors of light pink, red, or blue, respectively.

I-4. Conclusions

We have introduced a simple but effective procedure to adhere AuNPs onto virtually all types of material surfaces in a close-packed single-layer by utilizing the unique omni-adhesive property of αS. Our solution-based approach allowed the particles to be imprinted onto the surfaces of either chemically diverse 2-D substrates or physically complicated 3-D objects in high resolution. It would be the structural plasticity of αS and its specific molecular orientation on the particle that are responsible for exhibiting the pluripotent adsorption property. Future trials of preparing the αS conjugates with various NPs and their adsorption onto a diverse set of substrates would open up a plethora of applications in the area of nanotechnology, which require NPs exerting their sustained activities in the surface-immobilized state.

Part II. Multiple Uses of Hybrid Gold Nanoparticles with α-Synuclein Protein

II-1. Introduction

(1) Practical applications of NP-based high-performance devices

As mentioned above, organization of nanoparticles (NPs) onto target substrates is a crucial step in their practical applications to develop NP-based high-performance devices. In the previous chapter, we have demonstrated the hybrid αS-AuNP coat on the diverse material's surface regardless of substrate compostion and shape. For its practical evaluation, the αS-AuNP conjugates have been layered on top of a few selected target substrates such as poly(methyl methacrylate) (PMMA), carbon nanotubes (CNTs), titanium dioxide (TiO_2) microsphere, polydimethylsiloxane (PDMS)/glass, graphene oxide (GO) to assess their effects on the performance of organic memory transistor, the oxygen reduction reaction (ORR) for fuel cell, the plasmonic enhancement in solar cell, the cell attachment and photoactivation, and photothermal cancertherapy, respectively.

(2) Role of αS layer

The irreplaceable crucial functions of the αS protein layer in those

applications would be demonstrated, which include the dielectric layer for memory charge retention, the sacrificial coat to expose AuNPs for ORR activity, the reaction center for additional chemical functionalization of silicification, and the bio-interface for cell localization, respectively. In this respect, α-synuclein would play dual-roles which are adhesive property and the mentioned irreplaceable function in each applications. Therefore, our solution-based strategy could be generalized as key element for the development of future nano-devices if various nanoparticles can be employed in complexation with αS.

(3) Nanoparticle based organic field-effect transistors

Organic field-effect transistors (OFETs), which can memorize electrical signal, have been developed as an emerging technology for various future applications. Due to the the charge trapping/detrapping dynamics, the characteristic hysteresis observed in a dual-sweep measurement of their transfer characteristics, i.e., gate voltage (V_G) versus drain current (I_D). Metal NP-based OFET memories have been developed to achieve both scaling-down requirements and multiple functionalities of optical, electrical, and biological properties in a single device. Previous reports have demonstrated a controllable threshold voltage (V_T) of organic nano-floating-gate memory by fabricating Au or AgNPs. The typical NP-based OFET memories were fabricated by two steps of generating NPs using heat-treatment to thermally evaporated thin metal sheets and sandwiching them with tunneling and

blocking gate insulators. This type of devices exhibited the capability of programmable/erasable charge storage inside the NPs with retention time exceeding ~10^4 s. As another fabrication method, NP-based OFET memories fabricated with attachement of solution-dispersed AuNPs to amine-terminated a SiO_2 gate dielectric were suggested. However, it is still desired to simplicate device fabrication methods and improve the device performance. For instance, metallic NPs from a thin metallic film are formed via aggregation, thus it is hard to control their sizes and distribution. Solution-based NP deposition shows limiations in terms of achieving high NP packing density and uniform distribution of NPs. The requirements for specific chemical treatment of NPs and/or substrate also complicate the device fabrication steps. In this respect, the development of a new-type of fabrication method for NP-based OFETs with simplified procedure and high performance is on demand. In this study, we demonstrate a new type of OFET fabrication method based on the adhesion of αS-AuNPs in which aS playes dual roles of adhesive and dielectric layer [32].

(4) Nanoparticle based fuel-cell performance enhancement

To improve the economical feasibility and practicality of fuel cells, the development of catalytic system based on non-platinum noble metals including Au clusters is suggested to overcome the inefficiency of the oxidation reduction reaction (ORR). As the most realistic method, the system of AuNPs located onto the electroconductive carbon supports including CNT

and graphene via either in situ synthesis or adsorption of the particles prepared ex situ has been developed [33,34]. However, previous studies were suffered from either disability in tunability particle's size and shape or inevitable presence of the the capping agents on the surface of NPs.

As a possible solution for the ORR catalyst, we demonstrate the αS-mediated AuNP immobilization onto CNTs. In addition to electrocatalytic property of the system, the resulting nanocomposites would expand their applicabilty to various areas including catalysis, nanoelectronics, optics, and chemical/biological sensors [33]. We applied O_2-plasma to the nanocomposites to uncoat particle-surrounding αS, which allowed exposure of surface of AuNPs for electrocatlytic activity. Our novel αS-mediated approach would have several advantages over previous systems: (i) high-density single-layered coating of AuNPs onto CNT without aggreagion of AuNPs, (ii) facile removal of the outer αS layer with O_2-plasma treatment exposing the reaction centers for ORR, and (iii) regulation over the size and number density of immobilized AuNPs to fabricate the optimized system for ORR.

(5) Particle-on-a-particle system and dye-sensitized solar cell

Prepartion of nanocomposites in particles-on-a-particle (PoP) system has been developed to maximize functionality of individual particles and induce new functionality from the resulting composite structure. In particular, the

nanocomposites in a shape of particles-on-a-particle (PoP) would create synergetic functionality generated from individual particle's physical and chemical properties. Contrary to previous strategies for the synthesis of PoP system, the αS-utilized NP adsorption strategy has allowed us to prepare the nanocomposite in a simple single step. We have fabricated αS-AuNP satellites on TiO_2 microspheres and tested the resulting PoP nanocomposites for their effects on enhancing the performance of dye-sensitized solar cells (DSSCs).

DSSCs are photovoltaic devices, which can convert solar energy to electricity. The molecular dye sensitizers absorb photon and generate excited electrons that transfer to FTO electrode for electricity [35]. Hence, the light absorption efficieny of dye moleules is a critical factor to determine the energy conversion efficiency of DSSCs. Our PoP system of S-AuNP satellites on TiO_2 microspheres has therefore been employed to take advantage of its synergentic effects for the improvement of the light harvesting efficiency: i) the core TiO_2 microspheres elongate the path length of incoming light by light scattering [36], and ii) the satellite AuNPs improve the light sensitization of dyes by amplifying the electromagnetic field near the particles with LSPR of AuNPs [36]. In this system, the αS layer serve as the reaction center for biosilicification [37] which is required to protect the underlying AuNPs from being dissolved in the oxidative solution of iodide/triiodide (I^-/I_3^-) electrolytes.

(6) Cell attachment and photothermal cancer therapy

For the development cell-targeted biotechnology, cell culture on a chemically and physically diverse set of surfaces has been on-demand. Diverse adhesive property of αS-AuNP complex has made cell-incompatible surfaces to cell-culturalbe surface. Furthermore, photothermal property of αS-AuNP also enables cell-detatchment control, which would lead to functional cell-to-machine interface or photo-activated cell control system. In this respect, we have developted photothermal therapy via the complex of αS-AuNPs adsorbed onto GO surfaces (αS-AuNP/GO). Photothermal therapy is one of minimally invasive and spatiotemporally controllable strategies for cancer treatment. For the photothermal therapy, Near-infrared (NIR) light is generally used due to its tissue penetrating property. Our αS-AuNP/GO complex system would be demonstrated as an effective material for photothermal therapy because of its unusual optical property and biological characteristics. Adjacent AuNPs in the complex induce strong SPR coupling, which leads to broadening and shifting of abosorbance spectra into NIR window. At the same time, cell-attachable property of αS-AuNPs enabled the complex to integrate with mesenchymal stem cells (MSCs), which are known as tumor-tropic cells. Tumor-tropic cell-mediated NP delivery has been demonstrated as an effective system to increase the tumor-targeting efficiency of anti-cancer nanostructures. In previous studies, the strategy to incorporate NPs within tumor-tropic cells was the cellular upkate of NPs by endocytosis. However, the method was suffered from the cell cytotoxicity of the intracellular NPs and leakage of NPs via exocytosis. In this respect, αS-AuNP/GO complex system would circumvent the issues because the way that

nanocmplex incorporate with tumor-tropic cells is not cellular uptake but the attatchment of the nanocomplex on the cell membrane.

II-2. Experimental Section

(1) Fabrication and characterization of memory devices

For the fabrication of non-flexible non-volatile memory development, heavily-doped *p*-type silicon (p^+-Si) wafers with thermally grown 200-nm SiO_2 was used as a gate electrode with blocking layer. The substrate was ultrasonically cleaned by subsequently placing them in a batch of deionized water, acetone, and isopropanol (5-min sonication for each) and O_2 plasma treatment (60 W, 45 sccm, 10 min). For αS-AuNP monolayer formation, a pellet of αS-AuNPs was re-suspended with 400 μl of 50 mM citrate at pH 4.5. And then a 200-μl droplet of the conjugate solution was plac ed onto the substrates (1.5 cm x 1.5 cm^2). The particle adsorption was carried out through incubation in a humid chamber at 40°C for 3 h. I n the case of preparing a low-density monolayer with 30-nm AuNPs, the adsorbing conjugate solution was diluted by 8 fold with 50 mM c itrate at pH 4.5. The resulting αS-AuNP monolayer on SiO_2/p^+-Si waf ers was washed two times with 20% MeOH at 4°C, and then purged with N_2 flow. For flexible non-volatile memory development, indium-tin-oxide (ITO) coated PET substrates were used as purchased from Sigma-Aldrich (ITO thickness: 130 nm, surface resistivity: 60 Ω/sq) for a shared

gate-electrode platform. These transparent plastic sheets were thoroughly cleaned by subsequent rinsing with acetone and isopropanol, followed by nitrogen blow-dry. A thin-film (~ 40 nm) of PEDOT:PSS (Clevios™, Heraeus) was deposited by spin-coating at 3,000 rpm for 60 s, with an immediate annealing step at 100°C for 10 min, for mainly serving as a morphological stabilizer for ITO. PMMA (Sigma-Aldrich, M.W. = 120k) solution was prepared at the concentration of 80 mg/ml in toluene and heated at 70°C with a magnetic stirrer. The uniformly mixed PMMA solution was spin-coated at 1,000 rpm for 45 s, and annealed at 120°C for 1 hr, creating a 850-nm thick gate-dielectric layer. αS-AuNPs suspended with 50 mM citrate at pH 4.5 were adsorbed onto the PMMA-coated substrate in a humid chamber at 40°C for 3 hr. After the adsorption, the substrate was washed thoroughly with DW at 4°C.

For both types of non-volatile memory fabrication, pentacene (Sigma-Aldrich, triple-sublimed grade, ≥99.995%) was deposited onto the αS-AuNP layer, which was adsorbed onto SiO_2/p^+-Si wafer or PMMA/ PEDOT:PSS/ITO/PET, by thermal evaporation in a vacuum chamber using a shadow mask for the patterned semiconducting channels. The pentacene deposition was conducted at a stable rate of 0.025 nm/s under the base pressure of 2×10^{-6} Torr. To finalize the device fabrication, 50 nm of Au source/drain electrodes were vacuum-evaporated in a dedicated chamber, defining the channel width of 500 μm and the channel length of 50 μm (base pressure: 4×10^{-6} Torr, deposition rate: 0.02-0.03 nm/s). The electrical characteristics of the flexible field-effect-transistors (FETs) were measured by using a parameter analyzer (4200-SCS Parameter Analyzer, Keithley,

Cleveland, OH) in the dark and under ambient atmosphere.

(2) Oxygen reduction reaction (ORR) performance test

For CNT-αS-AuNP preparation, 1.2 mg of multi-walled carbon nanotubes (MWCNT, Sigm-Aldrich) were reacted with αS-AuNPs under bath-sonication in 2 ml of 10 mM citrate, pH 4.5. αS-AuNPs were slowly added dropwise to the reaction solution of MWCNTs. The CNT-αS-AuNP composites were prepared with various sizes of AuNPs (CNT-$AuNP_{5nm(16.3\%)}$, CNT-$AuNP_{10nm(16.3\%)}$, and CNT-$AuNP_{20nm(16.3\%)}$) at different proportions (CNT-$AuNP_{5nm(8.8\%)}$, CNT-$AuNP_{5nm(16.3\%)}$, and CNT-$AuNP_{5nm(31.7\%)}$). The weight percent of AuNPs was obtained by monitoring the absorption intensity of αS-AuNPs at the maximum absorption wavelength of 518 nm. The resulting CNT-αS-AuNP complexes were washed with three consecutive centrifugations at 16,100 x g for 15 min while resuspending the precipitates with fresh DW. The final composites were lyophilized with a freeze-dryer (FDU-2200, Eyela, Japan). The outer αS layer of the complexes was removed by O_2-plasma treatment (100 W, 10 sccm, 20 min). Electrochemical measurements were conducted in a standard three electrode cell with Pt-wire counter electrode and saturated Ag/AgCl reference electrode using Autolab potentiostat (PGSTAT). All the potentials were obtained relative to the reversible hydrogen electrode (RHE), which was calibrated by the hydrogen oxidation reaction. The Au/CNT samples were mixed with Nafion resin

(Nafion® perfluorinated resin solution, 5 wt % in the mixture of lower aliphatic alcohols and water. contains 45% water, Sigma-Aldrich, 15 wt %) for a binder and dissolved in IPA. Before ORR measurement, the pre-scan was carried out between 0.05-1.0 V vs. RHE to clean the electrode surface. The ORR activity was measured in 0.1 M KOH solution saturated with O_2 at 298 K with a scan rate of 10 mVs^{-1} using a rotating ring disk electrode (Pine instrument). The rotating speed was maintained at 1,600 rpm. The capacitance term was calibrated by measuring CV under Ar saturated condition. The electron transfer number was calculated based on the ratio between ring current and disk current. Ring electrode (Pt) potential was held at a potential of 1.5 V vs. RHE during the measurement.

(3) Plasmon-enhanced dye-sensitized solar cell

The αS-AuNPs prepared through the reaction between 50 μl αS (1 mg/ml) and 400 μl of the AuNP colloidal solution were adsorbed onto 10 μg of TiO_2 spheres (EPR-Ti-0.7, EPRUI Nanoparticles & Microspheres Co. Ltd) in 50 mM citrate (pH 4.5) at 40°C for 3 h. The resulting αS-AuNP-TiO_2 complexes were collected after three subsequent centrifugations at 100 x g for 10 min after resuspending the precipitates with DW. The solvent was then completely changed to ethanol by carrying out the same centrifugation (100 x g, 10 min) three times. For the SiO_2 outer-shell formation surrounding the composites, the αS-AuNP-TiO_2 complex was mixed with 300 μl ammonium hydroxide, 125 μl DW, and 4,985 μl ethanol. TEOS (250 μl at 1 v/v % in IPA, Acros

Organics, Belgium) was added dropwise to the mixture with continuous stirring at 600 rpm. After 18 hr of incubation, the resulting complexes were washed by centrifugation with fresh ethanol (3,000 x g, 3 min) three times. The final products of SiO_2-coated αS-AuNP-TiO_2 complex were collected and dried in a rotary evaporator. The complexes were then mixed with a paste consisted of ethyl cellulose, lauric acid, and terpineol. Before the deposition of αS-AuNP-TiO_2 complex, FTO glass was pre-treated with $TiCl_4$ in 60^oC for 1 hr and heated at 500^oC for 30 min. The paste containing αS-AuNP-TiO_2 complex was screen-printed to an active area of 0.25 cm^2 on the FTO glass. The sample was dried at room temperature and annealed at 500^oC for 30 min. The N719 (Solaronix, Auboone, Switzerland) was loaded by immersing the modified FTP glass into 0.5 mM N719/ethanol solution for 18 hr and the free dyes were washed off with absolute ethanol several times. The dye-sensitized electrode was integrated with a platinum-coated counter electrode using 60 μm thick Surlyn film (DuPont, Wilmington, DE). The assembled electric cell was sealed and filled with the liquid electrode of 0.6 M 1, 2-dimethyl-3-propylimidazolium iodide, 0.1 M LiI, 0.05 M I_2, and 0.5 M 4-tert-butylpyridine in acetonitrile. The J-V curve of the cell was measured using a 500 W xenon lamp (SXIL model 05A50KS source unit). IPCE (K3100, McScience, Korea) spectra were obtained in the wavelength range between 350 and 800 nm under short-circuit condition.

(4) Cell culture

Cell adhesion experiments on the fluorinated wafer were performed with four different types of mammalian cells: primary human umbilical vein endothelial cells (HUVECs; Lonza, Basel, Switzerland), primary human lung fibroblasts (LFs; Lonza), human epithelial HeLa cells, and human dopaminergic neuroblastoma cells (SH-SY5Y). HUVECs, LFs, HeLa, and SH-SY5Y were grown in the endothelial growth medium (EGM-2; Lonza), fibroblast growth medium (FGM-2; Lonza), Dulbecco's modified Eagle's medium supplemented with 10% (v/v) fetal bovine serum, and DMEM supplemented with 10% fetal bovine serum, respectively, at 37^{o}C with 5% CO_2. On the fluorinated wafer with 0.5 cm x 0.5 cm in size, HUVECs, LFs, HeLa, and SH-SY5Y were seeded at 1 x 10^6, 1 x 10^6, 2 x 10^5, and 1.6 x 10^5 cells/ml. After incubation for 12 hr, cell fixation and immnuno-staining of the cells were carried out. For the cell culture in micro-fluidic devices, HUVECs at 1 x 10^6 cell/ml were loaded into the channels, and then cultured for 17 hr.

(5) Immunostaining and confocal laser scanning microscope (CLSM) examination

All the cultured cells were fixed with 4% paraformaldehyde after rinse with Dulbecco's phosphate-buffered saline (PBS). The fixed cells were permeabilized with 0.2% Triton X-100 for 15 min at room temperature, and treated with a blocking buffer (1% bovine serum albumin in PBS) for 30 min at 37^{o}C. Then, the cells were immunostained with filamentous actin (F-actin) probe, Alexa Fluor 488 phalloidin (Molecular Probes, Invitrogen, Carlsbad,

CA) for 20 min at room temperature. For the cells in micro-channel device, 4',6-diamidino-2-phenylindole (DAPI) staining was additionally conducted according to the manufacturer's instruction (Sigma-Aldrich). To visualize the αS-AuNP coat on micro-channel surfaces, the channels were stained with anti-αS antibody (LB509, Santa Cruz Biotechnology) and Alexafluoro 594-conjugated secondary antibody (Invitrogen). The fluorescence images were acquired with CLSM (LSM 710, Carl Zeiss, Germany).

(6) HeLa cell detachment by the photodynamic effect of αS-AuNP single-layer coat

HeLa cells were cultured in Dulbecco's modified Eagle's medium supplemented with 10% (v/v) fetal bovine serum at 37^{o}C with 5% CO_2. The HeLa cells were seeded at 2 x 10^5 cells/ml on the slide glass with 0.5 cm x 2 cm in size. After incubation for 24 hr, the cells adhered on the glass in the media and Alexa Fluor 488 phalloidin-stained cells were observed with optical microscope and CLSM, respectively. The slide glass was washed with PBS, and then the light at a wavelength of 530 nm illuminated the HeLa cells on the glass in PBS with a luminescence spectrometer (LS-55, Perkin-Elmer) for 30 sec. Both regions of the glass with or without the light irradiation were examined with optical microscope and CLSM.

(7) Synthesis of AuNPs and GO

Sodium citrate tribasic dihydrate (≥ 99 %), gold (III) chloride trihydrate ($HAuCl_4 \cdot 3H_2O$, ≥ 99.9 %) and graphite (< 20 μm) were purchased from Sigma Aldrich and used without further purification. First, the citrate-capped AuNPs were synthesized according to the method developed by Bastus et al. [38]. Seed AuNPs were prepared by boiling 150 mL of 2.2 mM sodium citrate under a condenser. Soon after, 1 mL of 25 mM $HAuCl_4$ was added into the boiling solution with continuous stirring. After 10 min, the seed solution was cooled down to 90 ℃. To obtain larger AuNPs, 1 mL of 25 mM $HAuCl_4$ was injected into the seed solution. The reaction was terminated after 30 min. This process was repeated twice. The sample was then diluted by adding 53 mL of deionized water and 2 mL of 60 mM sodium citrate to 55 mL of the sample. This solution was then used as a seed solution, and the process was repeated. The AuNP size was controlled by the number of repeats. Next, GO flakes were synthesized using Hummers' method [39]. The prepared GO was suspended in water (0.05 wt %) and exfoliated using ultrasonication for 3 h. For purification, the solution was dialyzed for 6 h to remove residual acids and salts. Then, the obtained solution was centrifuged at 3000 rpm for 20 min to remove any unexfoliated GO.

(8) Preparation and Characterization of αS-AuNP/GO hybrid sheets

The αS-$AuNP_{30nm}$ was prepared by incubating the mixture of 70 μM αS solution and 0.2 mg/mL $AuNP_{30nm}$ colloidal solution at a volume ratio of 1 : 8 for 12 h at 4 ℃. The αS-$AuNP_{20nm}$ was synthesized by reacting a mixture

of 70 μM α-synuclein solution and 0.05 mg/mL $AuNP_{20nm}$ colloidal solution at a volume ratio of 1 : 6 for 12 h at 4 ℃. Unbound αS-molecules were subsequently removed by successive centrifugation and resuspension with fresh buffer solution. αS-coated $AuNP_{30nm}$ (0.15 mg) suspended in 50 mM citrate (pH 4.5) was reacted with 1.75 μg of GO for 2 h at 40 ℃. Short bath sonication was applied before the adsorption to fabricate the homogeneous complex. After the first adsorption, 0.03 mg of αS-$AuNP_{20nm}$ was added to the solution and another bath sonication was performed. The mixture was then incubated for 2 h at 40 ℃ and the unreacted AuNPs were removed by centrifugation followed by resuspension with distilled water (DW).

αS-AuNP/GO sheets were characterized by SEM, TEM, AFM, Raman spectroscopy, and UV-visible spectrophotometer. The αS-AuNP/GO sheets on the copper grid were examined with FE-SEM (SUPRA 55VP, Carl Zeiss, Germany) at 2.0 kV after coating the air-dried samples with a 2-nm-thick layer of platinum (BAL-TEC/SCD 005 sputter coater, Switzerland). The top-viewed TEM image was obtained by examining the αS-AuNP/GO sheets on a carbon-coated 200-mesh copper grid (Ted Pella Inc. CA) with TEM (JEM 1010, JEOL, Japan). The side-viewed TEM image was investigated after sectioning the αS-AuNP/GO sheets embedded in Spurr's resin. The surface morphology and height profile of the sample on poly-L-Lysine treated mica surface was examined using an Innova AFM (Veeco, Plainview, USA). Raman spectra of GO and αS-AuNP/GO sheet on glass surface were measured with Raman spectroscopy (LabRam 300, HORIBA Jobin Yvon, USA). Absorption spectra were obtained by measuring the optical density of

a 10-fold diluted solution of the samples using the wavescan mode of UV-visible spectrophotometer (Ultrospec 2100 pro, Amersham Biosciences, Uppsala, Sweden).

II-3. Results and Discussion

(1) Efficient Charge Trapping of the αS-AuNP Single-Layer in Memory Transistors

(1)-1. Non-flexible substrate based memory development

For the development of non-volatile memory, αS-AuNP was adsorbed onto SiO_2 surface as monolayer at pH 4.5 for the charge trap (Scheme 3a). Subsequently, pentacene, a high-performance organic semiconductor, and Au source/drain contacts were deposited in order onto the αS-AuNP layer to complete OFET device fabrication (Scheme 3b).

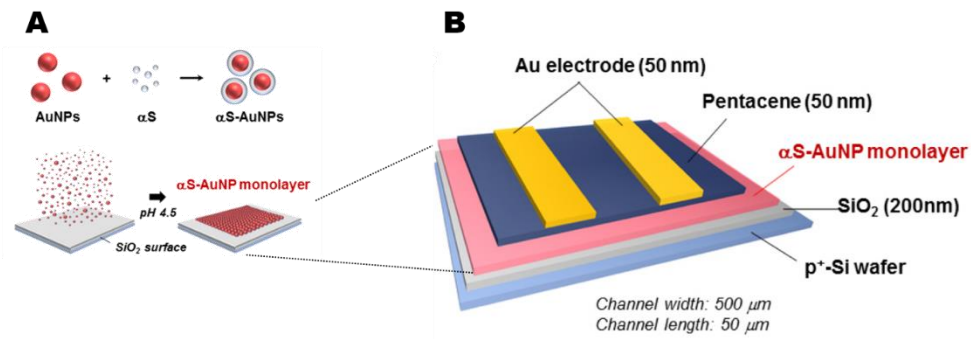

Scheme 3. Schematic representation of fabrication of memory transistor. (a) A schematic representation of the αS-Au NP monolayer formation on a SiO_2 surface. (b) Structure of the OFET devices.

We have analyzed the packing densities of the αS-AuNPs with FE-SEM (Figure 14a). The average densities of αS-AuNPs with diameters of 5, 10, and 30 nm were 2518.3±153.3, 1365±50.3, and 554±21.7 μm^{-2}, respectively. The packing density of αS-AuNP monolayer was controlled by adjusting the concentration of αS-AuNP solution. In the case of 30 nm AuNPs, the packing density decreased to 104.7±13.8 μm^{-2} when the solution concentration was diluted eight-folds. To confirm the presence of αS-AuNP monolayer, we have measured the height profile via AFM analysis (Figure 14b). The thickness measured over a few-μm length was uniform and comparable to the sizes of constituent particles.

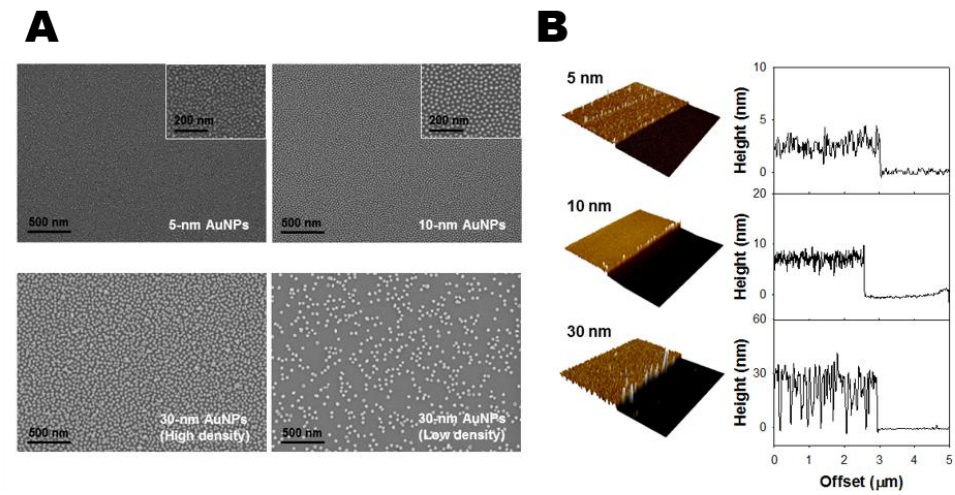

Figure 14. Adsorbed aS-AuNPs single layer on SiO_2 gate. (a) FE-SEM images of αS-Au NP monolayers made of 5-nm, 10-nm and 30-nm NPs. Magnified images are provided in insets. (b) Three-dimensional AFM images and thickness profiles of αS-Au NP monolayers made of 5-nm (top), 10-nm (middle), and 30-nm (bottom) NPs.

The electrical property of the fabricated device was investigated by measuring the transfer characteristics. A sweep-direction dependent behavior of I_D was observed in all cases (Figure 15a). The small hysteresis was observed in the OFETs without AuNPs due to the electron-trapping hydroxyl groups on the SiO_2 and/or oxygen-induced traps in the pentacene layer. On the contrary, the devices with αS-AuNP revealed the enlarged hysteresis in both transfer and output characteristics. The result attributes to the additional charge trapping in αS-AuNPs during the sweeping measurements. The AuNP coated with the dielectric layer of αS would be demonstrated as the charge-trapping center. It is worth mentioning that maximum channel current decreased with the increase of AuNP size. AFM analysis revealed that size increase of AuNP induced smaller polycrystalline grains of pentacene layer (Figure 15b). The smaller polycrystalline grains of pentacene layer led to decrease in hole mobility. It is northworthy that most of the measured devices within each 1.5 $\times$ 1.5 cm^2 substrate showed an impressively narrow statistical distribution of the device parameters (Figure 15c). Compared to previous reports, a distinctive advantage of our technique is the uniform packing of the NPs over large-area substrates and, thereby, very low fluctuation in on-chip device performance.

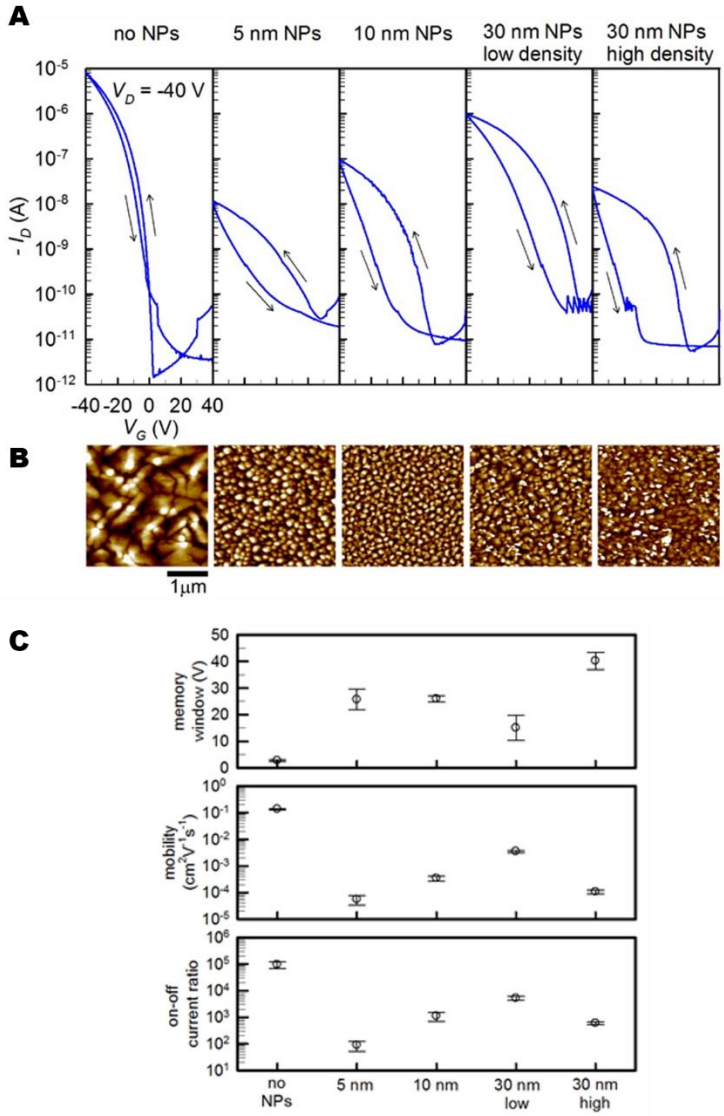

Figure 15. Transfer characteristics of αS-AuNPs based OFETs. (a) Dual-sweep transfer curves measured in the saturation regime with different αS-Au NP structures. (b) Corresponding AFM image of the 50-nm thick pentacene channel of each OFET. (c) Statistically estimated device parameters from seven different transistors.

The memory window, the gap between two V_G values at I_D of 10 nA, is found to be quasi-linearly dependent on the V_G sweep range (Figure 16a). The result indicates that injection and removal of charges in the core NP are effectively manipulated by V_G. Also, the slope parameter of the quasi-linearly dependency increased with with the NP size and density (Figure 16a).

The gate controllabitily was evaluated via separating the programming and reading functions of V_G. Three different states of the initial, programmed, and erased states using the same OFET were fixed with a V_G pulse of ±20 V for 10s. The transfer characteristics measured at each state confirmed definite transition of the state from "off-state" to "on-state" and return from "on-state" to "off-state" based on a V_G pulse (Figure 17a). We exteneded the measurements by alternating V_G pulses from ±10 V to ±60 V (Figure 17b). It was able to confirm the successful control over the electrical state by V_G in the OFETs by analyzing the threshold voltage shift (ΔV_T). The result also provides an indication of actuation principes of the OFETs. When the first negative V_G pulse is applied, holes are trapped and accumulated within AuNPs across the tunneling barrier of the thin protein encapsulation (Figure 17c). After the removal of the first pulse, the protein layer played a role of the dielectric layer to retain the charges in AuNPs. Under the positive V_G pulse, the trapped charges in AuNPs were partly moved into the pentacene layer. The partial return indicates that the efficiency of this discharging step is lower than that of the charging operation. Due to difference of efficiency between discharging and charging operations, the negative shift of V_T was observed as the measurement proceeds.

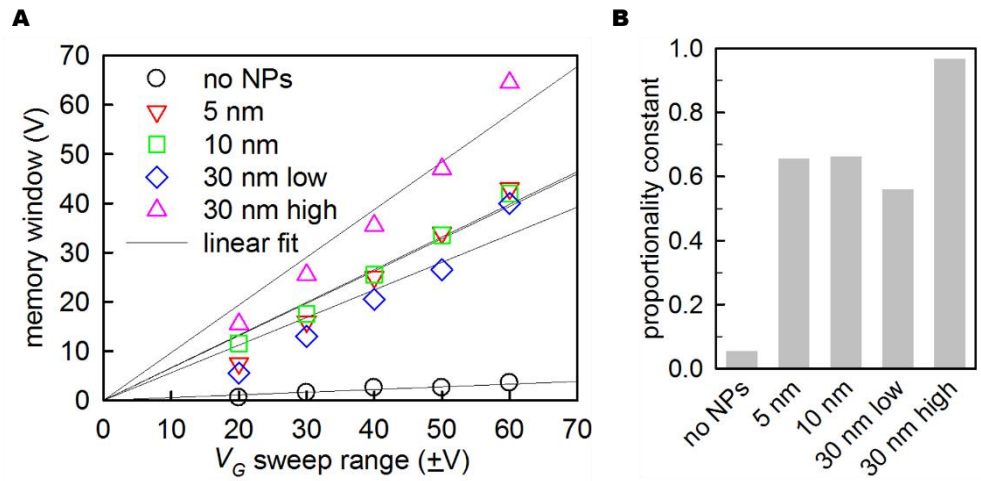

Figure 16. Summarized results of transfer characteristics of OFETs. (a) Symbols: gate-sweep range dependent memory windows. Lines: linear regressions through the origin. (b) Proportionality between the sweep voltage range and the observed hysteresis.

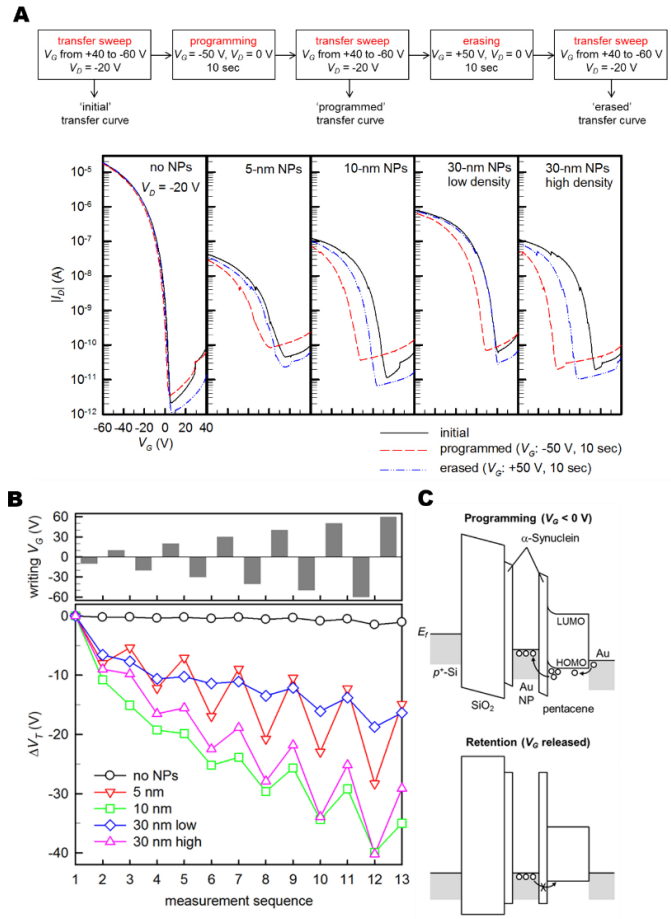

Figure 17. Programming and erasing tests of OFETs. (a) Upper panel summarizes the measurement protocol that was used to obtain 'initial', 'programmed', and 'erased' states of the given device. Lower panel shows the transfer curves recorded as such. (b) Upper panel indicates the polarity and magnitude of the gate programming/erasing pulse applied between transfer measurements. Lower panel corresponds to ΔV_T observed upon repeated measurements of the transfer characteristics at V_D = -20 V. (c) Schematic explanation of the gate-bias programming and charge retention. Ef denotes the Fermi level of the electrodes and NPs. The flat-band potential is assumed to be zero for this diagram.

In the non-volatile development, it is important to estimate the charge retention time, which is directly linked to the data storage and possible applications. Charge leakage across the blocking layer is mainly caused by defects sites in a dielectric layer, tunneling, and thermionic emission. We estimated the charge rentention time by extrapolation. At first, a fast transfer sweep was conducted, and the initial current ($I_{initial}$) at V_G = 0 V, V_D = -20 V was recorded for each sample. Then, the devices were under the programming operation of V_G = -50 V, V_D = 0 V for 10 s, which produced a negative ΔV_T and decrease of the magnitude in I_D at V_G = 0 V. When V_G was released after the programming operation, I_D slowly recovered its initial value ($I_{initial}$) as charge leakage proceeded. Then, we measured this relaxation dynamics by periodically reading I_D with V_G = 0 V, V_D = -20 V. In the log-log plot of the time-dependent drain current I_D (t), we fit the linear region nearest to the end of the measurement to a power-law relationship

$$I_D(t) \propto t^{\gamma}$$

where t is the relaxation time and γ is the characteristic exponent that corresponds to the slope of the fit lines in Figure 18a-d. To decribe the physical mechanism of the system, we analyzed the results by i) looking into the trends in γ with the brief calculation of number of holes trapped within AuNPs, and ii) correlating estimated charge retention time with current modulation parameters (Figure 18e). The trends in γ indicated that the charge relaxation occurs more quickly under a lower density of AuNPs with a higher population of charges per particle due to the stronger repulsive electrostatic

interaction inside the AuNPs. Also, the estimated charge retention time has positive correlation with the current modulation parameter, defined as the ratio between I_{initial} and the first data point in I_D (t). In conclusion, by introducing charge-trappable AuNPs, we have developed protein-based memory system with controllable data retention times in the order of 10^3 to 10^7 s.

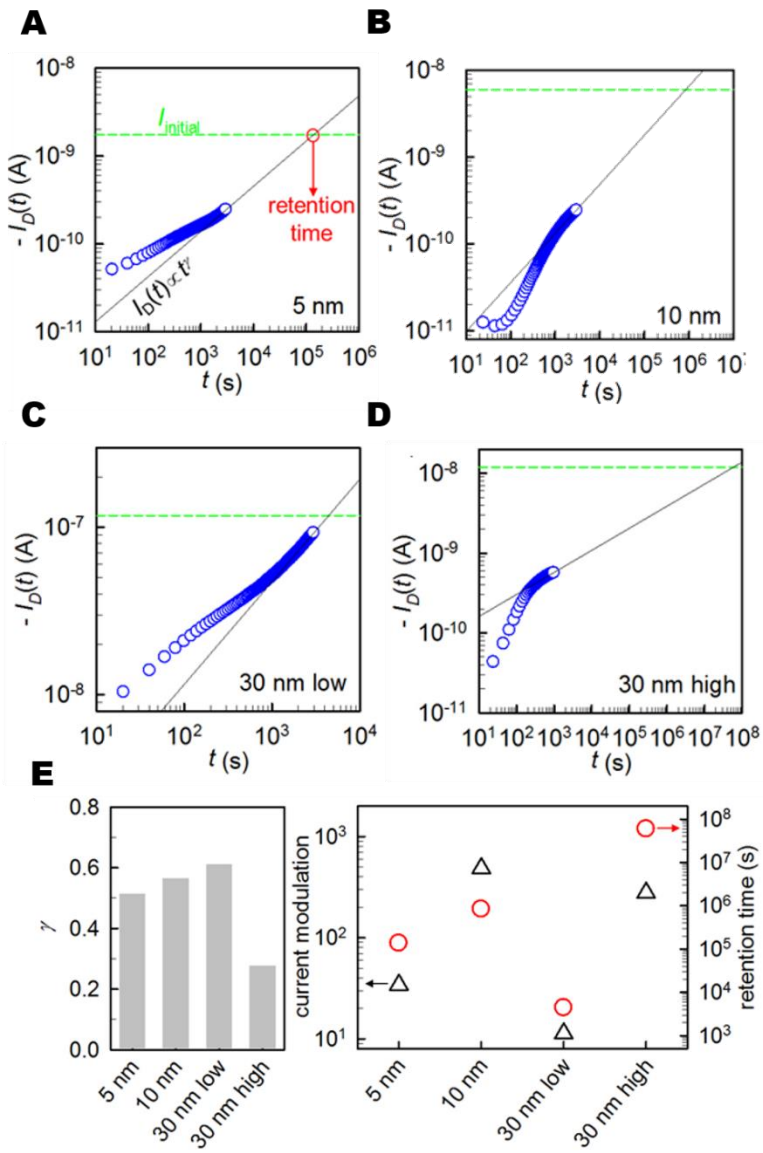

Figure 18. Retention characteristics of αS-AuNP based OFETs. (a)-(d) Transient relaxation measurements after charging the NPs by V_G = -50 V for 10 s with V_D maintained at zero. (e) Exponent γ of the fits and Gate-pulse-induced current modulation factors and retention time values.

(1)-2. Flexible substrate based memory development

Our solution-based low-temperature coating strategy is well suited for the AuNP immobilization onto plastic substrates to fabricate the NP-based flexible OFET memories. In this device construction, poly(3,4-ethylenedioxythiophene)-polystyrenesulfonate (PEDOT:PSS)-coated PET/indium tin oxide (ITO) substrate was used as a common gate electrode, and a spin-coated PMMA layer served as a gate insulator. Onto the PMMA layer, αS-AuNPs were adsorbed to form the single-layer as nano-floating gate on which then pentacene channel and gold source/drain electrodes were deposited. The final device produced exhibited the bending flexibility and high transparency (Figure 19a). SEM analysis revealed that the αS-AuNP conjugates comprising either 5 nm or 10 nm particles were tightly packed to form the single-layered coat on the PMMA substrate (Figure 19b). The transfer characteristics of the memory devices as represented with drain current (I_D) vs. gate voltage (V_G) were investigated by cyclic sweeping of V_G at a fixed drain voltage (V_D) of - 60 V (Figure 19c). In contrast to the device without αS-AuNP, the αS-AuNP-integrated devices manifested significant hysteretic behaviors. Considering the injection energetics from Au source into depleted pentacene [40,41], the hysteresis results from decrease in $|I_D|$ at the immediate reverse sweep due to the hole trapping inside AuNPs during the off-to-on scan. Figure 19d shows that the memory window (the difference in forward and reverse sweep V_G producing the I_D of -1 nA) strongly depends on the size of AuNPs as well as V_G sweep range. For both devices with αS-$AuNP_{5nm}$ and αS-$AuNP_{10nm}$, as the V_G sweep range increased with higher

potential swings, the memory window became widen owing to the increased number of trapped holes. Likewise, the memory window also further improved as the size of AuNPs increased. The 10-nm AuNPs showed the higher memory window than the 5-nm AuNPs at each V_G sweep range. The observed NP's size effect is also in line with such an interpretation that as the larger portion of the channel area a metallic material occupied, the higher density of trapped carriers can be reached. Despite the high memory window, however, 20-nm AuNPs resulted in an insufficient yield of the channel current that is much lower than that of 10-nm AuNPs. It suggests that there is a trade-off between the memory window and the maximum channel current [42] since the pentacene organic molecules are only weakly crystallized on a rough surface of the αS-AuNP layer.

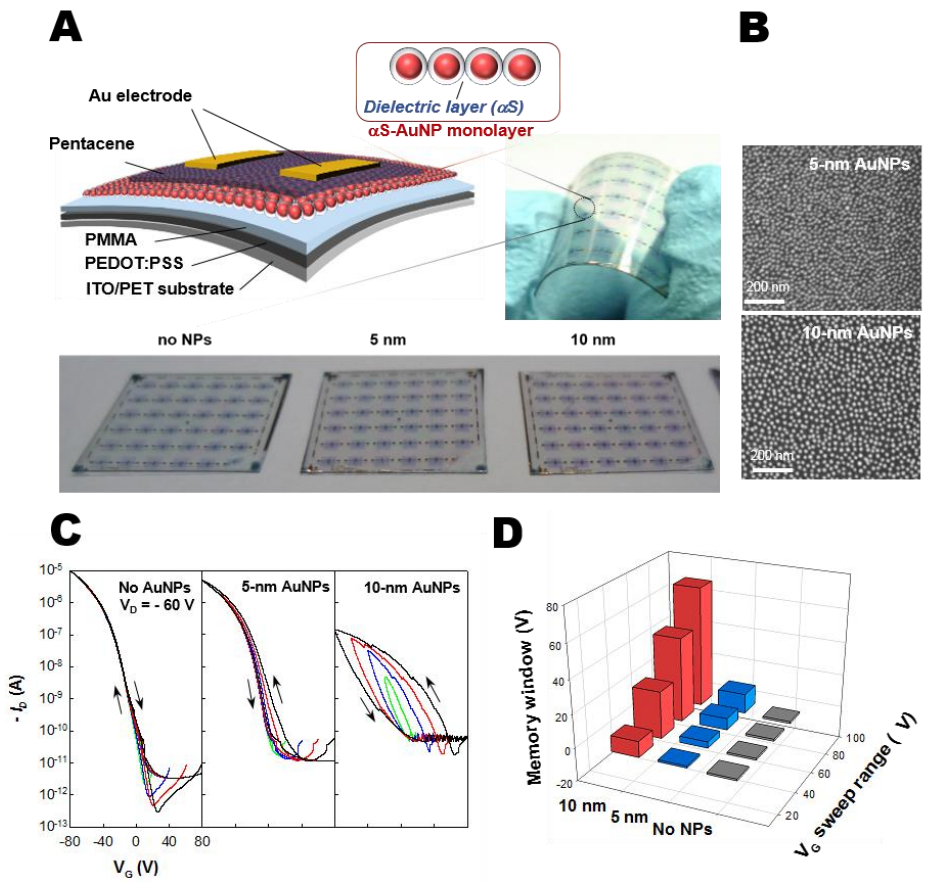

Figure 19. Flexible Flash memory development. (a) Schematic drawing for the structure of FET memory device comprising ITO/PET substrate, PEDOT:PSS, PMMA layer coated with αS-AuNPs, pentacene layer, and Au electrodes. Diagram representing αS dielectricity is shown in inset. Photograph of FET memory device with αS-AuNPs shows its bending flexibility. (b) SEM images of the tightly packed αS-AuNP single-layer with a particle diameter of 5 nm (left) and 10 nm (right) on PMMA layers of FET memory devices. (c) Transfer characteristics of FET memory without αS-AuNP (left) and with αS-AuNP5nm (middle) and αS-AuNP10nm (right).

The programming test, which provides information necessary for the practical use, was conducted, and the results showed stable two-state profile operation (Figure 20a). When addressing our memories with a periodically combined gate/drain pulse, both devices made of 5 nm AuNPs and 10 nm AuNPs showed reproducible data levels. Retention time evaluation was carried out by repeatedly measuring the off- and on- current after setting these states by a writing pulse (V_G = -80 V) and erasing pulse (V_G = +80 V), respectively (Figure 20b). The time-varying I_D levels were recorded at V_G = 0 V and V_D = -10 V, and the estimated retention time was approximately 10^4s for both devices. It is noteworthy that our memory devices were produced without introducing an additional tunneling layer on top of NPs. The αS protein shell itself played dual roles not only as a mediator for the AuNP monolayer adsorption but also as a thin dielectric layer. It is this protein's dielectric property that prevents the organic channel from being too conductive at the depletion-regime and renders the observed level of charge retention to the Au nanocapacitors. Therefore, the unique characteristics of αS exhibiting promiscuous adsorption with dielectric property have been demonstrated to be suitable for the successful construction of flexible non-volatile memory by producing close-packed single-layer coat of AuNPs over the organic substrate, which promises their contribution to the development of various types of nanoparticle-based electronics.

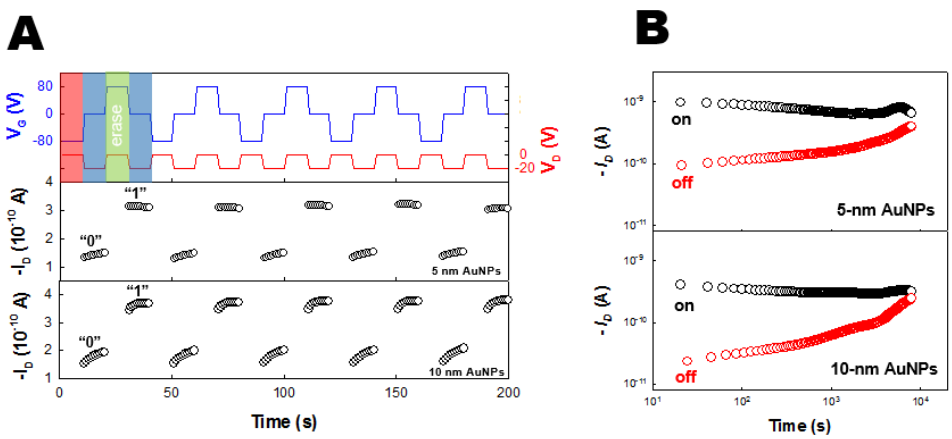

Figure 20. Programming and retention time test of αS-AuNP-based flexible OFET memory. (a) Programming demonstration by applying V_G/V_D pulse (top graph) at -80/0 V (write), 0/-20 V (read), +80/0 V (erase), and 0/-20 V(read). Both devices with αS-AuNP$_{5nm}$ (middle graph) and αS-AuNP$_{10nm}$ (bottom graph) show well-defined bi-stable operation with reproducible readouts. (b) Retention time evaluation by repeatedly measuring on- (black circle) and off- (red circle) current ($-I_D$) at V_G = 0 V. Both αS-AuNP$_{5nm}$ (top graph) and αS-AuNP$_{10nm}$ (bottom graph) devices show the retention time of approximately 10^4 s.

(2) Single-layered High Density Coating of αS-AuNPs on CNT for the Oxygen Reduction Reaction in Fuel Cells

The αS-AuNP-CNT complexes were produced through a sonicated incubation of CNTs with αS-AuNPs in 10 mM citrate, pH 4.5, and then subjected to O_2 plasma treatment to uncoat the αS from the particles (Figure 21a). TEM images of the nanocomposites showed the high-density single-layered AuNPs anchored onto the surface of CNTs (Figure 21b). By taking advantage of the solution-based immobilization process with the pre-made αS-AuNPs, various types of the nanocomposites were prepared by altering either the particle size (5, 10, and 20 nm) at a fixed concentration of 16.3 wt.% or the particle concentration (8.8, 16.3, and 31.7 wt.%) of 5-nm AuNPs. After the O_2 plasma treatment, all the nanocomposites were examined for their electrochemical property with cyclic voltammetry (CV) in argon (Ar) saturated alkaline solution (Figure 21c). Since all the CV curves showed the Au reduction peaks at 1.0 V_{RHE} [43], the AuNPs which remained anchored to the plasma-treated complexes were proven to be well exposed to the electrolyte solution. The NP size-dependent reduction current densities were obtained as -1.64, -0.64, and -0.25 mA cm^{-2} for 5-, 10-, and 20-nm AuNPs, respectively, and the NP concentration-dependent current densities were -0.48, -1.64, and -1.72 mA cm^{-2} at 8.8, 16.3, and 31.7 wt.% of the 5-nm AuNPs, respectively. The data also demonstrated that the exposed AuNPs were capable of exhibiting the active reduction reaction, which was enhanced as the surface area of Au active sites increased.

To evaluate electrocatalytic activity of the AuNP-CNT complexes for the ORR, linear-sweep voltammetry (LSV) was measured with a rotating disk electrode at 1600 rpm (Figure 22a). In the LSV results, both the ORR onset potentials (0.92, 0.91, and 0.82 V_{RHE}) and the corresponding ORR current densities (-5.30, -4.68, and -3.12 mA cm^{-2} at 0.1 V_{RHE}) decreased as the AuNP size of the complexes increased (5, 10, and 20 nm), respectively. The results showing the higher ORR activity obtained with the smaller AuNPs are consistent with the previous report suggesting the inverse relationship between the particle size and the electro-catalytic activity [44]. The decreased coordination of Au and the reduced electrophilicity of the smaller particles would lead to the strong electronic interaction between Au and oxygen (O), which eventually decreases the activation energy for ORR. In addition to the size dependence, the increased weight percentage of the immobilized AuNPs was also shown to enhance the ORR efficiency. As the concentration of 5-nm AuNP increased (8.8, 16.3, and 31.7 wt.%), the ORR current density was also augmented (-4.91, -5.30, and -6.02 $mAcm^{-2}$ at 0.1 V_{RHE}). Since the ring current was negligible in a rotating ring-disk electrode (RRDE) measurement (Figure 22b), the 2-electron reduction reaction of O_2 to H_2O_2 did not occur on the AuNP-CNT complex electrode. Moreover, the electron transfer number (n) calculated as approximately 3.8 over the potential range from 0.1 V_{RHE} to 0.9 V_{RHE} (Figure 22c) indicated that the ORR mainly progressed via 4-electron reduction of O_2 to H_2O on the AuNP-CNT electrode, which would be merited for the development of high-performance fuel cells.

Taken together, it has been demonstrated that the αS-mediated AuNP coating strategy was successfully used to produce the AuNP-CNT complexes capable of exerting the ORR activity, in which the protein of αS allowed not only the high-density single-layer coat formation of AuNPs onto CNT, but also its easy removal with the O_2 plasma treatment to expose reactive Au sites. Our approach, therefore, could be readily employed to fabricate various types of CNT-based hybrid materials with diverse NPs for future applications in the areas of nanoelectronics, catalysis, and sensor development

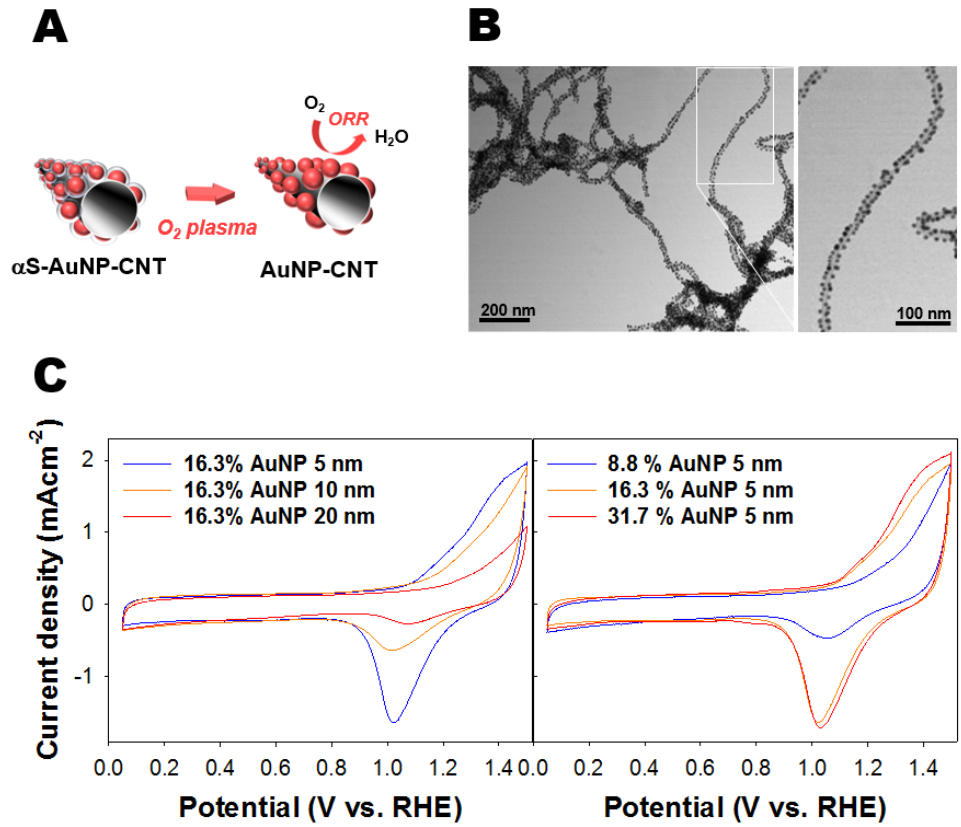

Figure 21. Adsorption of aS-AuNP single layer on CNT and O_2 plasma treatment. (a) Schematic illustration for the preparation of AuNP-CNT complex capable of ORR by removing outer αS layer with O_2 plasma treatment. (b) TEM images of the AuNP-CNT complexes. A magnified image of the complex is also provided. (c) CV curves of ORR for the plasma-treated αS-AuNP-CNT complexes containing either different proportions of AuNPs [left graph; $AuNP_{5nm(8.8\ Au\ wt\%)}$-CNT (blue line), $AuNP_{5nm(16.3wt\%)}$-CNT (orange), and $AuNP_{5nm(31.7Au\ wt\%)}$-CNT (red)] or different sizes of the particles [right graph; $AuNP_{5nm(16.3wt\%)}$-CNT (blue line), $AuNP_{10nm(16.3wt\%)}$-CNT (orange), and $AuNP_{20nm(16.3wt\%)}$-CNT (red)].

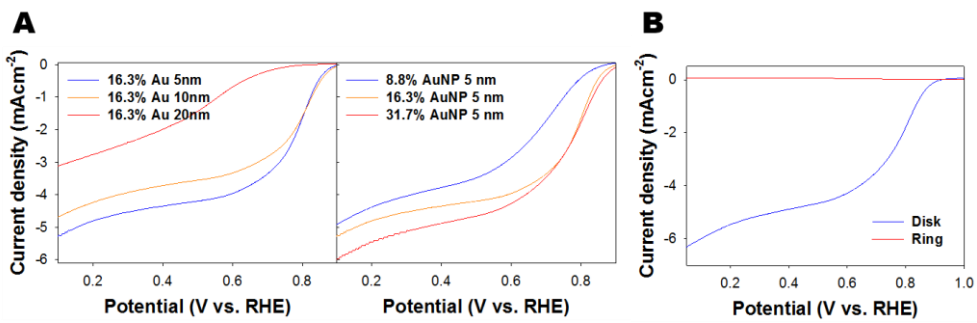

Figure 22. Electrocatalysis of O_2-plasma treated AuNP-CNT. (a) LSV curves of ORR for the plasma-treated αS-AuNP-CNT complexes containing either different proportions of AuNPs [left graph; $AuNP_{5nm(8.8\ Au\ wt\%)}$-CNT (blue line), $AuNP_{5nm(16.3wt\%)}$-CNT (orange), and $AuNP_{5nm(31.7Au\ wt\%)}$-CNT (red)] or different sizes of the particles [right graph; $AuNP_{5nm(16.3wt\%)}$-CNT (blue line), $AuNP_{10nm(16.3wt\%)}$-CNT (orange), and $AuNP_{20nm(16.3wt\%)}$-CNT (red)]. (b) RRDE curves of $AuNP5nm_{(31.7Au\ wt\%)}$-CNT revealing ring (red line) and disk (blue line) current. Electron transfer number n obtained from 0.1 to 0.9 V_{RHE} is shown in inset.

(3) Facile Fabrication of αS-AuNP Satellites on TiO_2 Microsphere and Their Use in the Dye-sensitized Solar Cells

Assembly of NPs into multi-dimensional structures has been considered valuable to not only maximize individual functions of constituting particles, but also create novel properties as a result of particle-particle interactions. In particular, preparation of nanocomposites in a shape of particles-on-a-particle (PoP) would be useful to prepare devices in nanotechnology since those structures could create synergetic functionality generated from each particle's physical and chemical properties. Simplicity of the αS-utilized NP adsorption strategy has allowed us to prepare the αS-AuNP satellites on TiO_2 microspheres in a single step. The resulting PoP nanocomposites were tested for their effects on enhancing the performance of dye-sensitized solar cells (DSSCs).

DSSCs are photovoltaic devices considered as a promising power conversion system to produce electricity from solar energy. Upon illumination, the molecular dye sensitizers generate electrons that subsequently transfer to a thin layer of TiO_2 NPs deposited on top of the fluoride-doped tin oxide (FTO) electrode for the generation of electricity [35]. Hence, the light absorption by the sensitizers is a critical factor to determine the energy conversion efficiency of DSSCs. Our PoP system decorating TiO_2 microsphere with satellite αS-AuNPs has therefore been employed to take advantage of its multifarious effects for the improvement of the light

harvesting efficiency. First of all, the core TiO_2 microspheres are able to elongate the path length of incoming light due to light scattering for the dyes to encounter the photons more frequently [36]. Secondly, the satellite AuNPs improve the light sensitization of dyes by exerting localized surface plasmon resonance (LSPR) and thus amplifying the electromagnetic field near the particles [36]. Finally, the outer shell proteins of αS serve as the reaction center for biosilicification [37] which is required to protect the underlying AuNPs from being dissolved in the etching solution of iodide/triiodide (I^-/I_3^-) electrolytes as well as their agglomeration during the high-temperature process of the DSSC fabrication. After depositing additional dyes on top of the outer silica shell, the resulting nanocomposites were assessed to show their enhancing effect on the light absorption of the dye-adsorbed TiO_2 NPs prepared from $TiCl_4$-treated-FTO electrode via screen printing followed by thermal annealing process.

The αS-AuNP-TiO_2 nanocomposites were prepared by incubating αS-AuNPs with well-dispersed TiO_2 microspheres in 50 mM citrate at pH 4.5. The nanocomposites showed the high-density single-layer coat of AuNPs onto 500-nm TiO_2 sphere, and the complexes appeared reddish in the optical image due to the surface plasmon of AuNPs. The αS proteins caused tetraethyl orthosilicate (TEOS) to exhibit serial condensation to form SiO_2, which produced the outer silica shell via the Si-O-Si linkage formation (Figure 23a). The protein-based biosilicification saved us from using additional chemical agents for the silica shell formation on the surface of bare metal NPs, which include 3-aminopropyl triethoxy silane (APTES),

glutaraldehyde, and PEGylated bis(sulfosuccinimidyl) suberate. TEM images revealed that the αS-AuNPs on TiO_2 microsphere were covered with an additional layer of SiO_2 shell with a thickness below 10 nm (Figure 23b) which was suggested to be optimal to utilize plasmonic property of AuNPs while preventing iodide/triiodide (I^-/I_3^-) ions from penetration. To verify its protective role, the SiO_2-coated nanocomposites were mixed with the etching solution of I^-/I_3^- electrolytes, in which the reddish color of the complexes was entirely preserved (Figure 23c). On the other hand, the nanocomposites without the SiO_2 coat lost the reddish color after the electrolyte treatment due to oxidation of the unprotected AuNPs by the I^-/I_3^- redox pair. Therefore, the SiO_2-coated αS-AuNP-TiO_2 composites were demonstrated to be suitable for their application in the plasmon-enhanced DSSCs as previously suggested with the SiO_2-protected metal NPs.

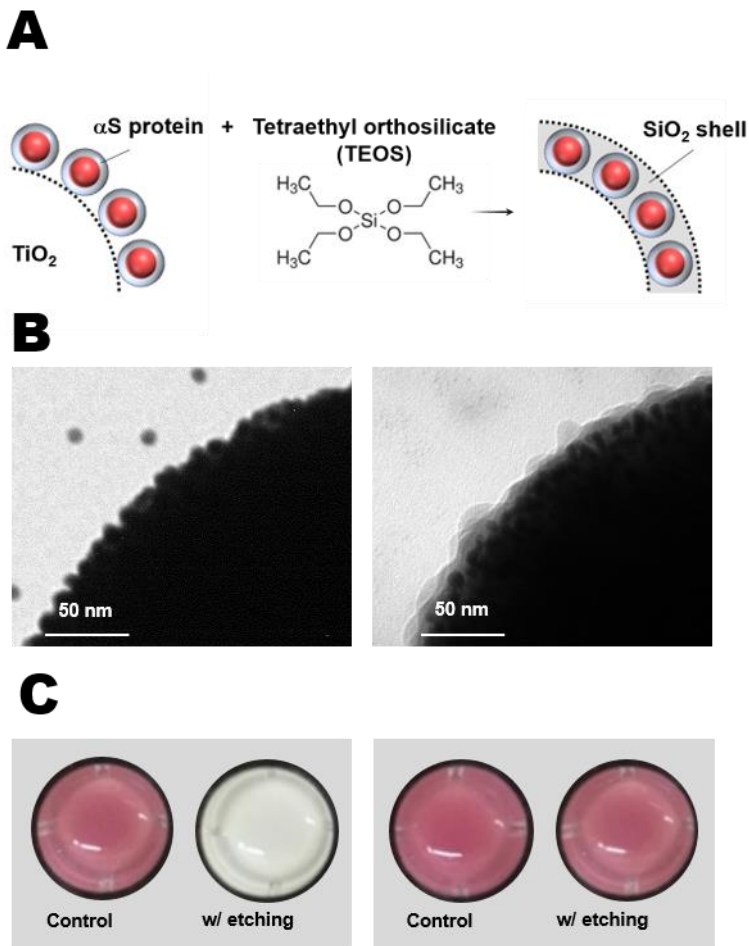

Figure 23. αS-AuNP single layer on TiO2 microsphere and biosilicification. (a) Schematic representation of a reaction of αS protein with tetraethyl orthosilicate (TEOS) to form outer SiO_2 shell. (b) TEM images of the complexes either unmodified (left) or TEOS-treated (right). (c) Stability test of the αS-AuNP-TiO_2 complex without (left box) and with the TEOS treatment (right box). Optical images in boxes show the AuNP-TiO_2 complex solution before (left) and after (right) the treatment of I^-/I_3^- electrolyte solution for 1 hr.

The DSSCs were fabricated with the SiO_2-coated αS-AuNP-TiO_2 PoPs located on top of the dye-adsorbed TiO_2 NPs in the I^-/I_3^- electrolytes between two FTO electrodes of photoanode and Pt counter electrode (Figure 24a). The photoanode was prepared by screen-printing of the nanocomposites with ruthenium dye (N719) onto the titanium tetrachloride ($TiCl_4$)-treated-FTO glass. In the photocurrent-voltage characterization of the DSSCs, short circuit current density (J_{sc}) and power conversion efficiency (PCE, η) were increased by 6.0% (from 12.6 to 13.3 mA/cm^2) and 5.6% (from 7.1 to 7.5%), respectively, in comparison with the cells without the SiO_2-coated αS-AuNP-TiO_2 complexes (Figure 24b and c). Since the incident photon-to-electron conversion efficiency (IPCE) of the nanocomposite-containing DSSCs increased at the wavelength region between 450 and 550 nm where the AuNPs also absorb the light, the PCE enhancement with the improved J_{sc} would be resulted from the positive effects of LSPR. These data demonstrate that our αS-mediated AuNP coating strategy could be adequately applied to develop the plasmon-enhanced DSSCs by producing the PoP-type nanocomposites between the satellite αS-AuNPs and the core TiO_2 microsphere, which have shown multiple effects for the improvement of solar cell efficiency by exhibiting the elongation of light path due to the plasmonic property of AuNPs, the light scattering of TiO_2 microsphere, and the αS-mediated biosilicification.

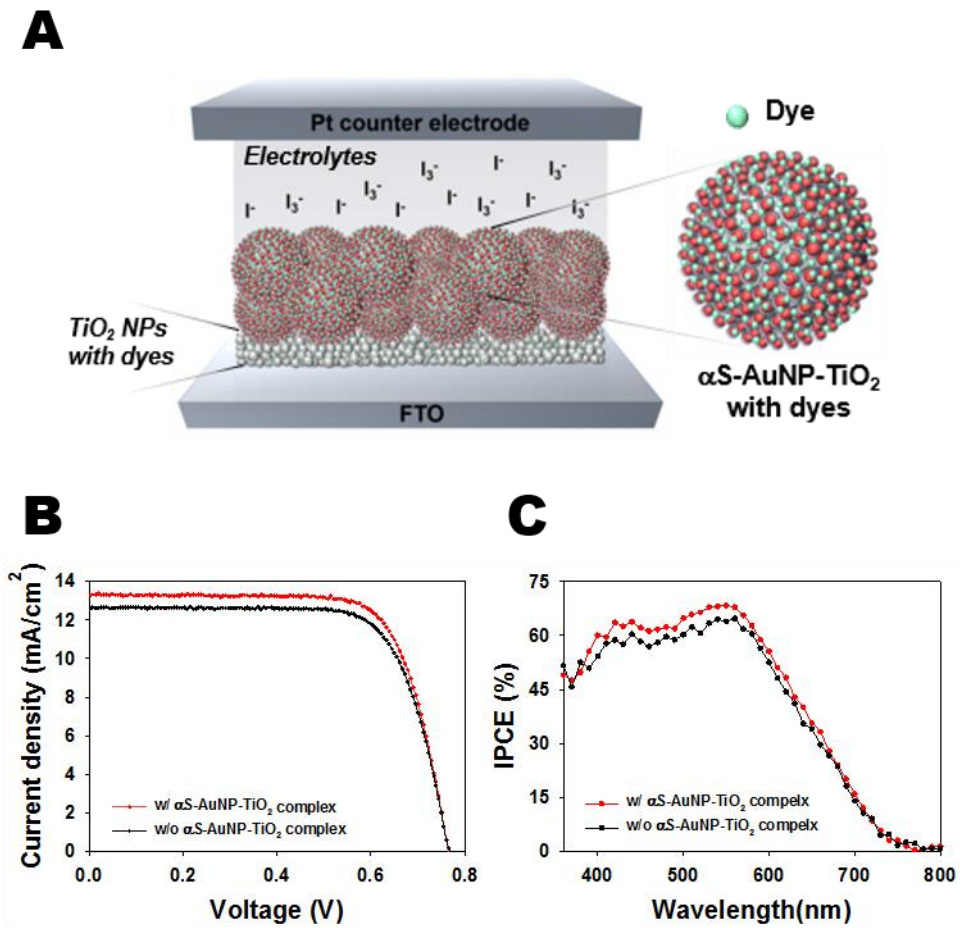

Figure 24. αS-AuNP satellites on TiO_2 microsphere and dye-sensitized solar cells. (a)Schematic drawing for the DSSC structure made of TiO_2 NP with dye sensitizer layer, SiO_2-coated-αS-AuNP-TiO_2 with dye layer, FTO electrode, and Pt-coated FTO counter electrode. (b) J-V characteristics and (c) IPCE spectra of the DSSCs with (red circle) and without (black circle) the SiO_2-coated-αS-AuNP-TiO_2 complexes.

(4) Cell Immobilization on the Diverse Surfaces of 2-D and 3-D Objects Pre-coated with the Biocompatible αS-AuNPs

To assess the biocompatible interface provided by the αS-AuNP coat, the cell attachment to the bio-unfriendly surface of fluorinated Si wafer was investigated before and after the αS-AuNP treatment (Figure 25a). The cell attachment was examined with several different types of human cells including primary human umbilical vein endothelial cells (HUVECs), primary human lung fibroblasts (LFs), human epithelial HeLa cells, and human dopaminergic neuroblastoma cells (SH-SY5Y) (Figure 25b). Confocal laser scanning microscope (CLSM) analysis indicated that all the cells were readily immobilized on the αS-AuNP-coated fluorinated surface while the fluorinated surfaces in the absence of αS-AuNPs were not able to hold the cells. Complete conversion of the interfacial property to cell-friendly environment through the αS-AuNP coating would be useful for preparing implantable therapeutic or diagnostic devices comprised of diverse non-biological materials [45]. In addition, photodynamic effect of the αS-AuNP layer made of 10-nm AuNPs to the survival of HeLa cells was verified with the light irradiation at 530 nm which corresponds to the maximum absorbance wavelength of 10-nm AuNPs revealed on the surface plasmon resonance (SPR) spectrum (Figure 25c). The number of cells remaining on the αS-AuNP coated surface decreased by 80% after only 30 s of the light illumination as determined with the confocal images while the cells cultured on a bare glass were hardly affected (Figure 25d). The light-induced cell

detachment is suggested to be attributed to the SPR-induced photothermal effect of AuNPs which would cause the thermal disruption of plasma membranes [46]. Therefore, thermoplasmonics of the αS-AuNP coats could provide us a cell manipulation strategy to get rid of the affected/cancer cells [47] as well as induce biological secretion [48].

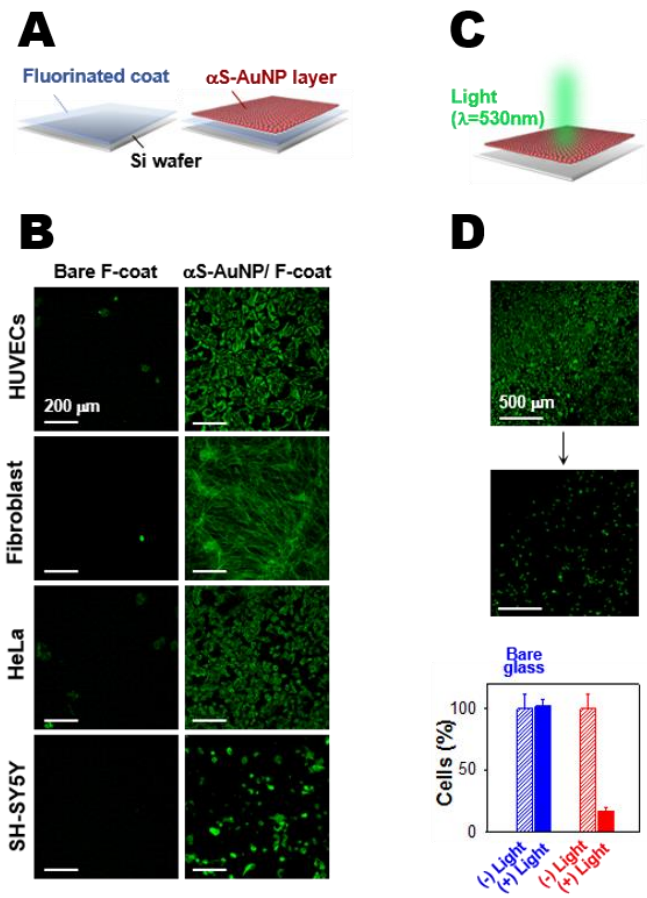

Figure 25. Cell immobilization on the substrates pre-coated with biocompatible αS-AuNPs. (a) Scheme depicting the fluorinated Si wafer (left) and the αS-AuNP-coated fluorinated Si wafer (right). (b) CLSM images of the 4 different cells of HUVECs (first row), LFs (second row), HeLa (third row), and SH-SY5Y (fourth row) on the fluorinated wafer without (left column) and with (right column) αS-AuNP coat. (c) Drawing of the αS-AuNP single-layer coat with light illumination at a wavelength of 530 nm. (d) CLSM images of HeLa cells and histogram demonstrating number of of HeLa cells on the αS-AuNP-coated Si wafer before and after the light irradiation.

In terms of culturing cells in vitro, 3-D cell culture system has been considered to be essential to create the microenvironment capable of directing proper cell differentiation and organization in a defined 3-D space for the tissue formation, which could not be achieved with either another gel-based 3-D culture system or conventional 2-D culture model [49]. The αS-AuNP coating was therefore performed for surface functionalization of the 3-D micro-channel devices. In particular, the PDMS-based micro-fluidic device was employed because of the merits of PDMS which include easy fabrication, low-cost, transparency, gas-permeability, and durability [50]. Despite of these superior properties, however, the hydrophobic surface of bare PDMS hampers its use for the direct cell adhesion [51]. In fact, the PDMS surface has been modified by employing protein coating, sol-gel chemistry, polyelectrolyte-based AuNP immobilization, and oxygen plasma treatment. However, most of them have required the complicated multi-step procedures, and the plasma-treated PDMS surface tends to lose the acquired hydrophilicity. On contrary, our approach of αS-AuNP coating would be a unique and facile alternative for the permanent bio-functionalization of 3-D micro-space single-layered with the protein-encapsulated AuNPs to enhance the cell attachment designed for 3-D cell culture.

The single-layered coat of 10-nm αS-AuNPs dramatically changed the hydrophobic surface property of the micro-channels influencing intra-channel cell transport and attachment. At the beginning of HUVEC culture, the cells were able to enter the micro-channels coated with the αS-AuNP conjugates

whereas the bare PDMS channels did not permit the cell's entry (Figure 26a). Even after 17 h of the cell culture, the cells were still hardly found in the bare PDMS channels while the confluent cells were found to be adhered on the inside surface of the αS-AuNP-coated channels. With CLSM analysis, anti-αS antibody (LB509) with Alexa 594-labeled secondary antibody staining revealed the presence of αS molecules, indicating that the αS-AuNP coat was maintained during the cell culture to promote the cell adhesion and proliferation (Figure 26b). The fluorescence staining with 4',6-diamidino-2-phenylindole (DAPI) and phalloidin visualized the adherent HUVECs showing nuclei and F-actin filaments aligned within the micro-channels of 50, 100, and 200 μm in width. The 3-D reconstruction of the confocal image of F-actin filaments within the 200 μm channels and the reconstituted cross-section of one of the channels showed that the adherent cells covered virtually all the surface within the channel (Figure 26c). These results, therefore, demonstrate that the αS-AuNP layer successfully modifying the physically inaccessible 3-D space within the micro-fluidic device could be applied for developing the 3-D cell-culture platforms for organ-on-a-chip which can be used for *in vitro* disease model development and drug discovery.

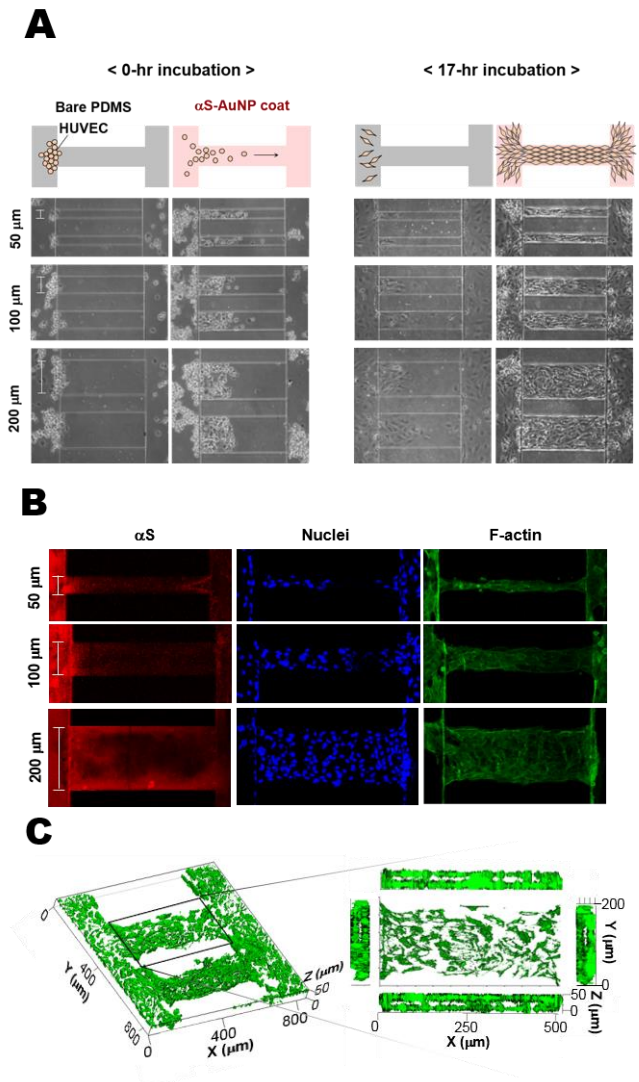

Figure 26. 3-D cell culture in αS-AuNPs single layer coated PDMS micro-channels. (a) Drawings (first row) and optical microscope images of HUVECs in micro-channels with the width of 50 μm (second row), 100 μm (third row), and 200 μm (fourth row). (b) Immuno-fluorescent images of αS and HUVECs on the inside surface of micro-channels. (c) CLSM analysis for the reconstructed 3-D image of phalloidin-stained HUVECs in the micro-channels with 200 μm in width (left) and the high-magnification cross-sectional image.

(5) αS-AuNP/Graphene Oxide sheets for Hybrid sheets for photothermal cancer therapy

Our strategy for photothermal cancer therapy is based on adhesion of αS-AuNP/GO complex onto MSCs with tumor-tropic property (Scheme 4) [52]. As mentioned above, utilization αS-AuNP/GO complex instead of non-orgnaized AuNP has merits of i) reduction of cell cytotoxicity, ii) enhancement of loading efficiency, and iii) red-shift of absorption spectra for the increase in photothermal efficiency. The decrease in cell cytotoxicity comes from external loading of AuNPs, which is differentiated from endocytosis of unorganized AuNPs. In the same reason, the problem of leakage in un-assembled AuNPs induced by exocytosis is reduced in the case of αS-AuNP/GO complex. Finally, the enhancement of phototermal efficiency comes from the plasmon coupling between adjacent AuNPs in the complex, which increases absorption of NIR range light.

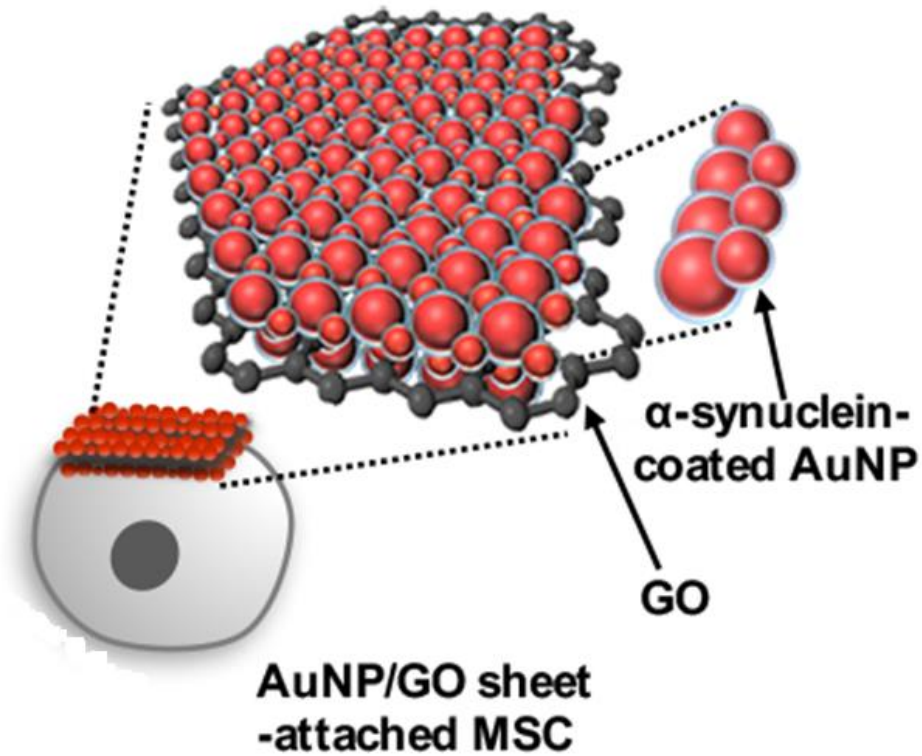

Scheme 4. Schematic illustration of αS-AuNP/GO complexs attached on tumor-tropic MSCs. αS-AuNP/GO complexs were prepared by adsorbing αS AuNPs on both sides of micro-sized GO flakes. αS-AuNP/GO complexs were stably attached to tumor-tropic MSC surface and exhibited enhanced photothermal capability.

Before the fabrication the αS-AuNP/GO complex, the preparation of αS-$AuNP_{30nm}$ and αS-$AuNP_{20nm}$ after the ultra-centrifugation for the residual αS removal was verified with DLS analysis (Figure 27a) [30,32]. For both sizes of AuNPs, the hydrodynamic radius increased about 8.5 nm, which indicates the preparation of stable αS-AuNP complexes. αS-$AuNP_{30nm}$ and αS-$AuNP_{20nm}$ were sequentially adosorbed onto GO with brief sonication. The preapared αS-AuNP/GO complexs was revealed as tri-layered structure of the tightly packed AuNP single layers sandwiching the GO via SEM and TEM analysis (Figure 27b,c). By measuring height profile of the complex with AFM analysis, we verified that the αS-AuNP/GO complexs had a thickness of ~ 60 nm, which is comparable to the thickness of two single layers of αS-$AuNP_{30nm}$ (Figure 27d). Clear D peak (~1350 cm^{-1}) and G peak (~1600 cm^{-1}) in Raman spectra of αS-AuNP/GO complexs showed that there was no significant chemical damages or modifications in GO during the intercaltion into the complex (Figure 27e).

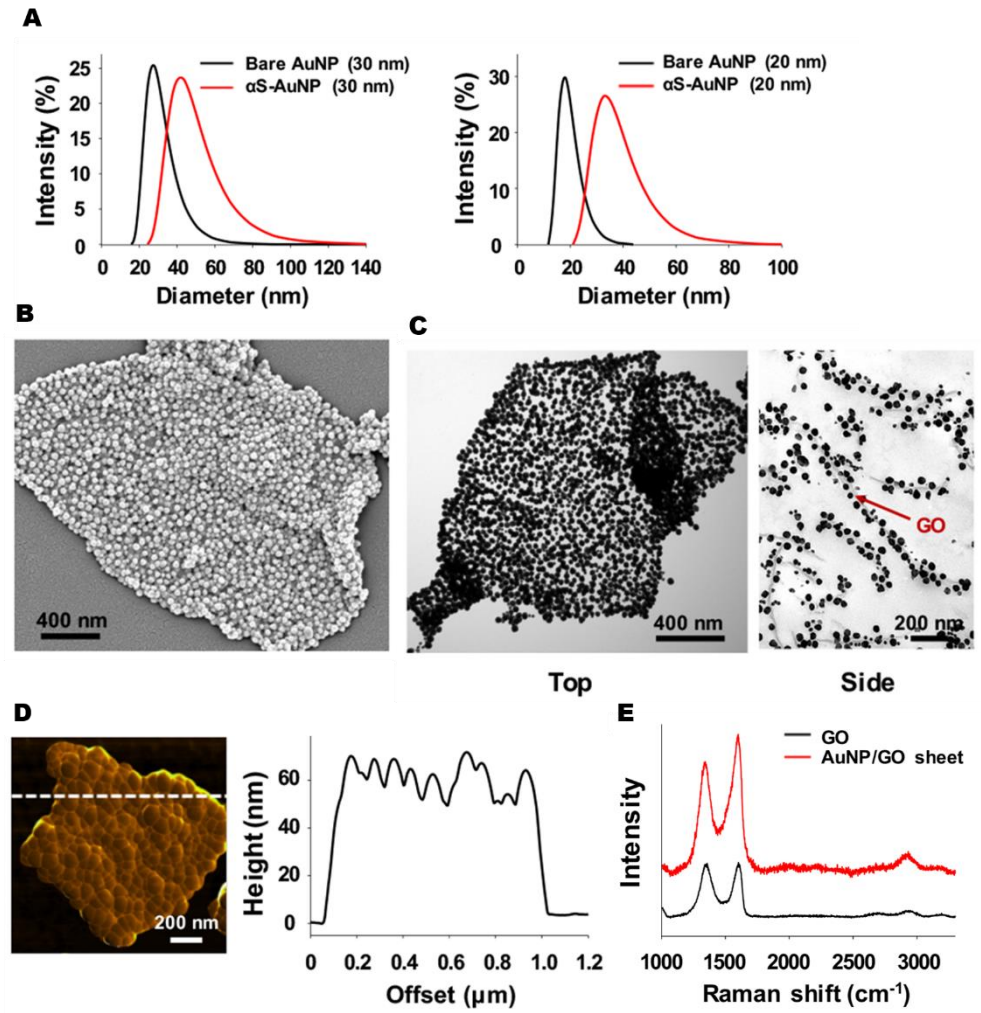

Figure 27. Characterization of αS-AuNPs and αS-AuNP/GO complexs (a) Hydrodynamic size of 30 nm (left) and 20 nm (right) AuNPs before and after α-ynuclein encapsulation. (b) SEM image of αS-AuNP/GO hybrid sheet. (c) TEM images of AuNP/GO hybrid sheet viewed from top and side. The 30 nm and 20 nm AuNPs coated with αS were absorbed on both sides of GO sheets. (d) AFM image of AuNP/GO sheet and the height profile along the line shown in the AFM image. (e) Raman spectra of GO and AuNP/GO sheet.

It is important to note that AuNPs with two different sizes were used to enhance photothermal efficiency. αS-AuNPs adsorb randomly onto GO without significant specific site preference, so, after the first adsorption process of αS-$AuNP_{30nm}$, there should be empty sites on GO between the larger AuNPs in which only smaller particles can access. In this respect, the serial adsorption steps of αS-$AuNP_{30nm}$ and αS-$AuNP_{20nm}$ were performed to maximize the plasmon coupling between adjacent AuNPs, which led to enhancement in photothermal efficiency. It was able to compare the packing density between αS-$AuNP_{30nm+20nm}$/GO complexs and αS-$AuNP_{30nm}$/GO complexs via SEM analysis (Figure 28a). The packing density of αS-$AuNP_{30nm+20nm}$/GO complexs was higher than that of αS-$AuNP_{30nm}$/GO complexs, leading to further red shift in their abosroption spectra (Figure 28b). The abosrobance of αS-$AuNP_{30nm+20nm}$/GO complexs at 808nm, the wavelength of NIR laser for photothermal therapy, increased 41 % compared to that of αS-$AuNP_{30nm}$/GO. We evaluated the photothermal effect of two different complexs and unorganized AuNPs by measuring the temperature increase under the NIR laser irradiation (808 nm, 1.5 W/cm, 5min) (Figure 28c,d). As expected, αS-$AuNP_{30nm+20nm}$/GO complexs showed the highest temperature increase of 23.2 ℃. To maximize the peformane of *in vivo* photothermal therapy, we have used αS-$AuNP_{30nm+20nm}$/GO complexs in the following experiments.

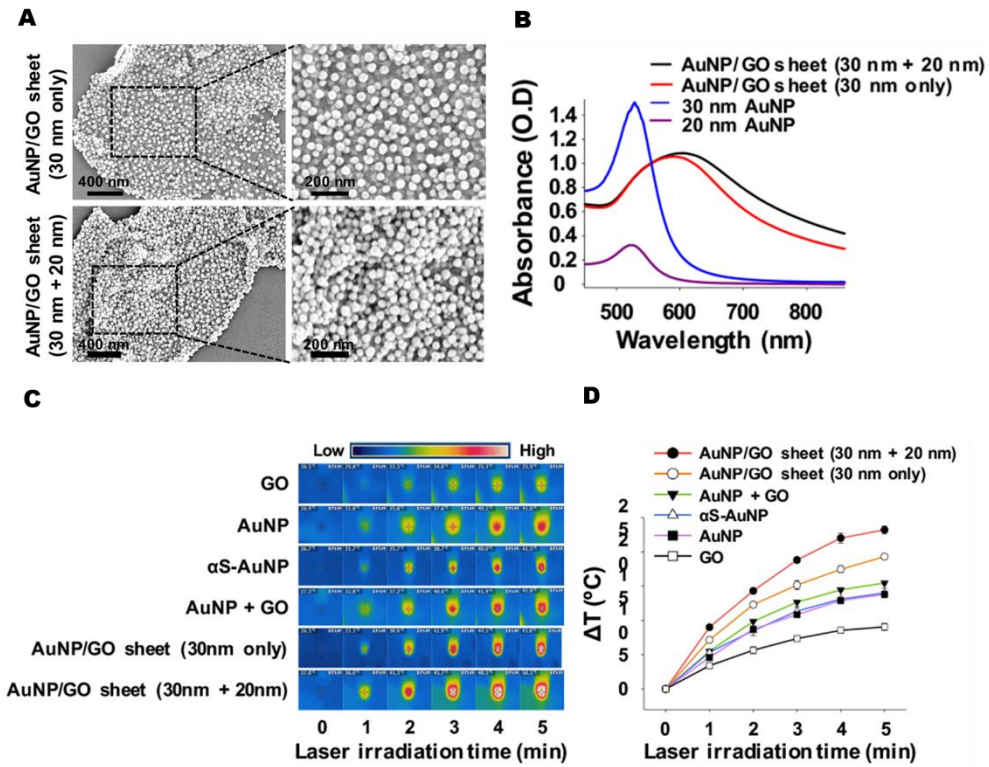

Figure 28. Plasmon coupling and optical property of αS-AuNP/GO complexs

(a) SEM images of αS-AuNP/GO complexs consisting of 30 nm AuNPs only (top) and 30 nm + 20 nm AuNPs (bottom). (b) Absorption spectra of the colloidal solutions of bare AuNPs (20 nm and 30 nm) and αS-AuNP/GO complexs (30 nm only and 30 nm + 20 nm). (c) and (d) Photothermal effects of GO, AuNP, αS-AuNP, AuNP + GO, αS-AuNP/GO complexs sheet (30 nm only), and AuNP/GO sheet (30 nm + 20 nm). Temperatures were monitored during 808 nm laser irradiation (n = 5).

αS-AuNP/GO complexs were loaded onto MSCs (αS-AuNP/GO/MSCs) by co-culture for a day. The distribution of αS-AuNP/GO complexs was evaluated via TEM analysis (Figure 29a). αS-AuNP/GO complexs successfully integrated with cell membrane as expected from the result of previous 3-D cell-culture system experiment, whereas the unassembled AuNPs located within the intracellular vesicles. The main difference that made the contrast in distribution between the complexs and unorganized AuNPs was the size of individual nanomaterial. It has been reported that nano-sized GO internalizes into cells while micro-sized GO attatches onto cells because of its size [53,54]. As shown in Figure 28a, the GO used for the experiment was micro-sized, which led to the fabrication of microscale hybrid GO complex.

To evaluate the *in vivo* applicability αS-AuNP/GO/MSCs, we assessed the stability of the adhesion between αS-AuNP/GO and MSCs under the fluid shear stress. The stability under fluid shear stress is important because the fluid shear stress mimics the circumstance of blood vessel. Comparision of fluorescence images acquired before and after applying shear stress revealed that αS-AuNP/GO complexes were stably adhered onto the MSCs after the fluid shear stress. We have investigated the mechanism of the attachement via western blot. After the treatment of αS-AuNP/GO complexes, the expression level of integrin β1 and fibronectin increased a lot, which are the adhesion-receptor and the extracellular matrix (ECM) protein, respectively [55]. It is noteworthy that the expression level of integrin β1 increased far more than

that of fibronectin, which indicates direct interaction between αS and integrin β1 as previous study has suggested [56].

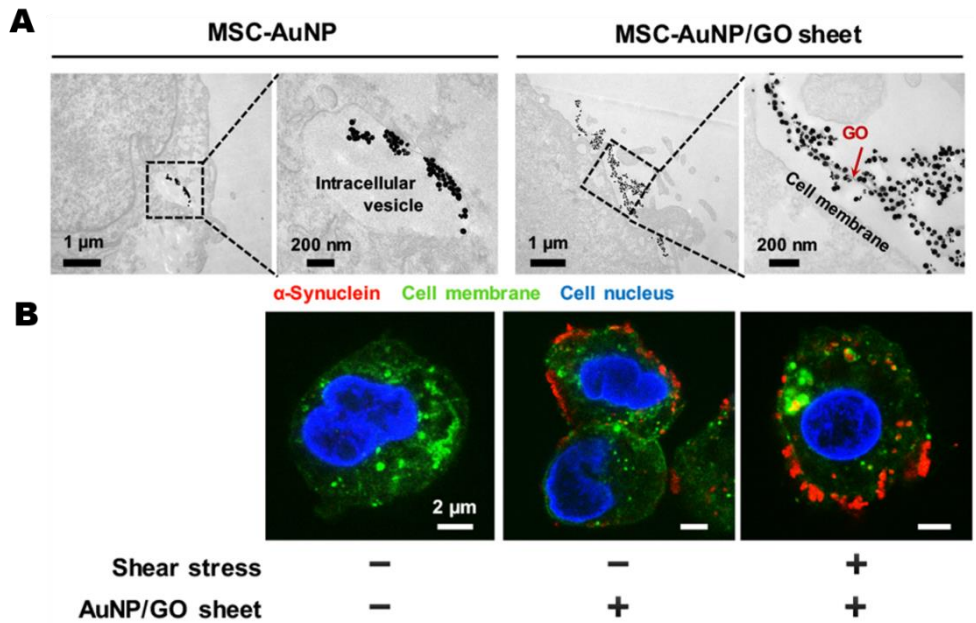

Figure 29. Adhesion of αS-AuNP/GO complexs on MSC surface. (A) TEM images of AuNPs internalized within the MSC and αS-AuNP/GO complexs attached on MSC surface. (B) Stability αS-AuNP/GO complexs attached on MSCs, as evaluated by exposing the cells to shear stress and immunostaining for Σ (red) in αS-AuNP/GO complexs. The cell membrane and nucleus of MSC were stained with PKH67 (green) and DAPI (blue), respectively.

To examine the *in vivo* photothermal efficacy, we intravenously injected αS-AuNP/GO/MSCs into tumor-bearing mice, and applied NIR laser (808 nm, 1.5 W/cm^2, 5 min) three days after the injection. As control groups, the effects of phosphate-buffer saline (PBS), AuNP, MSC, αS-AuNP/GO complex, and four-fold diluted αS-AuNP/GO/MSC were tested with same procedure. IR thermal imaging result revelaed that photothermal efficacy of αS-AuNP/GO/MSC-injected-group far exceeds those of other experimental groups and the temparture of αS-AuNP/GO/MSC-injected-group was increased upto 58.0℃, which is high enough temperature to induce cell death (Figure 30a) [57]. After the irradiation, we tested the anti-cancer effect for the following 21 days in comparison with that of non-irradiated PBS-injected-group (Figure 30b). Among all the experimental groups, only mice belonging to the αS-AuNP/GO/MSC-injected-group showed a definite removal of tumor volume. In accordance with these images, only αS-AuNP/GO/MSC-injected-group obviously showed the suppression of tumor growth over the 21-day evaluation period. However, other experimental groups exhibited comparable result with non-irradiated PBS-injected-group only except four-fold diluted αS-AuNP/GO/MSC-injected-group that suppressed about a half of tumor growth. In conclusion, we have developed novel and effective photothermal cancer therapy system based on the adhesive and cell-interactive properties of αS-AuNPs, leading to effective delivery toward cancer region in the hierarchical complex structure with GO and MSCs.

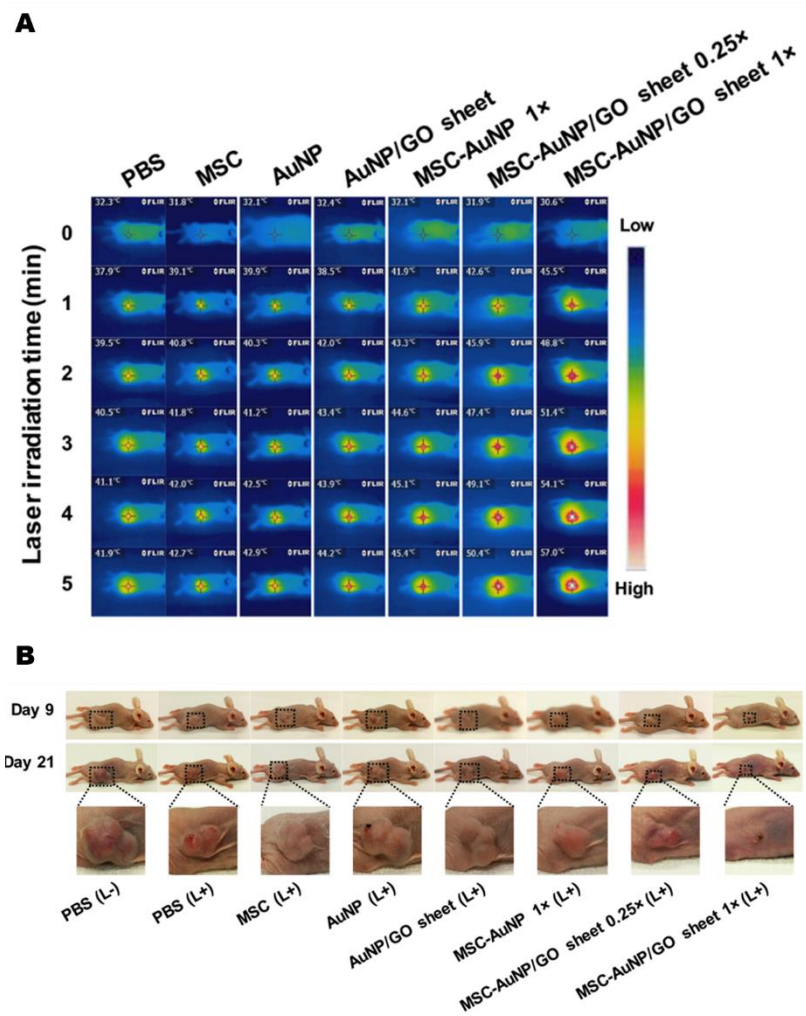

Figure 30. In vivo photothermal therapy result of MSC-AuNP/GO sheet. (a) Real-time infrared thermal images. Three days after intravenous injection of samples into tumor-bearing mice, the tumors were exposed to NIR laser irradiation for 5 min under anesthesia. (b) Representative mouse images of the laser irradiation groups and PBS (L−) group on day 9 and 21 after laser irradiation.

II-4. Conclusions

This study has shown that multiple uses of αS-AuNPs via the universal procedure to immobilize AuNPs onto the diverse types of substrates in a high-density single-layer by using the natural protein of αS exhibiting omni-adhesive property. Our solution-based approach was capable to form the αS-AuNP singl-layer coat onto the surface of PMMA 2-D layer, CNTs, TiO_2 microsphere, PDMS/glass microchannel, and GO. Versatility in the use of αS-mediated AuNP adsorption has been demonstrated in the areas of flexible non-volatile memory development, fuel cell performance improvement, solar cell efficiency enhancement, 3-D platform development for cell culture, and photothermal cancer therapy, where the outer αS played diverse roles besides the surface adsorption such as the dielectric layer, the sacrificial layer for AuNP exposure, the reaction center for silicification, and the bio-interface for cell attachment, respectively. Future trials of preparing the αS conjugates with various NPs and their adsorption onto a diverse set of substrates would open up a plethora of applications in the area of nanotechnology, which require NPs exerting their sustained activities in the surface-immobilized states.

Part III. Free-standing Gold-nanoparticle Monolayer Film Fabricated via Protein Self-assembly of α-Synuclein

III-1. Introduction

2-Dimensional nanofilms have been intensively fabricated with various materials, including graphene [58], surfactant [59], and inter-penetrating polymer network [60], to take advantages of ultra-thin thickness in electronic devices or membrane systems [61,62]. In this respect, free-standing ultrathin films of NPs have garnered a great deal of interest in materials science [63] especially to make those particles used in the development of realistic devices. The free-standing nanoparticle films have been produced via spin-assisted layer-by-layer (LbL) assembly [64], cross-linking based interfacial assembly [65,66], and drying mediated self-assembly [63,67]. The NPs inside have been linked together with binders such as polyelectrolytes [64], chemical ligands [65-67], and biomolecules [63]. In the case of LbL assembly, multilayered nanocomposite membrane was prepared by sandwiching a central AuNP layer with multiple polymer layers on both sides [64]. Although the AuNPs enhanced mechanical robustness of the polymer membrane, the particles were not packed tightly enough for additional applications. Using the interfacial-assembly, densely packed NP monolayer was produced after cross-linking them between two immiscible fluids [65,66]. In the drying-

mediated method, well-organized AuNP arrays were also successfully prepared by using either dodecanethiol- or DNA-conjugated nanoparticles [63,67]. These constructs, however, could not be expanded beyond micrometer scale as they were produced over microholes.

In this study, a bio-based strategy has been introduced to produce a free-floating ultrathin AuNP sheet where AuNPs are tightly packed in monolayer by employing a self-associative protein of αS as a binding agent and adhesive property of αS-AuNPs mentioned in Part I [29]. The resulting transparent two-dimensional (2-D) AuNP sheets are readily expandable, flexible and thus exhibiting conformal contact, patternable, and air/dry-stable. It is these characteristics that would allow the sheets to take crucial parts in their realistic applications.

III-2. Experimental Section

(1) Fabrication of free-standing αS-AuNP Film

The AuNP monolayer films were prepared via two steps: adsorbing the S-AuNPs onto a 30-μm-thick polycarbonate (PC) substrate (2 x 2 cm) (SEJIN TS, Korea) to form the AuNP monolayer, and then dissolving the substrate to give rise to simultaneous association between the αS-AuNPs through specific αS–αS interactions. To induce optimal adsorption of αS-AuNPs onto the substrate, pH of the solution containing αS-AuNPs was changed from 6.5 (20

mM MES) to 4.5 (50 mM citrate). The buffer exchange was carried out by precipitating the αS-AuNP conjugates with the centrifugation at 16,100 x g and re-suspending the resulting precipitates in the new citrate buffer. A 50-μL droplet of the αS-AuNP solution was then immediately placed on top of the PC substrate, which was pre-treated with oxygen plasma (CUTE-MPR, FEMTO SCIENCE, Korea) at 60 W for 1 min. After incubation in a humidified chamber at 40ºC for 3 h, the particle-loaded substrate was thoroughly washed with deionized (DI) water (Direct-Q, Millipore, Germany). The underlying PC layer was subsequently dissolved with chloroform (HPLC grade, Fisher, MA) while facilitating the self-assembly of αS-AuNPs. The resulting αS-AuNP monolayer film was freely suspended in the solvent. After replacing the PC-containing chloroform with the fresh solvent, the free-floating αS-AuNP film was transferred to the surface of slide glass (MARIENFELD, Germany) or silicon wafer (Siltron Inc., Korea).

(2) Cutting PC substrate into 2-D shape

Using a cutting machine (Craft Robo, Graphtec, Japan), a 30-μm-thick PC substrate was cut into circles patterned by a computer-aided design (CAD) software (AutoCAD 2012). The αS-AuNPs were adsorbed onto the substrates to form a monolayer, which were then developed in chloroform to yield the free-floating films coded by the circular PC substrates.

(3) Preparation of microfluidic devices for micro-patterning of αS-

AuNP film

Microfluidic devices were fabricated via soft lithography and rapid prototyping. Master molds were manufactured by patterning thick negative photoresist SU8-100 (MicroChem, Newton, MA) on Si wafers using patterns designed with the CAD software package. Positive replicas with embossed micro-channels were then produced by casting poly(dimethylsiloxane) (PDMS) (Sylgard 184, Dow Corning, Midland, MI) in the master molds. The PDMS solution was prepared by mixing pre-polymer and curing agent at 8:1. Following curing at 80℃ for 40 min, the PDMS molds were peeled off from the master molds. To have a port to inject the AuNPs, holes were punched on the PDMS using a needle. The PDMS was then brought into contact with the plasma-treated 30-μm-thick PC substrate for 30 min after activation of both surfaces of PDMS and PC substrate in oxygen plasma chamber for 1 min (at 500 mTorr and 60 W). In fact, the PC substrate was already pre-treated with one previous round of oxygen plasma at 60 W for 1 min, which was followed by subsequent functionalization with 1% solution of (3-aminoprpyl)triethoxysilane (APTES) (Sigma-Aldrich) for 20 min[68].

(4) Micro-patterning of αS-AuNP monolayer film

Micro-pattering of αS-AuNP film was achieved by using the microfluidics system. The patterns were produced by injecting the αS-AuNP dispersion into the PDMS microfluidic soft lithography mold. During incubation at 40℃, αS-

AuNPs were adsorbed onto the patterned surface of PC substrate under the micro-channels. The channels were washed with DI water following the AuNP adsorption. After detaching the PDMS mold from the PC substrate, the αS-AuNPs adsorbed onto the PC surface were dissolved in chloroform to obtain a micro-patterned film of the αS-AuNP monolayer.

(5) Testing of AuNP film formation with bovine serum albumin (BSA), amyloid-β (Aβ), κ-casein (κCN), and β-2 microglobulin (β_2M)

The AuNP film production was tested with the particles coated with proteins other than αS including BSA, Aβ, κCN, and β_2M. β_2M was prepared according to the procedure previously reported [69]. BSA, Aβ, and κCN were purchased from Sigma-Aldrich. The identical procedure employed for preparation of the αS-AuNP film was performed for the particles coated with the proteins listed above. For the protein-AuNP conjugates with Aβ and β_2M, they agglomerated and adsorbed onto the surface of Eppendorf tubes during the preparation procedures. Those aggregated AuNPs were examined with FE-SEM. For BSA, κCN, and β_2M, the resulting PC surface with the protein-particle conjugates adsorbed was examined with FE-SEM.

(6) Flexibility of the αS-AuNP monolayer film

Flexibility of the αS-AuNP film was investigated by observing its motion in

chloroform. The film readily crumpled and then unfolded to its original extended form by applying a gentle flow of chloroform. The motion of film was recorded with a movie camera (LG-F180S, Korea) at a resolution of 4208 x 3120 pixels.

(7) Conformal contact of the αS-AuNP film

The αS-AuNP film was transferred onto the regularly curved surfaces provided by the 1.16-μm-diameter SiO_2 beads (Micro Particles GmbH, Germany).

(8) Stability of the αS-AuNP film

The αS-AuNP films made of 20-nm-diameter AuNPs were transferred onto glass slides to investigate stability of the films against the elevated temperatures and the solvents in different polarities. To evaluate the temperature effect, the films were examined with an optical microscope during a 7-day period under an ambient condition at 80℃. To investigate the film's durability in aqueous condition, the films were also examined over a 7-day period while immersed in 20 mM MES (pH 6.5) at 37℃. Surface plasmon resonance (SPR) spectra of the films were monitored using Raman spectrophotometer (InVia, Renishaw, UK) to find out any damages on the AuNP array following the treatments. The SPR spectra were obtained on the same location of the film before and after the incubations. For the

investigation of the film's stability in organic solvents, the films were immersed in ethanol, acetone, dimethyl sulfoxide (DMSO), or acetonitrile for 1 h. The SPR spectra of the films were obtained at three different locations of each film and compared with each other by obtaining the mean absorption between 645–655 nm. Those spots of monitoring SPR signals remained unchanged before and after the solvent exposure.

(9) Formation of wafer-scale αS-AuNP films

A 30-μm-thick PC sheet was cut into the shape of a silicon wafer using the Craft Robo cutting machine, which was then treated with oxygen plasma at 60 W for 1 min. The resulting PC substrate was smeared with a 10-ml aliquot of the αS-AuNP colloidal dispersion made of 10-nm-diameter AuNPs. Following an incubation for 3 h at 40^{o}C, the PC substrate was washed with a sufficient amount of DI water. The PC was then dissolved with chloroform to obtain a 4-inch-diameter αS-AuNP film.

(10) Fabrication of double-component AuNP films

Double-component αS-AuNP films were fabricated by separately adsorbing two groups of αS-AuNPs containing either 10- or 20-nm AuNPs into two halves of a round-shape PC substrate with a diameter of 1.5 cm. After the oxygen plasma treatment, the substrate was placed at the center of a plastic paraffin film in 4 × 4-cm. A half of the circular PC substrate was masked with

a paraffin film. The other half was exposed to the αS-AuNPs containing 20-nm-diameter AuNPs. The mask was then removed, and the remaining semi-circle was exposed to another colloidal dispersion of αS-AuNPs with 10-nm-diameter AuNPs. The double-component free-floating films were produced by dissolving the supporting PC substrate in chloroform. Another free-floating film of the 'SNU' logo was also generated with the 10-nm-diameter AuNPs for the background and the 20-nm-diameter AuNPs for the letters by the same procedure described above.

III-3. Results and Discussion

(1) Free-standing film of αS-AuNPs

Our protein-based approach of preparing the free-standing AuNP single-layered sheet consists of three steps. First, αS-coated AuNPs (αS-AuNPs) were prepared by incubating a mixture of wild-type αS and colloidal AuNPs for 12 h at 4°C, followed by removal of the unbound αS. The αS-AuNP conjugates were then non-covalently adsorbed onto a plasma-treated polycarbonate (PC) substrate to form a closely packed monolayer at pH 4.5. By dissolving the PC substrate in chloroform, the AuNP monolayer was unleashed as a free-standing film from the sacrificial substrate. (Scheme 5)

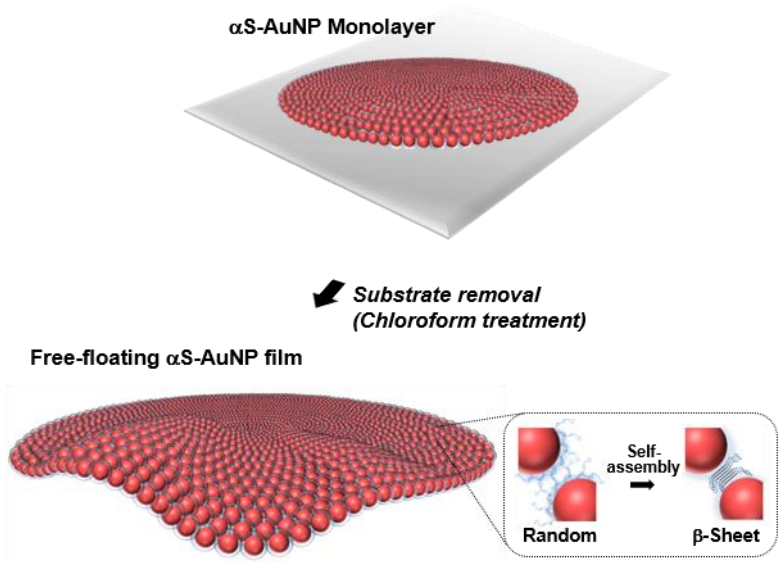

Scheme 5. Schematic diagram showing the fabrication strategy of free-floating αS-AuNP monolayer film. Free-standing film production with αS-αS self-assembly upon removal of the substrate with chloroform.

The resulting film prepared with 20-nm-diameter AuNPs was transparent in purple-blue (Figure 32a). A scanning electron microscope (SEM) image of the film is shown in Figure 32b. The film made of 10-nm-diameter AuNPs appeared bright pink (Figure 32c). Its transmission electron microscope (TEM) image reveals that the AuNPs were tightly packed in monolayer (Figure 32d). The film's flexibility was illustrated with a series of images of the film in the solvent (Figure 32e). The crumpled film unfurled into a planar state, and it folded back. The films formed with 20- and 30-nm AuNPs exhibited the similar behavior of flexibility in the solvent (Figure 32f, g). The free-standing αS-AuNP film was successfully expanded to the size of 4-inch wafer and shown to be floating intact in bright pink (Figure 32h). Although most methods currently available have tried to produce the NP films in centimeter-scale, the wafer-scale film with NPs packed as tightly as demonstrated here has never been achieved.

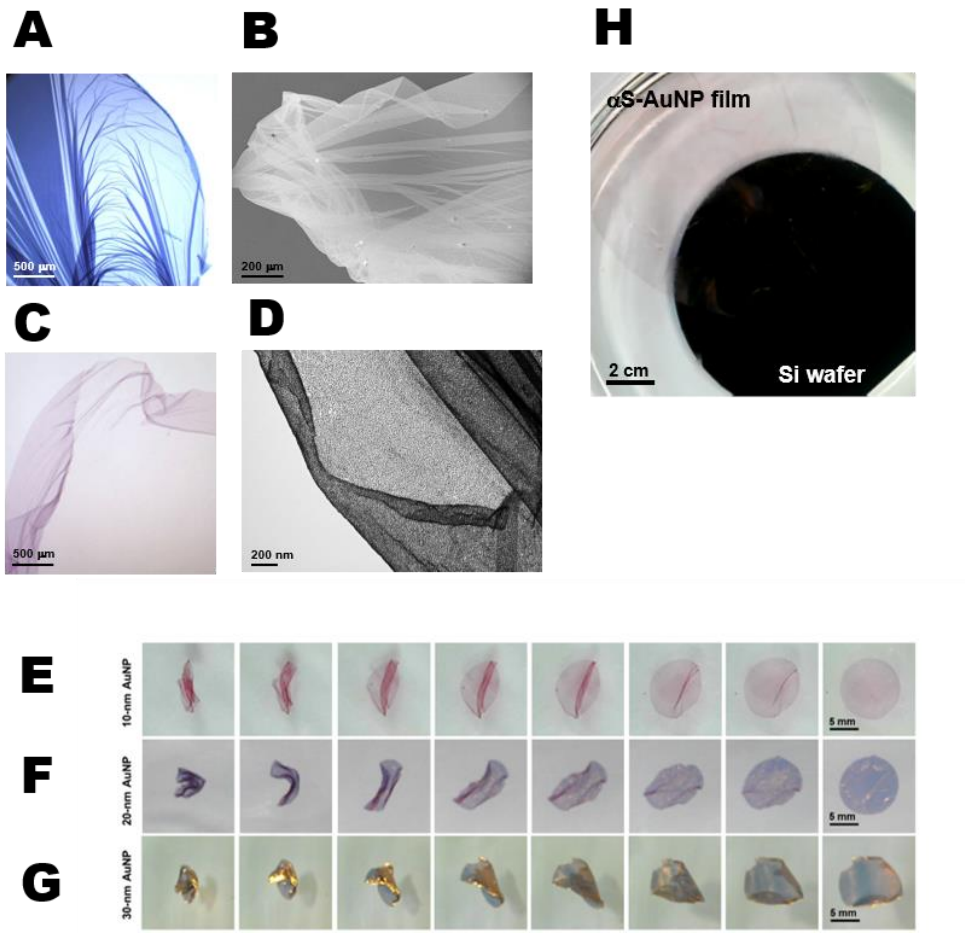

Figure 31. Flexible free-standing αS-AuNP monolayer films. a, b) Optical (a) and SEM (b) images of the αS-AuNP monolayer film prepared with 20-nm-diameter AuNPs. c, d) Optical microscope image (c) and TEM image (d) of a αS-AuNP monolayer film made of 10-nm-diameter AuNPs. e, f, g) Serial images of free-standing αS-AuNP films composed of 10-nm-diameter AuNPs (e), 20-nm-diameter AuNPs (f), or 30-nm-diameter AuNPs (g) showing the film's flexibility in chloroform. f) Optical image of a wafer-scale αS-AuNP film (indicated by dotted line) floated from the background 4-inch Si wafer.

(2) The role of αS for the fabrication of free-standing film

(2)-1. Interaction between αS-AuNP

The αS-AuNP films were produced based on three specific interactions between αS and individual AuNPs, between αS and the polymer substrate, and between αS and αS, leading to the αS-AuNP formation, the αS-AuNP adsorption onto the substrate, and the αS-αS self-assembly, respectively. Homogeneity of the αS-AuNP conjugates was assessed with dynamic light scattering (DLS) analysis (Figure 32a). The protein coat increased the average diameter of colloidal AuNPs from 20.6 to 38.4 nm. This 18 nm increase in the diameter is consistent with the previous studies investigating the hard corona formation of αS on AuNPs [24,70]. A flocculation assay indicated that a well-dispersed colloidal state was maintained for the αS-AuNPs even at a high salt concentration of 1.25 M NaCl (Figure 32b). On the contrary, other protein-AuNP conjugates prepared with another amyloidogenic peptide/protein of either amyloid-β (Aβ) or β2-microglobulin (β2M) yielded non-specific agglomerates of the particles as they formed during washing steps of the conjugate preparation (Figure 32c), indicating that the αS interaction with AuNPs is unique to generate the homogeneous αS-AuNP conjugates.

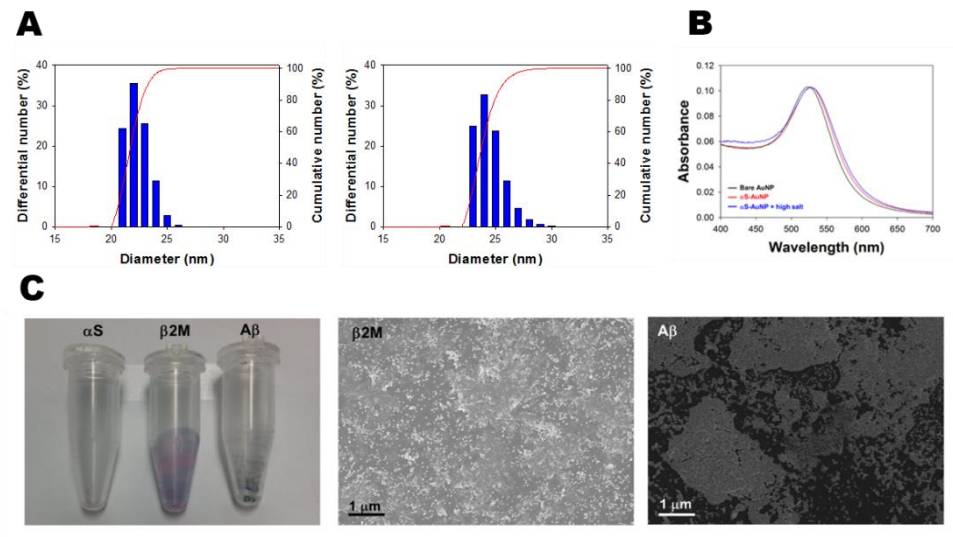

Figure 32. Coating AuNPs with αS. (a) DLS histograms of bare AuNPs (left) and αS-AuNPs (right). (b) Absorption spectra of the colloidal solutions of bare AuNPs (black line), αS-AuNPs (red line), and the αS-AuNPs in the presence of 1.25 M NaCl (blue line). (c) Images of Eppendorf tubes left behind after being used with αS-AuNPs, β_2M-AuNPs, or Aβ-AuNPs. (left) The tubes were collected after thorough washing to remove free proteins. SEM images of the surfaces of the tubes adsorbed with β_2M-AuNPs (middle) and Aβ-AuNPs (right).

(2)-2. Interaction between αS-AuNP and PC substrate

The adsorption process of αS-AuNPs onto PC substrate was also specific for the protein since the monodispersed array of the nanoparticles was not obtained with other soluble proteins such as amyloid-β (Aβ), abovine serum albumin (BSA), β2M, and κ-casein (Figure 33). These proteins produced rather non-specific agglomerates of AuNPs on the plasma-treated substrate. Therefore, the monolayer formation of αS-AuNP on the PC substrate, a critical prerequisite for the free-floating ultrathin AuNP film formation, was considered to be achieved via not only a preferential surface interaction of the αS to the substrate, but also an unaccommodating αS-αS interaction between the αS-AuNPs pre-attached on the surface and the upcoming αS-AuNP conjugates at the acidic pH of 4.5 and the temperature of 40℃ employed in this experiment. Packing density of the αS-AuNP monolayer improved as the incubation proceeded. The packing density increased from 472.0 ± 15.7 μm^{-2} for 5 min adsorption, 646.3 ± 10.1 μm^{-2} for 30 min, 706.7 ± 10.6 μm^{-2} for 60 min, to 1,005.0 ± 6.1 μm^{-2} for 180 min (Figure 34a). The specific adsorption of AuNPs mediated by αS was demonstrated to be dependent upon the surface property of PC substrate in addition to the incubation time. The packing density of αS-AuNPs on a PC substrate drastically decreased from 1,022.0 ± 9.2 μm^{-2} to 664.7 ± 12.3 μm^{-2} without the O_2 plasma treatment (Figure 34b). For the free-standing films, the packing density dropped from 1101.7 ± 3.5 μm^{-2} to 714.3 ± 11.0 μm^{-2} as they were prepared from the PC substrates without the plasma pre-treatment (Figure 34c). In addition, a

considerable amount of AuNPs agglomerates were formed on the plasma-treated substrate as the adsorption temperature increased from 60℃ to 80℃ (Figure 34d).

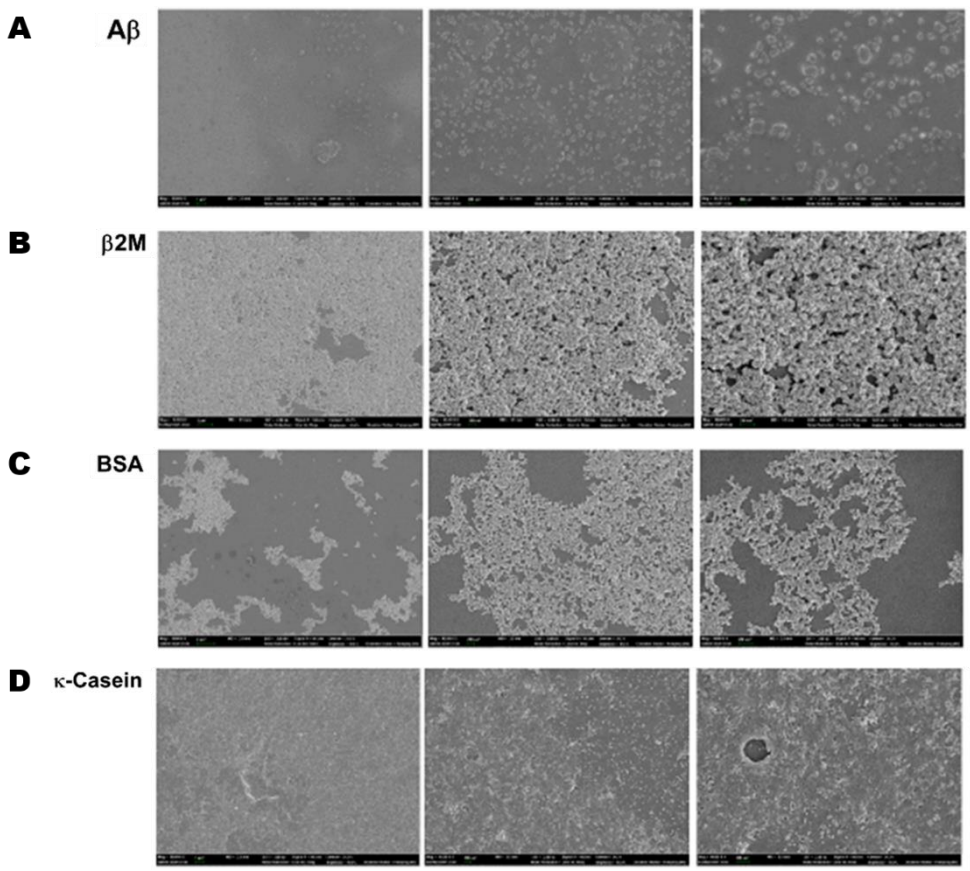

Figure 33. Tests of protein-AuNP monolayer adsorption. SEM images of protein-AuNP layer using Aβ (a), β_2M (b), BSA (c), or κ-casein (d).

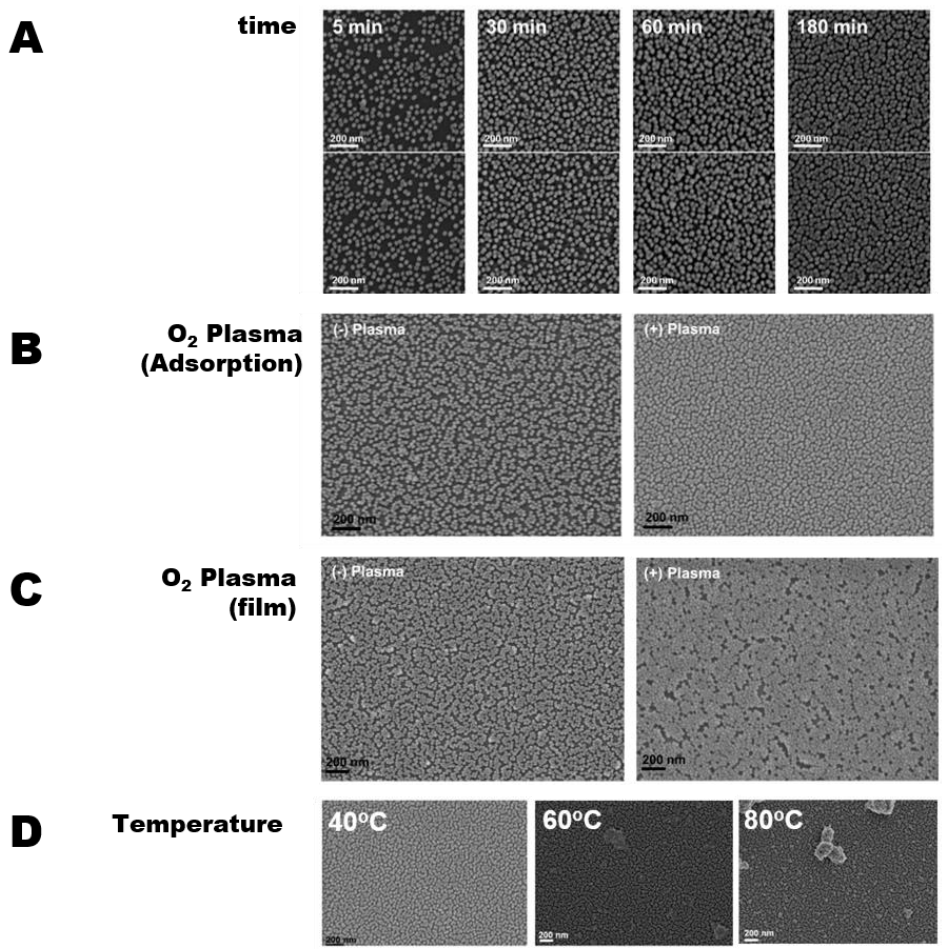

Figure 34. Optimization of film formation. (a) SEM images of the αS-AuNPs on PC substrates following adsorption for 5 min, 30 min, 60 min, and 180 min. (b) SEM images of αS-AuNPs adsorbed on non-plasma-treated (left) and plasma-treated PC substrates (right). (c) SEM images of αS-AuNP films fabricated by using the non-plasma-treated (left) and plasma-treated PC substrates (right). (d) SEM images of the adsorbed αS-AuNPs on plasma-treated PC substrates after 3 h incubation at 40°C (left), 60°C (middle), and 80°C (right).

(2)-3. Interaction between αS-AuNP and αS-AuNP

As the underlying PC substrate was dissolved in chloroform, the AuNPs in the floating film became held together through the αS–αS self-association. Under SEM, the intriguing fibril-like connections were revealed between the particles (Figure 35a). Considering αS as an amyloidogenic protein, those interconnections were presumed to be formed via the β-sheet structure in chloroform [71]. Deconvolution of an attenuated total reflectance Fourier transform infrared (ATR-FTIR) spectrum (Figure 35b) confirmed the presence of the β-sheet structure as unraveled with the bands at 1630 and 1680 cm^{-1} [72]. As previously reported that αS forms the β-sheet structure in the organic solvent [73-77], the use of chloroform in this study enabled us to obtain the αS-mediated nanoparticle films.

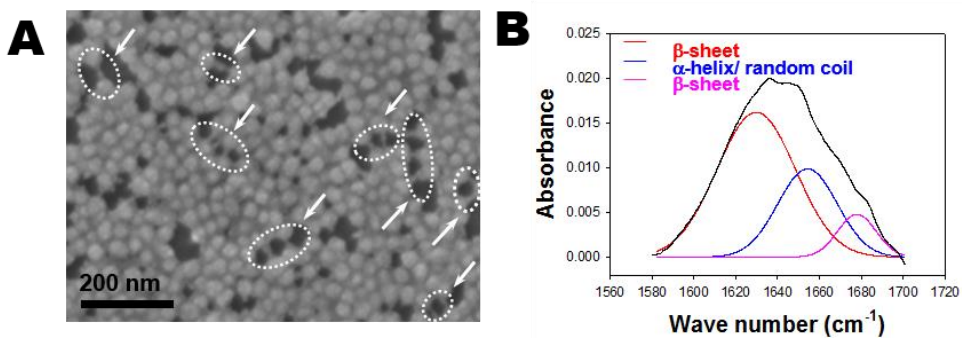

Figure 35. Interaction between αS-AuNPs in free-standing film. SEM image of a αS-AuNP film showing the extended αS interconnections between AuNPs as indicated within the dotted line circles and arrows. d) ATR-FTIR spectra (black bold curve) for the amide I band of αS-AuNP film. Deconvoluted curves in red and pink represent the β-sheet conformation. The blue curve indicates α-helix/random coil structure of αS.

(3) Optical property of αS-AuNP free-standing film

Three different size AuNPs with diameters of 10-, 20-, and 30-nm were used separately to create the free-standing films, and their properties were analyzed. All the protein-particle conjugates were able to produce the monolayer films as observed with SEM images although the packing density appeared to decrease as the AuNP size increased (Figure 36a). Atomic force microscopy (AFM) data indicated that the thickness of each film was comparable to the size of AuNPs with which the films were prepared (Figure 36b). Optical images of those films showed transparent sheets with different colors depending on the particle size: bright pink for the 10-nm-diameter NPs, purple-blue for the 20-nm NPs, and dark blue for the 30-nm NPs (Figure 36c). Surface plasmon resonance (SPR) spectra of the films were monitored by using a micro Raman microscope [63]; absorption spectra of the films made of 10-, 20-, and 30-nm-diameter AuNPs culminated at wavelengths of 530, 570, and 620 nm, respectively, reflecting their color difference (Figure 36d). In comparison with the spectra of colloidal AuNPs, those maxima were red-shifted from 518, 523, and 528 nm, respectively, owing to the plasmonic coupling between adjacent gold particles within the tightly packed films [78]. The extent of red-shift upon the film formation augmented as the particle size increased, which would be due to the enlarged area for plasmonic oscillation between adjacent particles.

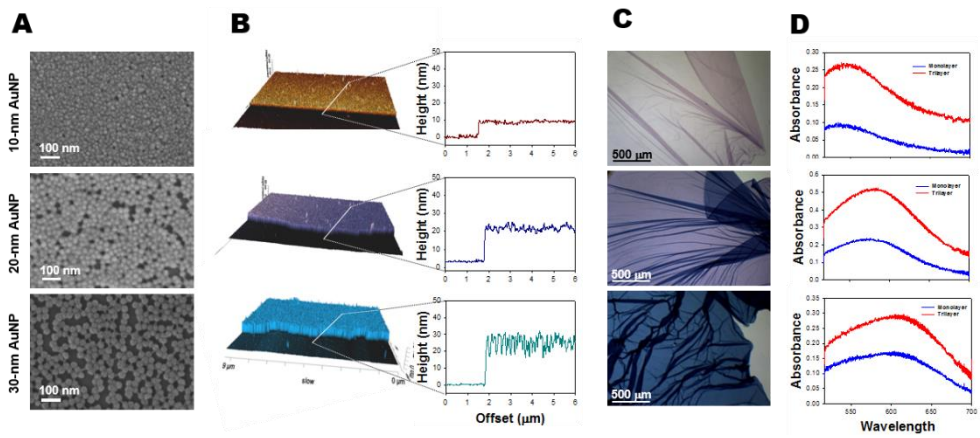

Figure 36. NP size dependency of optical properties of αS-AuNP monolayer films. Different αS-AuNP monolayer films produced with 10-nm-diameter AuNPs (top row), 20-nm-diameter AuNPs (middle row), and 30-nm-diameter AuNPs (bottom row). (a) Three-dimensional AFM images of the αS-AuNP films showing the thickness profiles. (b) Optical microscope images of the αS-AuNP films. (c) SPR spectra of the films acquired by monitoring local absorbance of the films with Reinshaw InVia Raman spectrometer. The red and blue curves indicate the adsorption spectra of the αS-AuNP films in triple layers and single layer, respectively.

(4) Flexibility of αS-AuNP free-standing film

These AuNP films were flexible in chloroform, and are expected to provide conformal contact to micron-scale three-dimensional objects like spherical silica beads with a diameter of 1 μm. The film made of 10-nm AuNPs yielded conformal wrapping around a silica bead without showing any cracks (Figure 37a). In particular, the film maintained its structural fidelity at the junction between the bead and a plane surface (Figure 37b). The film also conformally overlaid multiple spheres located adjacent to each other without causing any structural collapse (Figure 37c-e). In particular, the conformal contact formation would be a crucial feature for the development of bio-compatible devices monitoring in vivo organ/tissue activities [79-81].

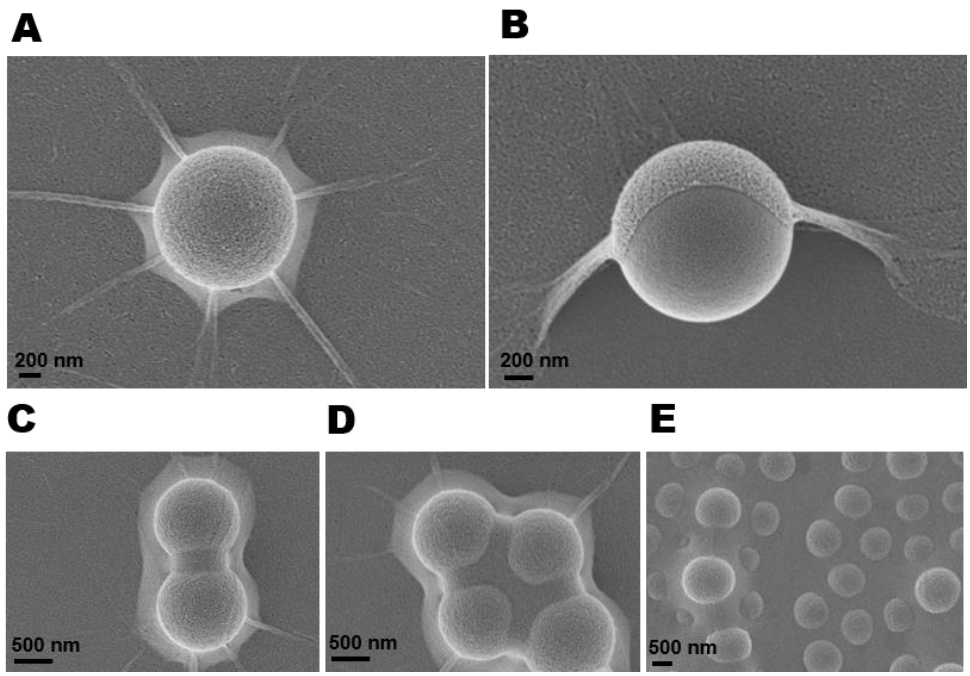

Figure 37. Conformal contact of αS-AuNP free-standing film. (a) SEM image showing conformal contact of the αS-AuNP film wrapping a 1-μm-diameter silica bead. (b) An image showing the film partly covering a silica bead. c, d, e) SEM images of the film wrapping two (c), four (d), and numerous (e) silica beads located adjacent to each other.

(5) Stability of αS-AuNP free-standing film

The stability of the transferred film is also critical for the development of bio-electronic devices. Since the film formation was mediated by the protein of αS, the film's durability was evaluated in conditions affecting the protein's stability. Although αS molecule tends to be self-interactive during a prolonged in vitro incubation, the film was demonstrated to be unaffected even after 7 days of incubation in 20 mM MES (pH 6.5) at 37℃ [82] (Figure 38a). The absorption spectra were almost identical before and after the prolonged incubation (Figure 38b). It suggests that the αS protein undergoes neither additional aggregation nor disintegration within the film structure under the aqueous condition. Moreover, thermal stability of the film was also tested at 80℃ where most proteins experience structural denaturation. Intriguingly, the film's morphology and its absorption spectra were hardly affected even after 7 days of incubation at the high temperature (Figure 38c and d). Its thermal durability is possibly attributed to the inherent heat-stable property of αS [83]. In addition, the film's solvent stability was also checked in ethanol, acetone, dimethyl sulfoxide (DMSO), and acetonitrile because they are often employed during fabrication of electronic devices or solar cell. The mean absorbance of the film in the region of 565-575 nm remained virtually unaffected before and after a 1 h immersed incubation in the solvents (Figure 38e). These experimental data suggest that the αS-AuNP film could be considered as a sustainable biocompatible material to be used in the device development.

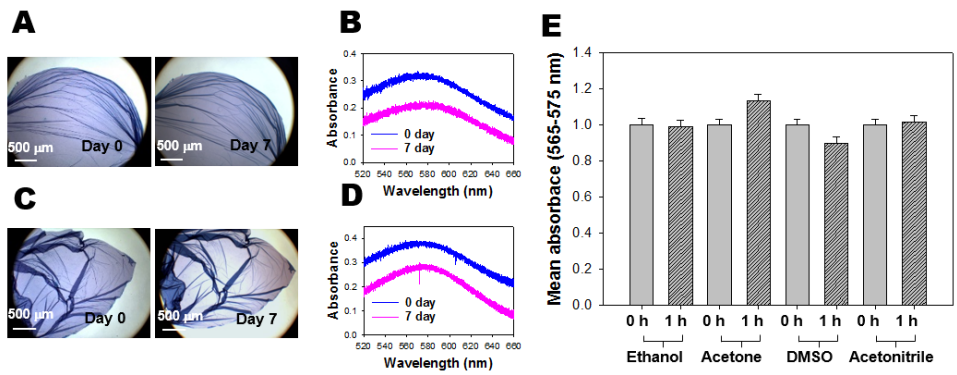

Figure 38. Stability of transferred αS-AuNP free-standing film. (a) Macroscopic optical images of the transferred films before and after incubating them in aqueous environment of 20 mM MES (pH 6.5) at 37ºC for 7 days, and (b) absorption spectra of the films on glass substrate monitored with Raman spectrometer before and after the incubation. (c) Morphologies of the films attached on glass substrate before and after its exposure to 80ºC for 7 days, and (d) their absorption spectra. (e) Absorbance of the films attached on the glass were obtained as the mean value of absorbance over the range of 645-655 nm before (gray) and after (oblique lines in gray) their exposure to ethanol, acetone, DMSO, or acetonitrile for 1 h.

(6) Patterning of αS-AuNP free-standing film

The AuNP films were patterned in 2-dimension by employing a microfluidic device prepared with poly(diemthylsiloxane) (PDMS) through soft lithography [84]. Colloidal dispersion of αS-AuNPs was injected into a channel on the patterned device tightly attached to the bottom layer of plasma-treated PC substrate [68] (Figure 39a, b). As the PC layer was detached from the top PDMS mold, the αS-AuNPs were found to be adsorbed at the bottom in monolayer with the patterned arrays of 100-μm-diameter circles separated in an equal distance of 300 μm (Figure 39c, left), 450 μm (Figure 39c, middle), and 600 μm (Figure 39c, right). These micron-scale patterns were maintained in the free-floating AuNP films following the removal of the PC substrate with chloroform (Figure 39d). Although patterning of free-standing nano-sheets has been suggested to be possible [59,63], no reports have been made to produce such two-dimensional micron-scale patterns with the ultrathin AuNP films as demonstrated in this study. Since patterning techniques are crucial for fabricating electronic devices [85], the patternable and flexible ultrathin αS-AuNP films would afford another potential to be applied in nano-bioelectronics [86,87].

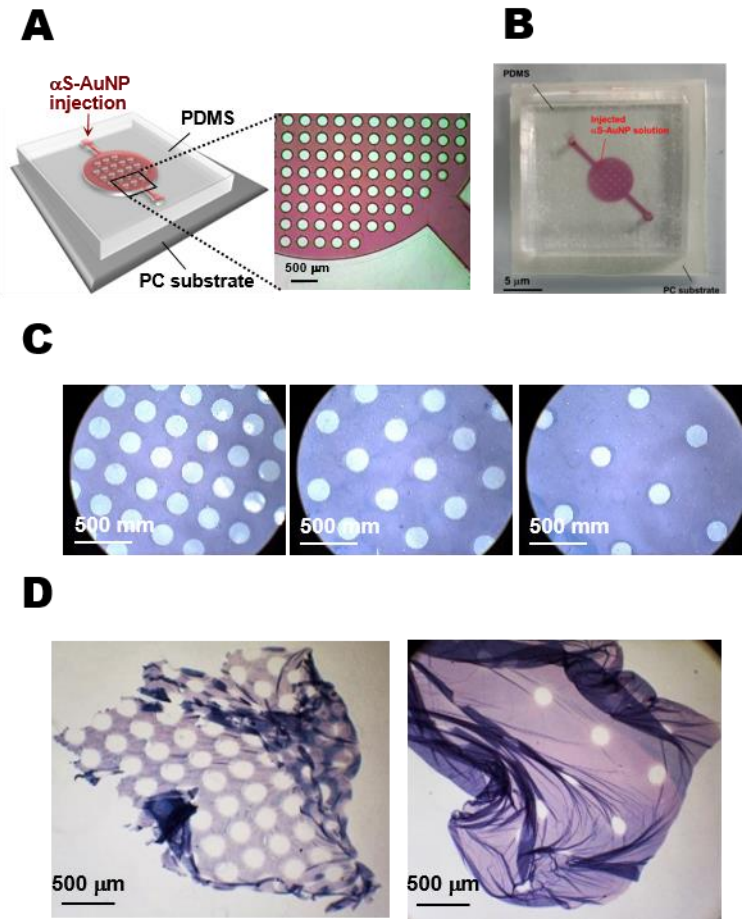

Figure 39. Patterning of αS-AuNP film. (a) A schematic image showing the PDMS microfluidic soft lithography mold and the PC substrate. (b) An optical image A microfluidic device injected with a colloidal dispersion of αS-AuNPs. (c) Optical images of the microchannels loaded with the αS-AuNPs containing 10-nm-diameter AuNP. Center-to-center distances between holes are 300 μm (left), 450 μm (middle), and 600 μm (right). (d) Images of the patterned αS-AuNP free-floating films with 100-μm-diameter holes with the center-to-center spacing of 300 μm (left) and 600 μm (right).

(7) Fabrication of double-component AuNP film

Double-component AuNP films comprising two different sizes of the particles were constructed via sequential adsorptions of 10 nm and 20 nm AuNPs (Figure 40a). The 20 nm αS-AuNPs were adsorbed on the half of a round shape PC substrate by masking the other half with a paraffin film. The mask was then removed and the conjugates with 10-nm-diameter NPs were adsorbed onto the newly exposed half-surface of the substrate (Figure 40b). After dissolving the underlying PC with chloroform, the flexible free-floating double-component AuNP film was obtained (Figure 40c). The resulting two semi-circles were different in colors, depending on the sizes of AuNPs. Each area was confirmed to be single layered by measuring the thickness with AFM (Figure 40d). This fact again indicated that the PC interaction was preferred for αS-AuNPs to the interactions between the pre-adsorbed 20 nm αS-AuNPs and the upcoming 10 nm αS-AuNPs. Using the same procedure, another free-floating double component film was fabricated with the 'SNU' logo embedded (Figure 40e). The letters were formed with the 20-nm AuNPs while the background was prepared with the 10-nm particles. This double-component film was also stable and flexible in chloroform (Figure 40f). This maneuver clearly demonstrates a feasibility of manufacturing patterned multi-component monolayer films of NPs with various functionalities using, for example, magnetic NPs or quantum dots.

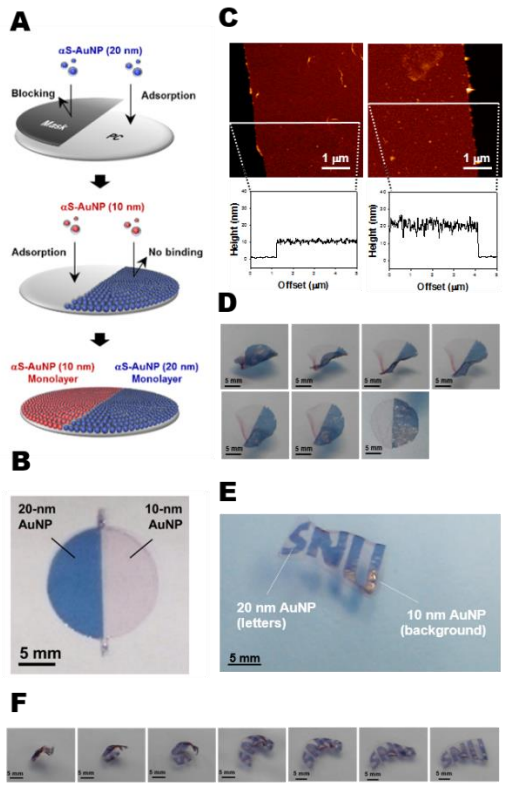

Figure 40. Fabrication of double-component films. (a) Schematic diagram showing the fabrication of double-component αS-AuNP film between 10- and 20-nm-diameter AuNPs. (b) Macroscopic image of the double-component αS-AuNP monolayer adsorbed on PC substrate. The monolayer consists of two semi-circles of the αS-AuNP monolayer comprising 20-nm-diameter AuNP (left) and 10-nm-diameter AuNP (right). (c) AFM images and height profiles of the double-component film. The areas made of 20- and 10-nm-diameter AuNPs are shown in the left and right panels, respectively. (d) A series of time lapse images of the double-component αS-AuNP film in chloroform. The flexible film was prepared with 10- and 20-nm-diameter AuNPs. e) Double-component film showing the 'SNU' logo. The letters were prepared with the 20-nm-diameter AuNPs while the background was made of 10-nm-diameter AuNPs. (f) A series of time lapse images of the double-component αS-AuNP film showing the 'SNU' logo in chloroform.

III-4. Conclusions

We have described a facile procedure of fabricating the protein-based free-standing AuNP monolayer films over wafer-scale, which can be not only patterned using soft lithographic technique but prepared in the free-floating multi-component sheets as well. This procedure is established based on three unique interactions between αS and AuNP, between αS and PC substrate, and between αS and αS. The αS encapsulating AuNPs directs adsorption of the protein-NP conjugates onto the plasma-treated PC substrate to form the AuNP monolayer. Subsequent chloroform-induced αS–αS interaction allows interconnection of the αS-coated AuNPs into the free-floating monolayer film as the PC substrate is dissolved. The resulting protein-protein interaction produces the β-sheet conformation between the αS molecules, which permits the films to exert resistance to chemical degradation and favorable mechanical property [88] as witnessed with the conformal contact formation and the thermal and solvent durability of the films. Taken all these properties together, the ultrathin free-standing AuNP monolayer film has potentials to be applied in a wide range of nanobiotechnology including development of nano-electronic devices. Furthermore, this type of single layered NP sheets could be used in ultrathin display and nano-membranes with electromechanical properties by incorporating various types of NPs such as quantum dots and magnetic nanoparticles.

References

[1] Fujiwara, K., Kasaya, H., Ogawa, N. Gold nanoparticle monolayer formation on a chemically modified glass surface. *Anal. Sci.* **25** (2009) 241-248.

[2] Lee, Y. H., Shi, W. X., Lee, H. K., Jiang, R. B., Phang, I. Y., Cui, Y., Isa, L., Yang, Y. J., Wang, J. F., Li, S. Z., Ling, X. Y. Nanoscale surface chemistry directs the tunable assembly of silver octahedra into three two-dimensional plasmonic superlattices. *Nat. Commun.* **6** (2015).

[3] Son, D., Lee, J., Qiao, S., Ghaffari, R., Kim, J., Lee, J. E., Song, C., Kim, S. J., Lee, D. J., Jun, S. W., Yang, S., Park, M., Shin, J., Do, K., Lee, M., Kang, K., Hwang, C. S., Lu, N. S., Hyeon, T., Kim, D. H. Multifunctional wearable devices for diagnosis and therapy of movement disorders. *Nat. Nanotechnol.* **9** (2014) 397-404.

[4] Liu, Y., Cheng, R., Liao, L., Zhou, H. L., Bai, J. W., Liu, G., Liu, L. X., Huang, Y., Duan, X. F. Plasmon resonance enhanced multicolour photodetection by graphene. *Nat. Commun.* **2** (2011).

[5] Ryu, D. Y., Shin, K., Drockenmuller, E., Hawker, C. J., Russell, T. P. A generalized approach to the modification of solid surfaces. *Science* **308** (2005) 236-239.

[6] Lee, H., Dellatore, S. M., Miller, W. M., Messersmith, P. B. Mussel-inspired surface chemistry for multifunctional coatings. *Science* **318** (2007) 426-430.

[7] Ku, S. H., Lee, J. S., Park, C. B. Spatial control of cell adhesion and patterning through mussel-inspired surface modification by polydopamine. *Langmuir* **26** (2010) 15104-15108.

[8] Ryou, M. H., Kim, J., Lee, I., Kim, S., Jeong, Y. K., Hong, S., Ryu, J. H., Kim, T. S., Park, J. K., Lee, H., Choi, J. W. Mussel-inspired adhesive binders for high-performance silicon nanoparticle anodes in lithium-ion batteries. *Adv. Mater.* **25** (2013) 1571-1576.

[9] You, I., Lee, T. G., Nam, Y. S., Lee, H. Fabrication of a micro-omnifluidic device by omniphilic/omniphobic patterning on nanostructured surfaces. *ACS Nano* **8** (2014) 9016-9024.

[10] Zhu, Q., Pan, Q. M. Mussel-inspired direct immobilization of nanoparticles and application for oil-water separation. *ACS Nano* **8** (2014) 1402-1409.

[11] Ferreon, A. C. M., Gambin, Y., Lemke, E. A., Deniz, A. A. Interplay of α-synuclein binding and conformational switching probed by single-molecule fluorescence. *Proc. Natl. Acad. Sci. U.S.A.* **106** (2008) 5645-5650.

[12] Ullman, O., Fisher, C. K., Stultz, C. M. Explaining the structural plasticity of alpha-synuclein. *J. Am. Chem. Soc.* **133** (2011) 19536-19546.

[13] Dyson, H. J., Wright, P. E. Intrinsically unstructured proteins and their functions. *Nat. Rev. Mol. Cell Bio.* **6** (2005) 197-208.

[14] Shin, H.-J., Lee, E.-K., Lee, J.-H., Lee, D., Chang, C.-S., Kim, Y.-S., Paik, S. R. Eosin interaction of α-synuclein leading to protein self-oligomerization. *BBA-Protein Struct M.* **1481** (2000) 139-146.

[15] Lee, D., Lee, E.-K., Lee, J.-H., Chang, C.-S., Paik, S. R. Self-oligomerization and protein aggregation of α-synuclein in the presence of coomassie brilliant blue. *FEBS J.* **268** (2001) 295-301.

[16] Lee, C.-H., Kim, H. J., Lee, J.-H., Cho, H.-J., Kim, J., Chung, K. C., Jung, S., Paik, S. R. Dequalinium-induced protofibril formation of α-synuclein. *J. Biol. Chem.* **281** (2006) 3463-3472.

[17] Lee, E.-N., Cho, H.-J., Lee, C.-H., Lee, D., Chung, K. C., Paik, S. R. Phthalocyanine tetrasulfonates affect the amyloid formation and cytotoxicity of α-synuclein. *Biochemistry* **43** (2004) 3704-3715.

[18] Giasson, B. I., Forman, M. S., Higuchi, M., Golbe, L. I., Graves, C. L., Kotzbauer, P. T., Trojanowski, J. Q., Lee, V. M.-Y. Initiation and synergistic fibrillization of tau and α-synuclein. *Science* **300** (2003) 636-640.

[19] Choi, B.-K., Kim, J.-Y., Cha, M.-Y., M.-J., I., Shin, Y.-K., Lee, N. K. B-amyloid and α-synuclein cooperate to block snare-dependent vesicle fusion. *Biochemistry* **54** (2015) 1831-1840.

[20] Burré, J., Sharma, M., Tsetsenis, T., Buchman, V., Etherton, M. R., Südhof, T. C. α-synuclein promotes snare-complex assembly in vivo and in vitro. *Science* **329** (2010) 1663-1667.

[21] Kim, J., Moon, C. H., Jung, S., Paik, S. R. α-synuclein enhances bioluminescent activity of firefly luciferase by facilitating luciferin localization. *BBA-Proteins Proteomics* **1794** (2009) 309-314.

[22] Paik, S. R., Lee, D., Cho, H.-J., Lee, E.-N., Chang, C.-S. Oxidized glutathione stimulated the amyloid formation of α-synuclein. *FEBS Lett.* **537** (2003) 63-67.

[23] Bhak, G., Lee, J., Kim, C.-H., Chung, D. Y., Kang, J. H., Oh, S., Lee, J., Kang, J. S., Yoo, J. M., Yang, J. E., Rhoo, K. Y., Park, S., Lee, S., Nam, K. T., Jeon, N. L., Jang, J., Hong, B. H., Yoon, M.-H., Paik, S. R. Title high density single-layer coating of gold nanoparticles onto multiple substrates by using omni-adhesive protein of α-synuclein for nano applications. *ACS Appl. Mater. Inter. in press* (2017).

[24] Yang, J. A., Johnson, B. J., Wu, S., Woods, W. S., George, J. M., Murphy, C. J. Study of wild-type alpha-synuclein binding and orientation on gold nanoparticles. *Langmuir* **29** (2013) 4603-4615.

[25] Lin, W., Insley, T., Tuttle, M. D., Zhu, L. Y., Berthold, D. A., Kral, P., Rienstra, C. M., Murphy, C. J. Control of protein orientation on gold nanoparticles. *J. Phys. Chem. C* **119** (2015) 21035-21043.

[26] Lee, D., Choe, Y.-J., Choi, Y. S., Bhak, G., Lee, J., Paik, S. R. Photoconductivity of pea-pod-type chains of gold nanoparicles encapsulated within dielectric amyloid protein nanofibrils of α-synuclein. *Angew. Chem. Int. Ed.* **50** (2011) 1332-1337.

[27] Lee, D., Choe, Y.-J., Lee, M., Jeong, D. H., Paik, S. R. Protein-based sers technology monitoring the chemical reactivity on an a-synuclein-mediated two-dimensional array of gold nanoparticles. *Langmuir* **27** (2011) 12782-12787.

[28] Paik, S. R., Lee, J. H., Kim, D. H., Chang, C. S., Kim, J. Aluminum-induced structural alterations of the precursor of the non-a beta component of alzheimer's disease amyloid. *Arch. Biochem. and Biophysics* **344** (1997) 325-334.

[29] Xia, Y. N., Whitesides, G. M. Soft lithography. *Angew. Chem. Int. Edit.* **37** (1998) 550-575.

[30] Lee, J., Bhak, G., Lee, J. H., Park, W., Lee, M., Lee, D., Jeon, N. L., Jeong, D. H., Char, K., Paik, S. R. Free-standing gold-nanoparticle monolayer film fabricated by protein self-assembly of alpha-synuclein. *Angew. Chem. Int. Ed.* **54** (2015) 4571-4576.

[31] Shipway, A. N., Katz, E., Willner, I. Nanoparticle arrays on surfaces for electronic, optical, and sensor applications. *ChemPhysChem* **1** (2000) 18-52.

[32] Kim, C. H., Bhak, G., Lee, J., Sung, S., Park, S., Paik, S. R., Yoon, M. H. Controlled charge trapping and retention in large-area monodisperse protein metal-nanoparticle conjugates. *ACS Appl. Mater. Inter.* **8** (2016) 11898-11903.

[33] Georgakilas, V., Gournis, D., Tzitzios, V., Pasquato, L., Guldi, D. M., Prato, M. Decorating carbon nanotubes with metal or semiconductor nanoparticles. *J. Mater. Chem.* **17** (2007) 2679-2694.

[34] Kim, S.-S., Kim, Y.-R., Chung, T. D., Sohn, B.-H. Tunable decoration of reduced graphene oxide with au nanoparticles for the oxygen reduction reaction. *Adv. Funct. Mater.* **24** (2014) 2764-2771.

[35] Standridge, S. D., Schatz, G. C., Hupp, J. T. Distance dependence of plasmon-enhanced photocurrent in dye-sensitized solar cells. *J. Am. Chem. Soc.* **131** (2009) 8407-8409.

[36] Atwater, H. A., Polman, A. Plasmonics for improved photovoltaic devices. *Nat. Mater.* **9** (2010) 205-213.

[37] Belton, D., Paine, G., Patwardhan, S. V., Perry, C. C. Towards an understanding of (bio)silicification: The role of amino acids and lysine oligomers in silicification. *J. Mater. Chem.* **14** (2004) 2231-2241.

[38] Bastus, N. G., Comenge, J., Puntes, V. Kinetically controlled seeded growth synthesis of citrate-stabilized gold nanoparticles of up to 200 nm: Size focusing versus ostwald ripening. *Langmuir* **27** (2011) 11098-11105.

[39] Hummers, W. S., Offeman, R. E. Preparation of graphitic oxide. *J. Am. Chem. Soc.* **80** (1958) 1339-1339.

[40] Kim, C. H., Bonnassieux, Y., Horowitz, G. Compact dc modeling of organic field-effect transistors: Review and perspectives. *IEEE T. Electron. Dev.* **61** (2014) 278-287.

[41] Kim, C. H., Yaghmazadeh, O., Tondelier, D., Bin Jeong, Y., Bonnassieux, Y., Horowitz, G. Capacitive behavior of pentacene-based diodes: Quasistatic dielectric constant and dielectric strength. *J. Appl. Phys.* **109** (2011).

[42] Steudel, S., De Vusser, S., De Jonge, S., Janssen, D., Verlaak, S., Genoe, J., Heremans, P. Influence of the dielectric roughness on the performance of pentacene transistors. *Appl. Phys. Lett.* **85** (2004) 4400-4402.

[43] Cherevko, S., Zeradjanin, A. R., Keeley, G. P., Mayrhofer, K. J. J. A comparative study on gold and platinum dissolution in acidic and alkaline media. *J. Electrochem. Soc.* **161** (2014) H822-H830.

[44] Tang, W., Lin, H. F., Kleiman-Shwarsctein, A., Stucky, G. D., McFarland, E. W. Size-dependent activity of gold nanoparticles for oxygen electroreduction in alkaline electrolyte. *J. Phys. Chem. C* **112** (2008) 10515-10519.

[45] Meyers, S. R., Hamilton, P. T., Walsh, E. B., Kenan, D. J., Grinstaff, M. W. Endothelialization of titanium surfaces. *Adv. Mater.* **19** (2007) 2492-2498.

[46] Tong, L., Zhao, Y., Huff, T. B., Hansen, M. N., Wei, A., Cheng, J.-X. Gold nanorods mediate tumor cell death by compromising membrane integrity. *Adv. Mater.* **19** (2007) 3136-3141.

[47] El-Sayed, I. H., Huang, X., El-Sayed, M. A. Surface plasmon resonance scattering and absorption of anti-egfr antibody conjugated gold nanoparticles in cancer diagnostics: Applications in oral cancer. *Nano Lett.* **5** (2005) 829-834.

[48] Huschka, R., Neumann, O., Barhoumi, A., Halas, N. J. Visualizing light-triggered release of molecules inside living cells. *Nano Lett.* **10** (2010) 4117-4122.

[49] Huh, D., Hamilton, G. A., Ingber, D. E. From 3d cell culture to organs-on-chips. *Trends Cell Biol.* **21** (2011) 745-754.

[50] Polini, A., Prodanov, L., Bhise, N. S., Manoharan, V., Dokmeci, M. R., Khademhosseini, A. Organ-on-a-chip: A new tool for drug discovery. *Expert Opin. Drug Discov.* **9** (2014) 335-352.

[51] Annabi, N., Selimovic, Š., Cox, J. P. A., Ribas, J., Bakooshli, M. A., Heintze, D., Weiss, A. S., Cropek, D., Khademhosseini, A. Hydrogel-coated microfluidic channels for cardiomyocyte culture. *Lab Chip* **13** (2013) 3569-3577.

[52] Kang, S., Lee, J., Ryu, S., Kwon, Y., Kim, K.-H., Jeong, D. H., Paik, S. R., Kim, B.-S. Gold nanoparticle/graphene oxide hybrid sheets attached on mesenchymal stem cell surface for photothermal cancer therapy. *Chem. Mater. in press* (2017).

[53] Talukdar, Y., Rashkow, J. T., Lalwani, G., Kanakia, S., Sitharaman, B. The effects of graphene nanostructures on mesenchymal stem cells. *Biomaterials* **35** (2014) 4863-4877.

[54] Park, J., Kim, B., Han, J., Oh, J., Park, S., Ryu, S., Jung, S., Shin, J. Y., Lee, B. S., Hong, B. H., Choi, D., Kim, B. S. Graphene oxide flakes as a cellular adhesive: Prevention of reactive oxygen species mediated death of implanted cells for cardiac repair. *ACS Nano* **9** (2015) 4987-4999.

[55] Hynes, R. O., Sauer, R. T., Sharp, P. A. The whitehead-institute and mit. *Science* **256** (1992) 719-719.

[56] Kim, C., Cho, E. D., Kim, H. K., You, S., Lee, H. J., Hwang, D., Lee, S. J. Beta 1-integrin-dependent migration of microglia in response to neuron-released alpha-synuclein. *Exp. Mol. Med.* **46** (2014).

[57] Jaque, D., Maestro, L. M., del Rosal, B., Haro-Gonzalez, P., Benayas, A., Plaza, J. L., Rodriguez, E. M., Sole, J. G. Nanoparticles for photothermal therapies. *Nanoscale* **6** (2014) 9494-9530.

[58] Geim, A. K., Novoselov, K. S. The rise of graphene. *Nat. Mater.* **6** (2007) 183-191.

[59] Jin, J., Wakayama, Y., Peng, X., Ichinose, I. Surfactant-assisted fabrication of free-standing inorganic sheets covering an array of micrometre-sized holes. *Nat. Mater.* **6** (2007) 686-691.

[60] Vendamme, R., Onoue, S. Y., Nakao, A., Kunitake, T. Robust free-standing nanomembranes of organic/inorganic interpenetrating networks. *Nat. Mater.* **5** (2006) 494-501.

[61] Anselmetti, D., Golzhauser, A. Converting molecular monolayers into functional membranes. *Angew. Chem. Int. Edit.* **53** (2014) 12300-12302.

[62] Celebi, K., Buchheim, J., Wyss, R. M., Droudian, A., Gasser, P., Shorubalko, I., Kye, J. I., Lee, C., Park, H. G. Ultimate permeation across atomically thin porous graphene. *Science* **344** (2014) 289-292.

[63] Cheng, W., Campolongo, M. J., Cha, J. J., Tan, S. J., Umbach, C. C., Muller, D. A., Luo, D. Free-standing nanoparticle superlattice sheets controlled by DNA. *Nat. Mater.* **8** (2009) 519-525.

[64] Jiang, C., Markutsya, S., Pikus, Y., Tsukruk, V. V. Freely suspended nanocomposite membranes as highly sensitive sensors. *Nat. Mater.* **3** (2004) 721-728.

[65] Lin, Y., Kaff, H., Emrick, T., Dinsmore, A. D., Russel, T. P. Nanoparticle assembly and transport at liquid-liquid interfaces. *Science* **299** (2003) 226-229.

[66] Lin, Y., Skaff, H., Böker, A., Dinsmore, A. D., Emrick, T., Russell, T. P. Ultrathin cross-linked nanoparticle membranes. *J. Am. Chem. Soc.* **125** (2003) 12690-12691.

[67] Mueggenburg, K. E., Lin, X.-M., Goldsmith, R. H., Jaeger, H. M. Elastic membranes of close-packed nanoparticle arrays. *Nat. Mater.* **6** (2007) 656-660.

[68] Tang, L., Lee, N. Y. A facile route for irreversible bonding of plastic-pdms hybrid microdevices at room temperature. *Lab chip* **10** (2010) 1274-1280.

[69] Kang, S., Yang, J. E., Kim, J., Ahn, M., Koo, H. J., Kim, M., Lee, Y. S., Paik, S. R. Removal of intact beta 2-microglobulin at neutral ph by using seed-conjugated polymer beads prepared with beta 2-microglobulin-derived peptide (58-67). *Biotechnol. Progr.* **27** (2011) 521-529.

[70] Yang, J. A., Lin, W., Woods, W. S., George, J. M., Murphy, C. J. α-synuclein's adsorption, conformation, and orientation on cationic gold nanoparticle surfaces seeds global conformation change. *J. Phys. Chem. B* **118** (2014) 3559-3571.

[71] Tycko, R. Molecular structure of amyloid fibrils: Insights from solid-state nmr. *Q. Rev. Biophys.* **39** (2006) 1-55.

[72] Berthelot, K., Immel, F., Géan, J., Lecomte, S., Oda, R., Kauffmann, B., Cullin, C. Driving amyloid toxicity in a yeast model by structural change: A molecular approach. *Faseb J.* **23** (2009) 1-10.

[73] Chaudhary, N., Singh, S., Nagaraj, R. Organic solvent mediated self-association of an amyloid forming peptide from β_2-microglobulin: An atomic force microscopy study. *Peptide Science* **90** (2008) 783-791.

[74] Munishkina, L. A., Phelan, C., Uversky, V. N., Fink, A. L. Conformational behavior and aggregation of α-synuclein in organic solvents: Modeling the effects of membranes. *Biochemistry* **42** (2003) 2720-2730.

[75] Krysmann, M. J., Castelletto, V., Mckendrick, J. E., Clifton, L. A., Hamley, I. W. Self-assembly of peptide nanotubes in an organic solvent. *Langmuir* **24** (2008) 8158-8162.

[76] Krysmann, M. J., Catelletto, V., Hamley, I. W. Fibrillisation of hydrophobically modified amyloid peptide fragments in an organic solvent. *Soft Matter* **3** (2007) 1401-1406.

[77] Lee, J.-H., Bhak, G., Lee, S.-G., Paik, S. R. Instantaneous amyloid fibril formation of α-synuclein from the oligomeric granular structures in the presence of hexane. *Biophys. J.* **95** (2008) L16-L18.

[78] Ghosh, S. K., Pal, T. Interparticle coupling effect on the surface plasmon resonance of gold nanoparticles: From theory to applications. *Chem. Rev.* **107** (2007) 4979-4862.

[79] Viventi, J., Kim, D.-H., Moss, J. D., Kim, Y.-S., Blanco, J. A., Annetta, N., Hicks, A., Xiao, J., Huang, Y., Callans, D. J., Rogers, J. A., Litt, B. A conformal, bio-interfaced class of silicon electronics for mapping cardiac electrophysiology. *Sci. Transl. Med.* **2** (2010) 1-9.

[80] Webb, R. C., Bonifas, A. P., Behnaz, A., Zhang, Y., Yu, K. J., Cheng, H., Shi, M., Bian, Z., Liu, Z., Kim, Y.-S., Yeo, W.-H., J.-S, P., Song, J., Li, Y., Huang, Y., Gorbach, A. M., Rogers, J. A. Ultrathin

conformal devices for precise and continuous thermal characterization of human skin. *Nat. Mater.* **12** (2013) 938-944.

[81] Kim, D. H., Viventi, J., Amsden, J. J., Xiao, J., Vigeland, L., Kim, Y. S., Blanco, J. A., Panilaitis, B., Frechette, E. S., Contreras, D., Kaplan, D. L., Omenetto, F. G., Huang, Y., Hwang, K. C., Zakin, M. R., Litt, B., Rogers, J. A. Dissolvable films of silk fibroin for ultrathin conformal bio-integrated electronics. *Nat. Mater.* **9** (2010) 511-517.

[82] Murray, I. V. J., Giasson, B. I., Quinn, S. M., Koppaka, V., Axelsen, P. H., Ischiropoulos, H., Trojanowski, J. Q., Lee, V. M.-Y. Role of α-synuclein carboxy-terminus on fibril formation in vitro. *Biochemistry* **42** (2003) 8530-8540.

[83] Kim, T. D., Ryu, H. J., Cho, H. I., Yang, C.-H., Kim, J. Thermal behavior of proteins: Heat-resistant proteins and their heat-induced secondary structural changes. *Biochemistry* **39** (2000) 14839-14846.

[84] Taylor, A. M., Blurton-Jones, M., Rhee, S. W., Cribbs, D. H., Cotman, C. W., Jeon, N. L. A microfluidic culture platform for cns axonal injury, regeneration and transport. *Nat. Methods* **2** (2005) 599-605.

[85] Yoo, J. E., Lee, K. S., Garcia, A., Tarver, J., Gomez, E. D., Baldwin, K., Sun, Y., Meng, H., Nguyen, T. Q., Loo, Y. L. Directly patternable, highly conducting polymers for broad applications in organic electronics. *Proc. Natl. Acad. Sci. U.S.A.* **107** (2010) 5712-5717.

[86] Irimia-Vladu, M., Sariciftci, N. S., Bauer, S. Exotic materials for bio-organic electronics. *J. Mater. Chem.* **21** (2011) 1350.

[87] Rousche, P. J., Pellinen, D. S., D. P. Privin, J., Williams, J. C., Vetter, R. J., Kipke, D. R. Flexible polyimide-based intracortical electrode arrays with bioactive capability. *IEEE Trans. Biomed. Eng.* **48** (2001) 361-371.

[88] Knowles, T. P., Fitzpatrick, A. W., Meehan, S., Mott, H. R., Vendruscolo, M., Dobson, C. M., Welland, M. E. Role of intermolecular forces in defining material properties of protein nanofibrils. *Science* **318** (2007) 1900-1903.

국문초록

나노입자는 기존의 재료가 가지지 못했던 독특한 화학적, 광학적, 전기적 성질은 가진다. 이러한 재료들을 실제 소자에 응용하기 위하여서 특정 구조로 나노입자를 조립하는 것이 필수적이다. 다양한 구조들 중 2차원 구조체의 경우, 다양한 전기나 광학 소자에 응용이 가능하다. 이런 이유에서 DNA나 고분자를 이용하여 나노입자를 이차원으로 조립하려는 시도가 있어왔다.

알파-시뉴클레인 (α-Synuclein, αS)는 아밀로이드성 단백질로 자가-조립을 통하여 아밀로이드 섬유를 만드는 것으로 알려져 있다. 이 단백질은 여러가지 분자와 상호작용하는 intrinsically disordered protein (IDP)의 한 종류이다. 흥미롭게도, 우리는 αS가 금나노입자를 코팅할 수 있다는 사실을 알아내었다. αS는 140개의 아미노산으로 이루어져 있으며 염기성 아미노산이 많은 N-말단, 소수성 아미노산이 많은 non-amyloid-β 영역 (NAC), 산성 아미노산이 많은 C-말단, 이렇게 크게 세 부분으로 나누어 볼 수 있다. N-말단은 이 부분이 가지는 양전하로 인하여 음전하를 가지는 금나노입자와 우선적으로 상호작용한다고 생각되고 있다. C-말단과 NAC가 바깥쪽으로 노출되어 있을 것으로 생각된다.

본 연구에서는 특정 산성 pH에서 접착력을 가지는 αS-금나노입자 복합체 (αS-AuNP)에 관한 연구가 진행되었다. αS-AuNP는 pH 4.5에서 다양한 종류의 표면에 대해 뛰어난 접착력을 보였다.

놀랍게도, αS-AuNP는 산화물, 유리, 반도체, 금속, 고분자, 탄소 동소체 등 우리가 시험해본 모든 물질에 잘 흡착되었다. 이 흡착의 가장 중요한 특징은 금나노입자의 단일층이 형성된다는 것이다. 이러한 단일층 형성은 αS-AuNP의 표면과의 상호작용과 αS-AuNP간의 반발로 설명할 수 있었다. αS-AuNP의 표면과의 상호작용은 αS의 높은 구조적 자유도에 의하여 가능하였다. 반면, αS-AuNP간의 반발은 노출되어 있는 C-말단 간의 음전하간 반발로 일어났으며, 이는 단일층 형성을 유도하게 된다.

이러한 αS-AuNP의 만능 접착력은 다양한 시스템에 적용될 수 있었다. 전자빔을 이용하여 100-nm 수준의 형태로 패터닝이 가능하였다. 또한, 용액 상 반응을 기반으로 한다는 장점으로 인하여 다양한 3차원 구조에 흡착될 수 있었다. 우리는 이러한 αS-AuNP의 성질을 메모리 개발, 연료전지 개발, 태양전지 개발, 세포 배양 시스템, 광열(光熱) 암 치료법 개발에 응용하였다. 이 응용 사례들에 있어, αS는 단순히 흡착을 유도할 뿐 아니라, 전하의 저장을 위한 유전층의 역할, AuNP의 표면을 노출시키기 위해 제거되는 역할, 규화 반응을 유도하는 화학적 역할, 세포의 표면과 접촉을 유도하는 생물학적 역할을 수행하였다. 본 연구에서 자유-부유성 나노입자 박막 역시 제조되었다. 자유-부유성 고밀도 나노입자 박막을 마이크로미터 크기 이상으로 제조하는 것에는 많은 어려움이 있었다. 우리는 αS-AuNP 단일층이 흡착된 고분자 층을 유기용매에 녹여 자유-부유성 나노입자 박막을 제조하였다. 이 과정에서 유기용매에 의하여 유도된 αS간의 β-sheet 구조는 전체 구조를 안정화 시키는 역할을 하였다.

주요어

알파-시뉴클레인, 금나노입자, 나노소자, 만능접착능력, 단일층